

**SILICON/GRAPHITE/GRAPHENE HYBRID ANODES VIA AIR
CONTROLLED ELECTROSPRAYING FOR LITHIUM ION BATTERIES**

A Thesis

Presented to the Faculty of the Graduate School
of Cornell University

In Partial Fulfillment of the Requirements for the Degree of
Master of Science

by

Yash Milind Joshi

December, 2019

© 2019

Yash Milind Joshi

ABSTRACT

Lithium ion batteries (LIB) have been the front runners to offer solutions to energy storage and electronic applications. The current state of art LIB's are unable to satisfy the demands for EV applications due to their low energy density. To improve the energy density of LIB's Silicon has been most promising due its extraordinary theoretical capacity However Silicon anode expands 2-3 times its original size while taking in Lithium ions for their storage. This leads to pulverization and loss of electrical contact of the electrode material leading to severe capacity decay. Thus mitigation of this volume expansion has been a stumbling block for its commercialization. In this work various strategies like an effective assembly of Silicon/ Graphite/ Graphene via Air controlled-Electrospray are utilized to overcome this issue. Moreover, using facile and scalable ways to create mesopores as well as macropores to accommodate the silicon volume expansion is also investigated. The results demonstrates capacity several times higher than the traditional LIB's as well as stable capacity over several cycles of deep discharge. The results show that the different modes of failure for silicon based anodes are successfully addressed and the proposed assembly by the means of air-controlled electrospray is scalable and economic fabrication technique.

BIOGRAPHICAL SKETCH

Yash Joshi was born in India, on 15th November, 1995. He developed an active interest in Science and Mathematics since early school days. Growing up in the state of Gujarat which is the hub of chemical industries in India he decided to pursue Chemical Engineering for his career. He gained admission to Nirma University, Institute of Technology as an undergraduate in Chemical Engineering for 4 years where he developed a keen passion for research which led to the decision to pursue Masters of Science at Cornell University. At Cornell University, he joined Prof Yong Joo's group due to his interest in the field of energy. He carried out independent research in the fast emerging field of next generation Lithium ion batteries under the guidance of Prof. Joo.

To my parents and friends.

ACKNOWLEDGMENTS

I would like to thank Prof. Joo for giving me an opportunity to work on this exciting project and providing me useful insights and suggestions throughout the course of MS research. His enthusiasm during each of my weekly meetings motivated me to pursue this project to the best of my ability. I learnt a lot from his unique method of using simple analogies to explain complex research problems. I would also like to thank Prof. Hanrath for the valuable interactions I had with him and for always being very approachable and helping.

I would like to thank SangMok for sharing his immense practical knowledge and instilling in me a sense of awareness towards industrial applications of the research that I conducted throughout my MS.

I would like to thank my parents and my brother for the ever-lasting love and support that they provided throughout my graduate studies which enabled me to carry out my MS in a successful manner.

Last but not the least I would like to thank all the past and present Joo group members who were very welcoming and with whom I had a lot of interesting discussions about and beyond research which made coming to work a lot fun.

TABLE OF CONTENTS

BIOGRAPHICAL SKETCH	iii
ACKNOWLEDGMENTS	v
LIST OF FIGURES	vii
LIST OF TABLES	viii
CHAPTER 1: INTRODUCTION	1
1.1 Introduction	1
1.2 Air-Controlled Electrospray	5
REFERENCES	8
CHAPTER 2: DIRECT DEPOSIT POROUS HYBRID SILICON ANODES FOR SCALABLE AND HIGH PERFORMANCE LITHIUM ION BATTERIES	
2.1 Introduction.....	11
2.2 Experimental section.....	14
2.3 Results and discussion	18
2.4 Conclusion	35
REFERENCES.....	36
CHAPTER 3: DIRECT DEPOSIT SILICON/GRAPHITE/GRAPHENE HYBRID ANODES FOR SCALABLE AND HIGH PERFORMANCE LITHIUM ION BATTERIES	
3.1 Introduction.....	39
3.2 Experimental Section	42
3.3 Results and Discussion	45
3.4 Conclusion	58
REFERENCES.....	59

**CHAPTER 4: PARTICLE COMPOSITES SILICON/GRAPHITE/GRAPHENE
HYBRID ANODES FOR SCALABLE AND HIGH PERFORMANCE LITHIUM
ION BATTERIES**

4.1 Introduction	62
4.2. Experimental Section	68
4.3 Results and Discussion	72
4.4 Conclusion	98
REFERENCES	100

CHAPTER 5: FUTURE WORK

5.1 Chapter 2	103
5.2 Chapter 3	105
5.3 Chapter 4	106

LIST OF FIGURES

CHAPTER 2

Fig 2.1 Schematic illustrating the fabrication process.....	13
Figure 2.2 SEM image of (a) particle before heat treatment (b) particle after heat treatment.....	19
Figure 2.3 Cross section SEM image of (a) electrode after PAA removal (b) reference electrode where no PAA is removed.....	19
Figure 2.4 Cross- section SEM image of (a) electrode with GNR (b) Magnified image of GNR (c) reference electrode without GNR	20
Figure 2.5 TGA analysis of before and after heat treatment.....	21
Figure 2.6 TGA analysis for PAA_REM and reference for case 1.....	21
Figure 2.7 TGA analysis for GNR and reference for case 2	22
Figure 2.8 BET analysis of PAA_REM and reference for Case 1.....	23
Figure 2.9 Porometry analysis of PAA_REM and reference for Case 1.....	24
Figure 2.10 BET analysis of GNR and the reference for Case 2	24
Figure 2.11 initial capacity voltage profiles of PAA_REM and Ref1	27
Figure 2.12 Cyclic voltammograms of PAA_REM and Ref1 at 1mV/s.....	27
Figure 2.13 initial capacity voltage profiles of GNR and reference for case 2	28
Figure 2.14 Cyclic voltammograms of GNR and reference for case 2.....	28
Figure 2.15 Nyquist plots of impedance data for case 1 a) before formation b) after formation c) after cycling	29
Figure 2.16 Nyquist plot of impedance data for case 2 before formation	30
Figure 2.17 Cyclic performance of PAA_REM and reference for case 1.....	31

Figure 2.18 Cyclic performance GNR and reference for case 2.....	32
Figure 2.19 Rate capability of PAA_REM and reference for Case 1.....	34
Figure 2.20 Rate capability of GNR and reference for case 2	34

CHAPTER 3

Figure 3.1 SEM images of a) CP11 and b) SF6	47
Figure 3.2 SEM images of a) low magnification top view Si/CP11 electrode b) high magnification top view of Si/CP11 electrode c) cross-section Si/CP11 electrode.....	48
Figure 3.3 SEM images of a) low magnification top view Si/SF6 electrode b) high magnification top view of Si/SF6 electrode c) cross-section Si/SF6 electrode.....	49
Figure 3.4 SEM images of a) low magnification top view Si/CP11/SF6 electrode b) high magnification top view of Si/CP11/SF6 electrode c) cross-section Si/CP11/SF6 electrode	50
Figure 3.5 TGA analysis of Si/CP11, Si/SF6, and Si/CP11/SF6.....	51
Figure 3.6 Tap density of CP11 and SF6 powder	52
Figure 3.7 initial capacity-voltage profiles of Si/SF6, Si/CP11 and Si/CP11/SF6...	55
Figure 3.8 schematic illustrating higher capacity for Si/SF6 electrode	55
Figure 3.9 Nyquist plots for impedance data for Si/CP11, Si/SF6 and Si/CP11/SF6...	57
Figure 3.10 Rate capability of Si/CP11, Si/SF6, Si/CP11/SF6	57

CHAPTER 4

Figure 4.1 Effect of lowering silicon content on cycle performance.....	66
Figure 4.2 Schematic illustrating the problem of silicon thickness change	66
Figure 4.3 Schematic illustrating the first step of the particle additive composite...	67
Figure 4.4 A visual representation of the synthesis of the particles.....	67
Figure 4.5 Schematic illustrating the second step of the particle additive composite...	68
Figure 4.6 SEM images of a) particles on the collector b) Particle after scratching....	73
Figure 4.7 SEM images of a) particle additive composite electrode b) direct deposit electrode	73
Figure 4.8 TGA analysis of particle additive and direct deposit.....	74
Figure 4.9 SEM images of particle morphology at a) 0.01 ml/min b) 0.02ml/min c) 0.03ml/min and d) 0.04 ml/min infusion rate	78
Figure 4.10 Particle size distribution vs. infusion rate.....	79
Figure 4.11 SEM images of particle morphology at a) 100% NMP b) 100% DMF c) NMP/DMF/DMA and d) NMP/DMF/THF.....	80
Figure 4.12 Particle size distribution vs. relative volatility.....	80
Figure 4.13 SEM images of particle morphology at a) 20cm b) 25cm and c) 30cm distance from the collector.....	81
Figure 4.14 Particle size distribution vs. distance from collector.....	81
Figure 4.15 SEM images of particle morphology at a) 20KV b) 25KV and c) 30KV voltage.....	82
Figure 4.16 Particle size distribution vs. voltage	83

Figure 4.17 SEM images of particle morphology at a) 25 psi b) 30 psi and c) 35 psi air pressure	84
Figure 4.18 Particle size distribution vs. air pressure	84
Figure 4.19 BET analysis of HD, LD and MD	85
Figure 4.20 TGA analysis 12 μ m, 20 μ m and 7 μ m	86
Figure 4.21 TGA analysis of MD, HD and LD	86
Figure 4.22 Initial capacity-voltage profile particle additive and direct deposit	88
Figure 4.23 EDX image of silicon and carbon distribution a) particle additive b) direct deposit electrode	88.
Figure 4.24 Nyquist plot of impedance data comparison a) before formation b) after formation between particle additive and direct deposit	89
Figure 4.25 Cycle performance of particle additive and direct deposit.....	90
Figure 4.26 Rate capability of particle additive and direct deposit	90
Figure 4.27 Initial capacity-voltage profile of 12 μ m, 20 μ m and 7 μ m	92
Figure 4.28 Nyquist plot for impedance data for 20 μ m, 7 μ m, and 12 μ m.....	92
Figure 4.29 Cycle performance of 7 μ m, 20 μ m and 12 μ m	94
Figure 4.30 Rate capability of 20 μ m, 12 μ m and 7 μ m	94
Figure 4.31 initial capacity-voltage profiles of HD, LD and MD	96
Figure 4.32 Cycle performance of LD, MD and HD	97
Figure 4.33Rate capability performances of LD, HD and MD	97

CHAPTER 5

Figure 5.1 In-situ dilatometer measuring thickness change evolution with time...	105
Figure 5.2 SEM image of cross section of CP11/SF6/GNR electrode	106
Figure 5.3 Schematic illustrating step 1 of the modified Particle additive method...	108

CHAPTER 1

INTRODUCTION

1.1 Introduction

The dependence of humans on technology has been constantly increasing as the technology is now available to the humans easily. Availability of cost-effective energy has, thus, become an essential part of human lives. United States is one of the largest consumer of energy and about 80% of the energy consumed, in the year 2018, i.e. 81 quadrillion Btu comes from fossil fuels like petroleum, natural gas and coal[1]. Not only are these resources finite but fossil fuels have a lot of harmful effects from their extraction, transportation as well as from burning fossil fuels which leads to global warming and their wastage[2]. This over-reliance on fossil fuels will lead to several long-term negative effects on the health of humans as well as our planet. However the recognition of renewable energy resources as a better alternative compared to fossil fuels has been gaining momentum.

Renewable energy resources are those energy resources which can be utilized repeatedly over a period of time such as solar energy, wind energy, biomass energy ect[3]. The issue with renewable energy resources, however, is that they are intermittent and hence not available at all times. This creates a need for energy storage because of the associated intermittent characteristics of the renewable energy resources. Therefore there has been a transition from harvesting energy from renewable resources towards storage of this energy which opens up a whole new market for energy storage technologies. Batteries have been widely tipped as the

answer to the energy storage problem. In addition to the fact that batteries possess the ability to store energy batteries have been around for centuries and hence batteries have largely been used for large scale energy storage from sustainable sources of energy. All batteries consist of two electrodes connected by an ionically conducting liquid called electrolyte. The electrodes are maintained at different potentials. When the electrodes are connected externally by a device ions flow through the electrolyte from the more positive electrode to the more negative electrode and the electrons flow in an opposite direction and the resulting electrical energy is trapped by the external circuit[4]. There have been a lot of batteries with various chemistries in the past. However in the recent past lithium ion batteries have emerged as the batteries of choice especially for applications involving the transportation and the electronic sectors. This is due to the high energy and power density offered by lithium ion batteries as well as a range of chemical potentials available due to various different designs[5]. Conventionally Li-ion batteries have Graphite as an anode[6] and a layered metal oxide such as LiCoO_2 as cathode[7]. There have been enhancements in the energy and power densities of Li-ion batteries by improvements in the separator design processes[8] as well as by tuning the properties of the electrolyte by addition of different additives such as vinylene carbonate[9] however for applications like electric vehicles there has to be a dramatic increase in the energy and power densities in Li-ion batteries [10].

One of the major ways to achieve this is by using a different chemistry for anode or the cathode of the Li-ion battery. There has been a lot of research in finding the right anode for Li-ion batteries since carbon has been the standard anode since the

conception of Li-ion batteries as opposed to various changes in the cathode material. One of the earliest candidates was LiAl alloy anode which was capable of providing good columbic efficiencies but this was only when it was restricted to low current densities ($1\text{mA}/\text{cm}^2$) [11]. One of the other chemistries that were trialed used tungsten dioxide as the anode which gave highly reversible Li-ion insertion but resulted in external lithiation when used in a full cell as well as giving lower capacities[11].

The research into finding the right anode is divided into 3 chemistries namely conversion, intercalation and alloying reactions of the anode with the lithium. The mainly studied intercalation anodes are graphite and $\text{Li}_4\text{Ti}_5\text{O}_{12}$ [12]. In both the anodes the Li- ions undergo insertion between layers of the crystal structure during charging and deintercalation during discharging. LTO has several advantages such as stress free reversible lithium intercalation, favorable lithium potential of 1.5V [13] as well as good rate capability performance[14], however, it suffers from poor energy density due to its lower specific capacity[12], [13]. Graphite till now has been the most promising intercalation anode and is known to intercalate with various ions[15] and has also been tested in an electrochemical battery system relatively early on[16]. It has a theoretical specific energy capacity of 360-372mAh/g depending on the route of synthesis of the graphite[17] and has shown good rate capability[18].

The second class of anode chemistries was explored was that of conversion reactions where the electrode is made up of nanoparticles of transition metal oxides such as Cobalt oxide, Copper oxide, Nickel oxide and Iron oxide as well as fluorides and phosphides. These metal oxide nanoparticles are reduced when they react with lithium which leads to the formation of Li_2O . These electrodes have demonstrated capacities

of 700mAh/g up to two times higher than intercalation based graphite anodes[19]. However these anodes have a lot of problems which have limited their commercialization such as huge voltage hysteresis, volume changes during cycling, low first cycle columbic efficiencies as well as limited applicability at higher temperatures[20].

The third class of anode chemistry involves alloying reactions. The most prominent negative electrodes that reversibly alloy with lithium to form high capacity rechargeable lithium ion batteries are Silicon and Tin which are capable of delivering specific capacities up to 4200mAh/g and 900mAh/g respectively[12]. In this work our focus has been on silicon as the material for anode. Silicon provides several attractions besides the high gravimetric theoretical capacity ($\text{Li}_{4.4}\text{Si}$ lithiated state) such as its abundance (second most common element in earth's crust), sound infrastructure due to the semi-conductor industry, reasonable discharge voltage, and employability at room temperature, relatively cheap as well as environmentally benign and non-toxic[21]. However Silicon undergoes huge volume expansion (around 310%) [22] because of its inherent ability to store a lot of lithium ions which leads to huge stress creation over a number of cycles of lithiation and delithiation [21]. This creation of huge stress leads to pulverization of the electrode material as well as detachment of the active material from the collector resulting in electrical isolation of silicon [23,24]. Solid electrolyte interphase is typically formed at potentials less than 1V which is a passivating layer but due to the repeated volume changes the SEI layer is broken down over a number of cycles resulting thicker SEI and higher impedance [24,25]. All these steps occur in a synergistic way and lead to rapid failing of the silicon based anodes[21]. Apart from

these issues Silicon has inherently low electrical conductivity[26] which impedes its use in high power density or rate capability applications.

There has been a lot of work done in the past decade to solve these issues ranging from synthesizing silicon nanostructures to reduce the pulverization of the silicon[27], making composites with carbonaceous materials to alleviate the stress as well as provide a conductive network[28, 29], applying coatings of different materials to combat the resulting stress from the volume expansion[30,31], and creating porous electrode structures to provide room for the silicon to expand[32,33].

In this thesis attempts have been made to address all the different modes of failure associated with silicon anodes with a special emphasis on controlling the volume expansion of the silicon anodes. We hypothesize that volume expansion of silicon is the major mode of failure of silicon based anodes that contributes to the other modes of failure. Hence we explored several material processing strategies on combating this issue of volume expansion which is our main focus. Also an equal emphasis was placed on making the electrode fabrication process cost-effective, scalable and environmentally friendly.

1.2 Air-Controlled Electrospray

The process of choice employed in this study is air controlled electrospray. The process of electrospinning is widely known and already industrialized. In electrospinning a polymer solution is subjected to a sufficient voltage source and drawn out of a needle as jet which travels a certain distance to the collector and solidifies as it reaches the collector to form polymer fibers[34]. It has been used by

several research groups to fabricate porous nanofiber composite silicon electrodes because of the simple and environmentally friendly nature of the manufacturing technique that gives porous silicon nanofiber mats[35] . Despite several advantages this process is time consuming as well as gives lower volumetric energy density and hence we used Air controlled electro spray process which retained all the advantages associated with electrospinning but is a lot faster because of the addition of air pressure and thus scalable and at the same time gives porous film as opposed to porous nanofiber mats thus increasing the energy density [29]. In air controlled electro spraying, a voltage source is applied to the inner nozzle which breaks up the solution into small jets and additionally an air pressure is applied to the outer nozzle to further break up these jets into smaller particles which is then directly deposited onto the copper collector to form a film of the electrode.

In chapter 1 of this work a solution of silicon, graphene, polyimide (PI), polyvinyl alcohol (PVA), and graphene nanoribbons (GNR) was pumped through the nozzle and under the influence of electric field and air pressure to obtain directly deposited high silicon content electrodes. The resulting electrodes were then subjected to a heat treatment to thermally degrade PVA and hence create micropores as well as mesopores to accommodate the volume expansion during successive cycles of lithiation and de-lithiation. The GNR was added to provide a conductive pathway between the silicon inside these voids and the graphene sheets. The effect of pores and GNR was isolated to study the contribution of both individually in targeting different modes of failure of high silicon based loading electrodes.

Case 1 of this chapter compares the effect of void spaces created by thermally removing PVA by comparing it with a control electrode having the exact same composition obtained without the use of a sacrificial polymer. The electrode with pores shows much better cyclability compared to control which highlights the effect of the porous structure in controlling volume expansion. Case 2 of this chapter compares the effect of GNR by comparing it with a control having similarly porous structure but absence of GNR. The electrode with the GNR shows a much higher capacity as well suggesting better silicon activation as well as better rate capability highlighting the effect of GNR in providing conductive pathway.

In chapter 2 of this thesis Silicon/Graphite composites were electrosprayed which resulted in directly deposited moderate silicon content electrodes. Two kinds of graphite namely CP11 which is spherical and has an average diameter of 11 μ m and SF6 which is plate like and has an average diameter of 6 μ m were investigated. It was found that while, SF6 gave better capacity due to its smaller plate like structure activating more silicon, CP11 gave better rate capability due to its compact packing. Combining these two types of graphite was found to give the most optimized cell performance by retaining the individual properties of both kinds of graphite.

In chapter 3 of this thesis a unique assembly of silicon/graphite composites is put forward with relatively lower silicon content which builds on the work one in chapter 1 and chapter 2 by combining them. First Si/PI/Graphene solution was prepared and electrosprayed in a similar way as done in chapter 1 onto an aluminum collector. It was then scratched off the collector to form Si/PI/Graphene particles. These particles were then mixed with a solution of CP11 and SF6 in a similar way as done in chapter 2 and

directly sprayed onto the copper collector. This two step particle additive approach was compared with a directly deposited one step control. The particle additive approach showed a higher capacity as well as better cycling and rate capability highlighting the advantages of the unique architecture achieved via this two step approach. Further the morphology of the particles, so formed, is highly tunable resulting in different size and porosity by changing the various electro spraying parameters. Further the effect of the morphology of the particles on the electrochemical performance was investigated.

The work done in this thesis progresses from a very high level of fundamental relevance in Chapter 1 to a very high level of industrial relevance in Chapter 3.

REFERENCES

- [1] “Good News, Bad News_ 4 Trends in US Energy Use _ World Resources Institute.” .
- [2] “The Hidden Costs of Fossil Fuels _ Union of Concerned Scientists.” .
- [3] N. L. Panwar, S. C. Kaushik, and S. Kothari, “Role of renewable energy sources in environmental protection : A review,” *Renew. Sustain. Energy Rev.*, vol. 15, no. 3, pp. 1513–1524, 2011.
- [4] M. Armand and J. Tarascon, “Building better batteries,” vol. 451, no. February, pp. 2–7, 2008.
- [5] T. Kim, “and hybridized technologies,” pp. 2942–2964, 2019.
- [6] T. U. Miinchen and W. Germany, “THE ELECTROCHEMICAL PREPARATION AND PROPERTIES OF IONIC ALKALI METAL- AND NR , GRAPHITE INTERCALATION COMPOUNDS IN ORGANIC ELECTROLYTES,” vol. 14, no. 1, pp. 111–115, 1976.
- [7] R. April and C. J. B. Goodenough, “A NEW CATHODE MATERIAL FOR BATTERIES OF HIGH ENERGY DENSITY,” vol. 15, no. c, pp. 783–789, 1980.
- [8] H. Lee, M. Yanilmaz, O. Toprakci, K. Fu, and X. Zhang, “Environmental Science separators for rechargeable lithium-ion batteries,” pp. 3857–3886, 2014.
- [9] L. Chen, K. Wang, X. Xie, and J. Xie, “Effect of vinylene carbonate (VC) as electrolyte additive on electrochemical performance of Si film anode for lithium ion batteries,” vol. 174, pp. 538–543, 2007.
- [10] E. Environ, “Environmental Science going beyond , lithium-ion batteries,” pp. 7854–7863, 2012.
- [11] M. Li, J. Lu, Z. Chen, and K. Amine, “30 Years of Lithium-Ion Batteries,” vol. 1800561, pp. 1–24, 2018.
- [12] E. Environ, “Environmental Science Challenges in the development of advanced Li-ion batteries : a review,” pp. 3243–3262, 2011.
- [13] J. M. Chem, R. Marom, S. F. Amalraj, N. Leifer, D. Jacob, and D. Aurbach, “FEATURE ARTICLE,” pp. 9938–9954, 2011.
- [14] Y. Tang, L. Yang, Z. Qiu, and J. Huang, “Template-free synthesis of mesoporous spinel lithium titanate microspheres and their application in high-rate lithium ion batteries †,” pp. 5980–5984, 2009.
- [15] I. Electrochemistry, “(Received 25th April 1974),” vol. 53, pp. 329–333, 1974.

- [16] Z. Jiang, M. Alamgir, and K. M. Abraham, "The Electrochemical Intercalation of Li into Graphite in Li / Polymer Electrolyte / Graphite Cells," vol. 142, no. 2, pp. 3–10, 1995.
- [17] M. Endo, C. Kim, K. Nishimura, T. Fujino, and K. Miyashita, "Recent development of carbon materials for Li ion batteries," vol. 38, pp. 183–197, 2000.
- [18] H. Buqa, D. Goers, M. Holzapfel, and M. E. Spahr, "High Rate Capability of Graphite Negative Electrodes for Lithium-Ion Batteries," pp. 474–481, 2005.
- [19] P. Poizot, S. Laruelle, S. Grugeon, L. Dupont, and J. Tarascon, "Nano-sized transition-metal oxides as negative-electrode materials for lithium-ion batteries," vol. 407, no. September, 2000.
- [20] S. Yu, S. H. Lee, D. J. Lee, and Y. Sung, "Conversion Reaction-Based Oxide Nanomaterials for Lithium Ion Battery Anodes," no. 16, pp. 2146–2172, 2016.
- [21] X. Zuo, J. Zhu, P. Müller-buschbaum, and Y. Cheng, "Nano Energy Silicon based lithium-ion battery anodes : A chronicle perspective review," *Nano Energy*, vol. 31, no. November 2016, pp. 113–143, 2017.
- [22] L. Y. Beaulieu, K. W. Eberman, R. L. Turner, and L. J. Krause, "Colossal Reversible Volume Changes in Lithium Alloys," vol. C, pp. 7–10, 2001.
- [23] J. H. Ryu, J. W. Kim, Y. Sung, and S. M. Oh, "Failure Modes of Silicon Powder Negative Electrode in Lithium Secondary Batteries," pp. 306–309, 2004.
- [24] H. Wu and Y. Cui, "Designing nanostructured Si anodes for high energy," pp. 414–429, 2012.
- [25] J. M. Chem *et al.*, "The failure mechanism of nano-sized Si-based negative electrodes for lithium ion batteries," no. Cmc, pp. 6201–6208, 2011.
- [26] M. Ashuri and L. L. Shaw, "batteries : where size , geometry and structure," pp. 74–103, 2016.
- [27] C. K. Chan *et al.*, "High-performance lithium battery anodes using silicon nanowires," pp. 31–35, 2007.
- [28] N. Liu *et al.*, "A pomegranate-inspired nanoscale design for large-volume-change lithium battery anodes," *Nat. Nanotechnol.*, vol. 9, no. 3, pp. 187–192, 2014.
- [29] L. Fei *et al.*, "Graphene Oxide Involved Air-Controlled Electrospray for Uniform, Fast, Instantly Dry, and Binder-Free Electrode Fabrication," *ACS Appl. Mater. Interfaces*, vol. 9, no. 11, pp. 9738–9746, 2017.
- [30] B. Y. Yu, L. Gu, C. Zhu, S. Tsukimoto, P. A. Van Aken, and J. Maier, "Reversible Storage of Lithium in Silver-Coated Three-Dimensional Macroporous Silicon," pp. 2247–2250, 2010.
- [31] L. Luo *et al.*, "Surface Coating Constraint Induced Self-Discharging of Silicon Nanoparticles as Anodes for Lithium Ion Batteries," *Nano Lett.*, vol. 15, no. 10,

pp. 7016–7022, 2015.

- [32] L. Wu, J. Yang, X. Zhou, M. Zhang, Y. Ren, and Y. Nie, “Silicon nanoparticles embedded in a porous carbon matrix as a high-performance anode for lithium-ion batteries,” pp. 11381–11387, 2016.
- [33] Q. Xiao *et al.*, “Inward lithium-ion breathing of hierarchically porous silicon anodes,” *Nat. Commun.*, vol. 6, pp. 1–8, 2015.
- [34] Z. Huang, Y. Zhang, M. Kotaki, and S. Ramakrishna, “A review on polymer nanofibers by electrospinning and their applications in nanocomposites,” vol. 63, pp. 2223–2253, 2003.
- [35] Y. Zhmayev, S. Pinge, G. Shoorideh, and G. L. Shebert, “Controlling the Placement of Spherical Nanoparticles in Electrically Driven Polymer Jets and its Application to Li-Ion Battery Anodes,” pp. 5543–5553, 2016.

CHAPTER 2

DIRECT DEPOSIT POROUS HYBRID SILICON ANODES FOR SCALABLE AND HIGH PERFORMANCE LITHIUM ION BATTERIES

2.1 Introduction

The current state of art lithium ion battery technology is at its limit and thus a significant upgrade in terms of gravimetric and volumetric energy density is the need of the hour especially for applications such as Electric Vehicle[1][2][3][4]. Silicon anode has been one of the most promising alternatives to the conventional graphite anode due to its high theoretical gravimetric capacity of about 4200mAh/g[5][6][7]. However Silicon undergoes huge volume expansion because of its inherent ability to store a lot of lithium ions which leads to huge stress creation over a number of cycles of lithiation and delithiation. This creation of huge stress leads to pulverization of the electrode material as well as detachment of the active material from the collector resulting in electrical isolation of silicon. Solid electrolyte interphase is typically formed at potentials less than 1V which is a passivating layer but due to the repeated volume changes the SEI layer is broken down over a number of cycles resulting thicker SEI and higher impedance. All these steps occur in a synergistic way and lead

to rapid failing of the silicon based anodes. Apart from these issues Silicon has inherently low electrical conductivity which impedes its use in high power density or rate capability applications[8][9][10][11][12][13][14].

To overcome these obstacles various different strategies have been explored. Coatings of various materials such as conductive polymers[15] [16] help to provide a continuous conductive network and self healing polymers [17] which has the ability to recover by itself during repeated cycling. Silicon/Graphene hybrid anodes have been widely used because of the ability of graphene to not only provide excellent conductivity but also act as a mechanical buffer towards the silicon volume expansion and hence improve cycle life performance[18][19][20]. One of the most successful approach, however, has been using a silicon carbon based composites and engineering void spaces for the effective accommodation of silicon volume expansion[21][22][23][24][25]. The various approaches studied in the literature to create pore spaces invariably involve the use of an expensive fabrication method such as chemical vapour deposition(CVD) to create an assembly with a sacrificial template that is etched away later by using hydrofluoric acid[26][27][28]. This approach despite being largely successfully is not economic especially for a large scale production of such porous silicon/carbon composite structures and also the usage of hydrofluoric acid for etching render this process environmentally not suitable.

In our study we are using air-controlled electrospray method in order to facilitate a scalable and economic method of fabrication of silicon anodes. Fig 2.1 shows the schematic of our process. A solution of silicon, graphene, polyimide (PI), polyacrylic

alcohol (PAA), and graphene nanoribbons (GNR) was pumped through the nozzle and under the influence of electric field and air pressure to obtain directly deposited high silicon content electrodes. The resulting electrodes were then subjected to a mild heat treatment to thermally degrade PAA.. This approach provides the multiple advantages. First, graphene sheets provide structural integrity by imparting a compressive stress to counter the outward silicon volume expansion. Second, removal of PAA creates micropores as well as mesopores to accommodate the volume expansion during successive cycles of lithiation and de-lithiation. Third, the added GNR acts as a conductive pathway to ensure that the silicon inside the voids is electronically connected to the graphene sheets and also offers a pathway for shorter transport of the lithium ions.

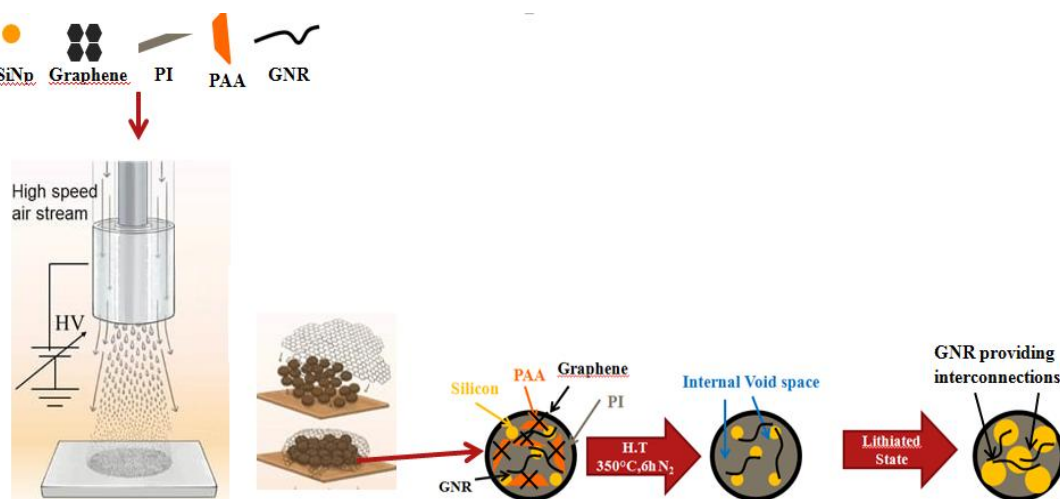


Fig 2.1 Schematic illustrating the fabrication process

To elucidate the effect of creation of the pores and its effect on mitigating volume expansion a control electrode was made involving the same steps except the thermal degradation of PAA. In this way there is no intentional creation of external pores hence the structure of the 2 electrodes is very different. The final composition of this control was kept the same as our process. This forms Case 1 of this chapter. In Case 2 another control was made with all the same steps except the addition of GNR. In this case the control has the external pore formation but without the addition of GNR. This was done to study the effect of GNR since the obtained structure of the electrode is the same but composition is slightly different due to the absence of GNR.

2.2 Experimental section

Preparation of DD Porous Silicon anodes with GNR via Air-controlled

Electrospray: 1.5g of PI (X) was dissolved in a mixture of 7.5g of NMP (Sigma Aldrich) and 7.5g of DMF (Sigma Aldrich) and left for stirring overnight. 1g of PAA (Sigma Aldrich) was dissolved in 10g NMP and left for overnight stirring. 0.35g of Silicon (US Research Nanomaterials c.a. 30-70nm) was dissolved in a mixture of 0.91g of NMP and 3.43g of DMF and left for sonication(X) for 1 hour to disperse the solution properly and prevent any aggregation. 0.758g of PI solution prepared previously was then added to this solution. 0.233g of PAA solution prepared previously was added to the above solution. The solution was stirred vigorously by a vortex stirrer. At this point 0.05g of GNR (EMD Performance Materials) was added to the mixture. Finally, 2.625g of a 4% by weight solution of Graphene in NMP (ACS) was added to the mixture. The solution was stirred vigorously and left overnight for

stirring. The solution was then pumped from a syringe at 0.01ml/min towards a copper collector at a distance of 20cm from the tip of the needle. 25KV of Voltage was applied to the system. Additionally 30psi of air pressure was applied to the system which resulted in the formation of Si/Gr/PI/PVA/GNR composite which was collected on the copper foil. As-sprayed copper electrode was then heat treated at 350°C at a ramp rate of 10°C/min for 6h in N₂ inert conditions. This resulted in formation of DD Si/PI/Gr/GNR electrode on the copper collector of the loading 0.3-0.5 mg/cm². Higher areal or mass loading can simply be achieved by longer spraying time or by using additional nozzles.

Preparation of DD Silicon anodes with GNR via Air-controlled Electro spray:

1.5g of PI (X) was dissolved in a mixture of 7.5g of NMP (Sigma Aldrich) and 7.5g of DMF (Sigma Aldrich) and left for stirring overnight. 0.35g of Silicon (US Research Nanomaterials c.a. 30-70nm) was dissolved in a mixture of 0.91g of NMP and 3.43g of DMF and left for sonication(X) for 1 hour to disperse the solution properly and prevent any aggregation. 0.775g of PI solution prepared previously was then added to this solution. The solution was stirred vigorously by a vortex stirrer. At this point 0.05g of GNR (EMD Performance Materials) was added to the mixture. Finally, 2.625g of a 4% by weight solution of Graphene in NMP (ACS) was added to the mixture. The solution was stirred vigorously and left overnight for stirring. The solution was then pumped from a syringe at 0.01ml/min towards a copper collector at a distance of 20cm from the tip of the needle. 25KV of Voltage was applied to the system. Additionally 30psi of air pressure was applied to the system which resulted in the formation of Si/Gr/PI/PVA/GNR composite which was collected on the copper

foil. As-sprayed copper electrode was then heat treated at 350°C at a ramp rate of 10°C/min for 6h in N₂ inert conditions. This resulted in formation of DD Si/PI/Gr/GNR electrode on the copper collector of the loading 0.3-0.5 mg/cm². Higher areal or mass loading can simply be achieved by longer spraying time or by using additional nozzles.

Preparation of DD Porous Silicon anodes without GNR via Air-controlled Electro spray:

1.5g of PI (X) was dissolved in a mixture of 7.5g of NMP (Sigma Aldrich) and 7.5g of DMF (Sigma Aldrich) and left for stirring overnight. 1g of PAA (Sigma Aldrich) was dissolved in 10g NMP and left for overnight stirring. 0.35g of Silicon (US Research Nanomaterials c.a. 30-70nm) was dissolved in a mixture of 0.91g of NMP and 3.43g of DMF and left for sonication(X) for 1 hour to disperse the solution properly and prevent any aggregation. 0.758g of PI solution prepared previously was then added to this solution. 0.233g of PAA solution prepared previously was added to the above solution. The solution was stirred vigorously by a vortex stirrer. Finally, 3.084g of a 4% by weight solution of Graphene in NMP (ACS) was added to the mixture. The solution was stirred vigorously and left overnight for stirring. The solution was then pumped from a syringe at 0.01ml/min towards a copper collector at a distance of 20cm from the tip of the needle. 25KV of Voltage was applied to the system. Additionally 30psi of air pressure was applied to the system which resulted in the formation of Si/Gr/PI/PVA/GNR composite which was collected on the copper foil. As-sprayed copper electrode was then heat treated at 350°C at a ramp rate of 10°C/min for 6h in N₂ inert conditions. This resulted in formation of DD Si/PI/Gr/GNR electrode on the

copper collector of the loading 0.3-0.5 mg/cm². Higher areal or mass loading can simply be achieved by longer spraying time or by using additional nozzles.

Material Characterization of the Directly Deposited Electrodes: Composite electrodes were characterized using a scanning electron microscope (SEM, Zeiss Gemini) and Energy Dispersive Spectroscopy (Bruker) to assess morphological changes. Thermogravimetric analysis (TGA, TA instruments Q500) was conducted on the electrodes to measure the silicon content.

Battery fabrication and electrochemical measurements of the directly deposited silicon electrodes: 2032 type coin cells were fabricated using the as directly deposited silicon composite as working electrode, Lithium metal disc (MTI) as counter electrode and a polyethylene separator (Cellgard) to test the performance of the half cells. A homemade electrolyte 1M LiPF₆ as the salt with dimethyl carbonate (Sigma), Ethylene methyl carbonate (Sigma), and diethyl carbonate (Sigma) was used as solvents in a ratio of 2:4:4 with 10% of fluoroethylene carbonate (Sigma) additive inside the half cells. Electrochemical properties of the cells were characterized by electrochemical impedance spectroscopy (PARASAT 4000, Princeton Applied Research) and cyclic voltammetry (CH Instruments, Potentiostat) and galvanostatic charge and discharge cycles (MTI). A voltage window of 0.01-1.5V Vs Li/Li⁺ were applied to the half cells.

2.3 Results and discussion

Material Characterization:

Morphology of the DD Si/PI/PAA/GNR/Gr anode after heat treatment is shown in figure 2.2. It is evident from the SEM images of 2.2a) there is visible formation of internal pores on the surface of the electrodes. This is further confirmed by comparing the Si/Gr/PI/PAA/GNR particles scratched from the anode before and after Heat treatment. The as-sprayed particles have 0D morphology where the silicon nanoparticles are encapsulated by Graphene sheets to form sphere like structures. After heat treatment the particles still maintain their structure but develop pores. Figure 2.3 a) shows the cross-sectional images of electrode after heat treatment where a lot external pore formation is visible. These pores are majorly micron-scale macropores which provide sufficient room to accommodate silicon volume expansion which prevents pulverization during cycling and maintains the electrode structure which is further boosted by graphene sheets providing sufficient mechanical support. Also the addition of GNR helps in ensuring that the silicon inside the void spaces is not electrically isolated. Fig 2.3 b) shows the corresponding cross –sectional image for Ref 1 where as is apparent the electrode structure is much denser compared to the PAA_REM which is due to no PAA removed in this case although all the other ingredients are the same. Fig 2.4 shows the corresponding cross-sectional images of the electrode with GNR and the reference electrode for Case 2 without GNR. It is evident that both the structures are highly porous because of the removal of PAA.

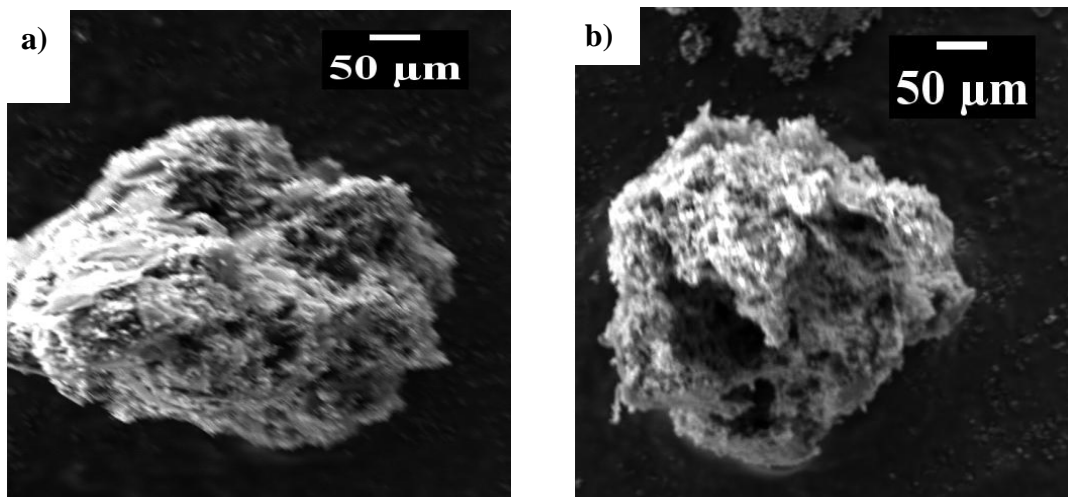


Figure 2.2 SEM image of (a) particle before heat treatment (b) particle after heat treatment

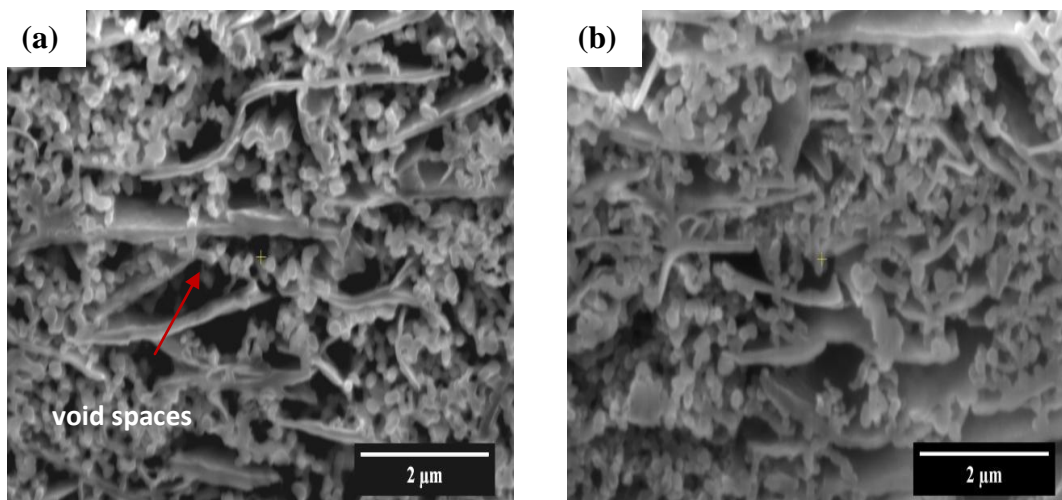


Figure 2.3 Cross section SEM image of (a) electrode after PAA removal
(b) reference electrode where no PAA is removed.

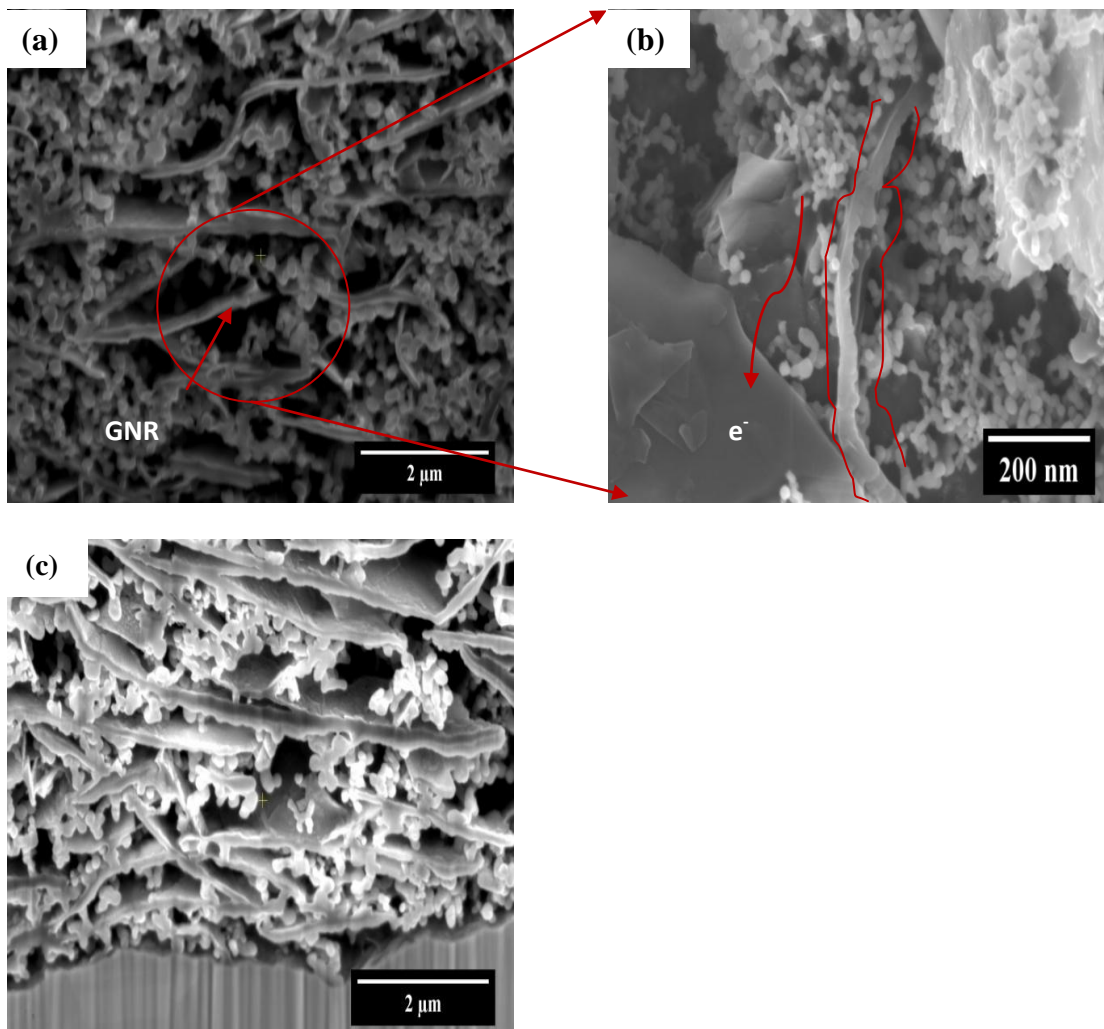


Figure 2.4 Cross- section SEM image of (a) electrode with GNR (b) Magnified image of GNR (c) reference electrode without GNR

The actual silicon content was calculated based on thermogravimetric analysis in figure 2.5. The silicon content before heat treatment was 67% and PAA was 5% but after heat treatment it becomes 70% which is due to the removal of PAA which is completely removed. Figure 2.6 and 2.7 show that the silicon content for both the

cases i.e. PAA_REM and its corresponding reference as well as GNR and its corresponding reference are the same which proves that difference in electrochemical performances is not due to different silicon, graphene or binder content. For the reference in case 2 GNR is replaced by equal amount of graphene.

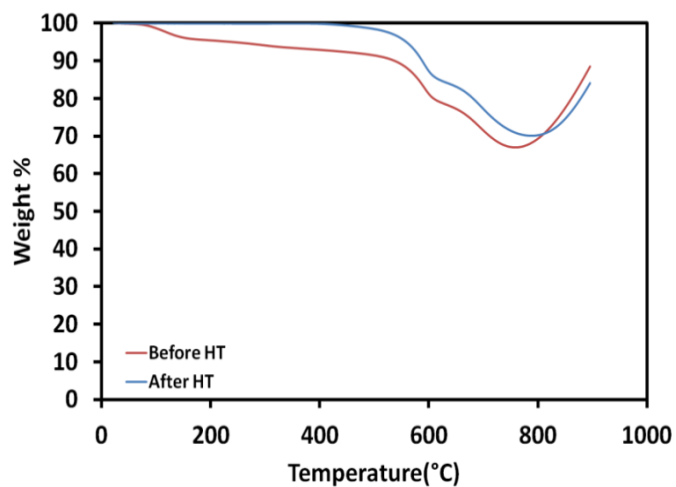


Figure 2.5 TGA analysis of before and after heat treatment

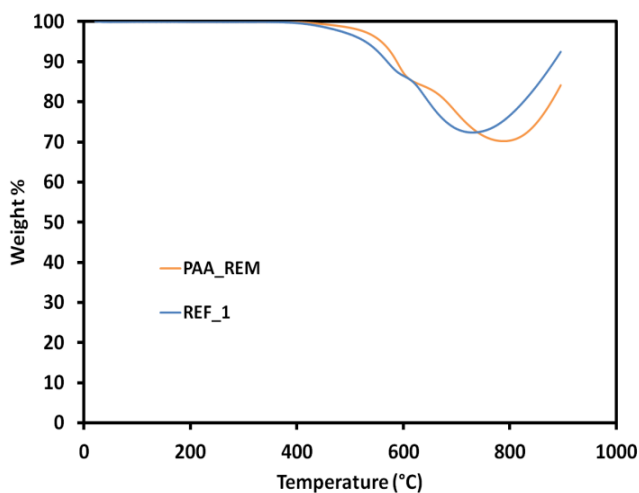


Figure 2.6 TGA analysis for PAA_REM and reference for case 1

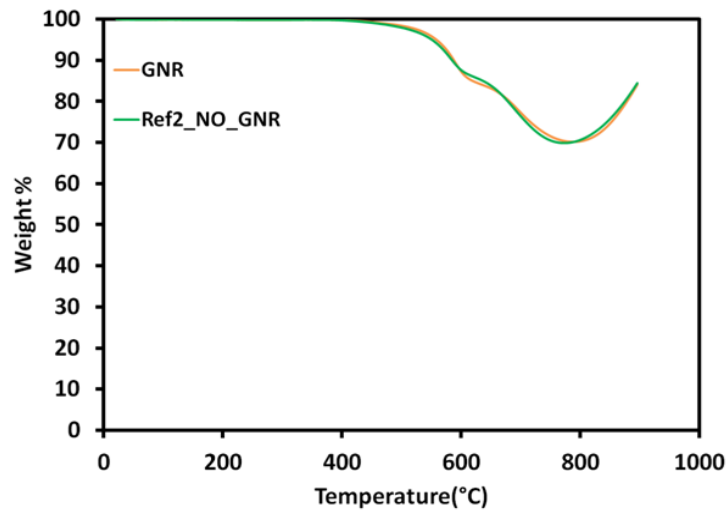


Figure 2.7 TGA analysis for GNR and reference for case 2

To characterize the pore size distribution Brunauer-Emmett-Teller (BET) and Porometry was used which shows the internal and external pores respectively. Figure 2.8 shows a comparison of the mesopores for PAA_REM and Ref1 system for Case 1. It is evident that there is not a significant difference in the mesopores for both the cases. This is possibly because of the existence of GNR between the voids created by thermally removing PAA. However there are some mesopores created for PAA_REM which is possibly due to the removal of PAA covering the silicon nanoparticles. Figure 2.9 shows comparison of the macropores between the PAA_REM and Ref1 as measured from Porometry. Here there is a clear difference showing the existence of micron sized pores for PAA_REM which is significantly more than the Ref1 which can be co-related to the voids seen in the SEM images in Figure 2.3. Figure 2.10 shows the BET comparison of GNR and NO_GNR for Case 2. The NO_GNR case as

a lot more mesopores compared to the GNR case despite thermal degradation of PAA in both cases which confirms our earlier assumption that the GNR occupies the void spaces created due to the removal of PAA. This will ensure that the silicon in the void spaces is not electrically isolated.

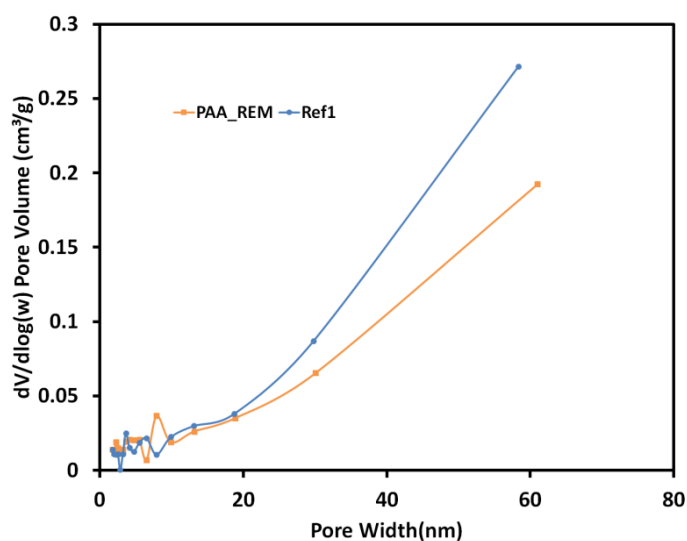


Figure 2.8 BET analysis of PAA_REM and reference for Case 1

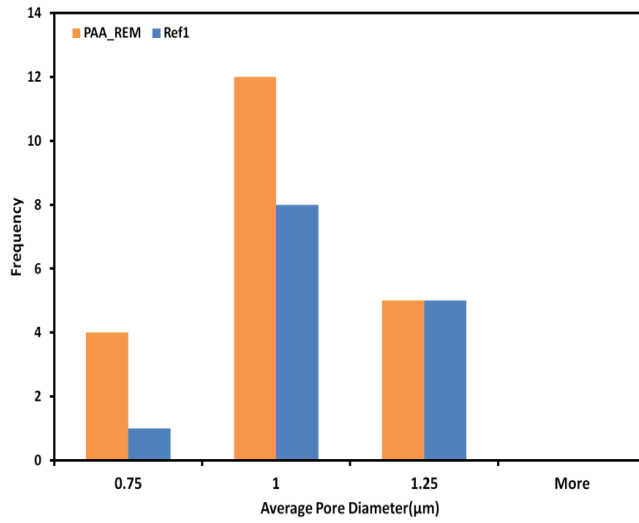


Figure 2.9 Porometry analysis of PAA_REM and reference for Case 1

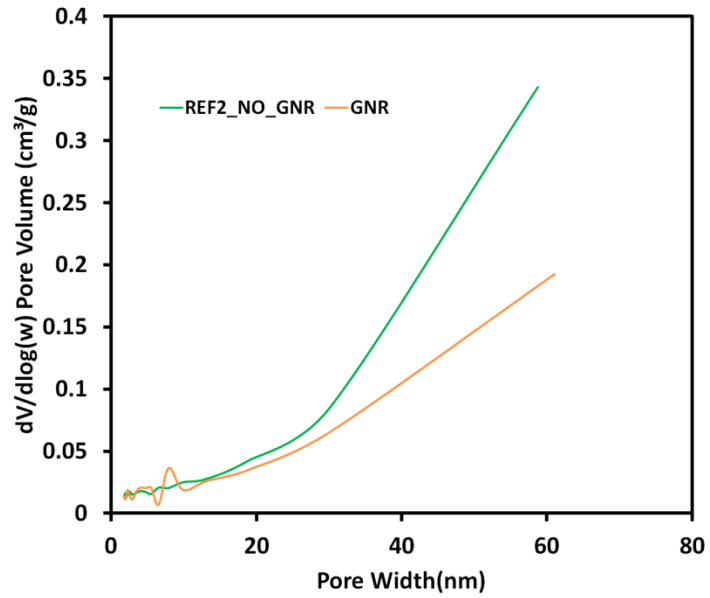


Figure 2.10 BET analysis of GNR and the reference for Case 2

Half-cell Electrochemical Performance:

To compare the electrochemical performance for Case 1 as well as Case 2 2032 coin type half cells were assembled. Each cell was lithiated to a voltage of 1.5V and delithiated to a voltage of 0.01V and made to undergo 5 formation cycles at 0.1C and then undergo deep charge discharge galvanostatic cycling with the 1st cycle at 0.1C, second cycle at 0.2C and the rest of the cycles at 0.3C and going back to 0.1C after 50 cycles at 0.3C to see the rate of recovery and same pattern was followed thereafter. The capacity-voltage graph for the formation cycle for case 1 is shown in Figure 2.11. For both PAA_REM and reference a characteristic flat plateau can be observed at around 0.25V for the discharge curve which corresponds to the formation of amorphous phase of Li_xSi from crystalline Si representing the alloying process[29][26]. The initial columbic efficiency for both PAA_REM and reference is very similar, 74.25 and 74.5 respectively, giving another confirmation of similar composition leading to similar electrochemical reactions. Also the capacities for both PAA_REM and Ref1 are very similar due to the similar composition. Figure 2.12 shows the cyclic voltammetry profile for case 1. The 1st peak corresponds to the formation of amorphous $\text{Li}_{13}\text{Si}_4$ phase i.e. partial lithiation. The 2nd peak corresponds to a completely lithiated $\text{Li}_{22}\text{Si}_5$ which results in most of the capacity. In a similar

manner for delithiation the same process occurs corresponding to the two peaks. The 1st peak shows the partial removal of Li⁺ ions to form Li_xSi_y phase and the second peak corresponds to complete delithiation to get back crystalline silicon[30][31][32]. Figure 2.13 and 2.14 are the corresponding capacity voltage profile and cyclic voltammetry profiles for case 2. It is evident from figure 2.13 and 2.14, similar to figure 2.11 and 2.12, the electrochemical reaction are very similar and initial columbic efficiencies are also very similar. However, GNR has a higher capacity than No_GNR because of the ability of GNR to provide electrical interconnections leading to a higher activation of silicon[33].

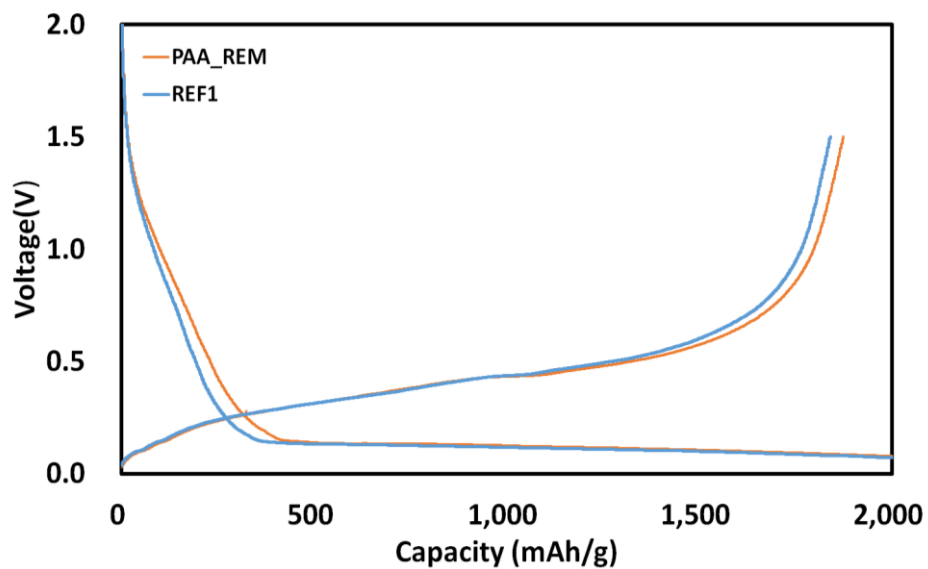


Figure 2.11 initial capacity voltage profiles of PAA_REM and Ref1

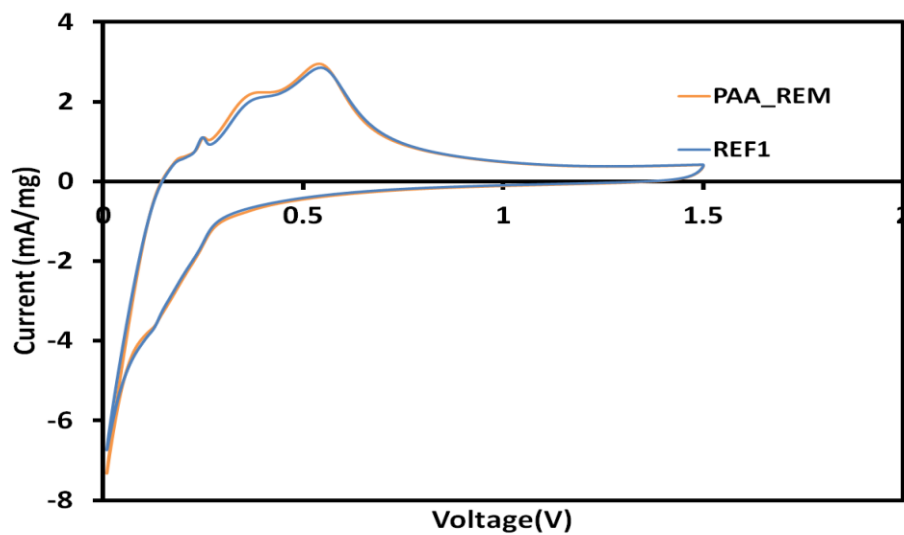


Figure 2.12 Cyclic voltammograms of PAA_REM and Ref1 at 1mV/s

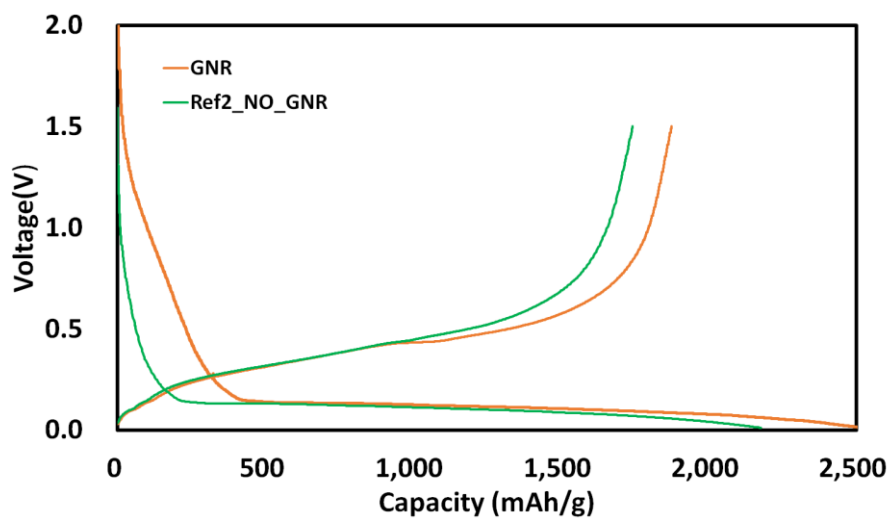


Figure 2.13 initial capacity voltage profiles of GNR and reference for case 2

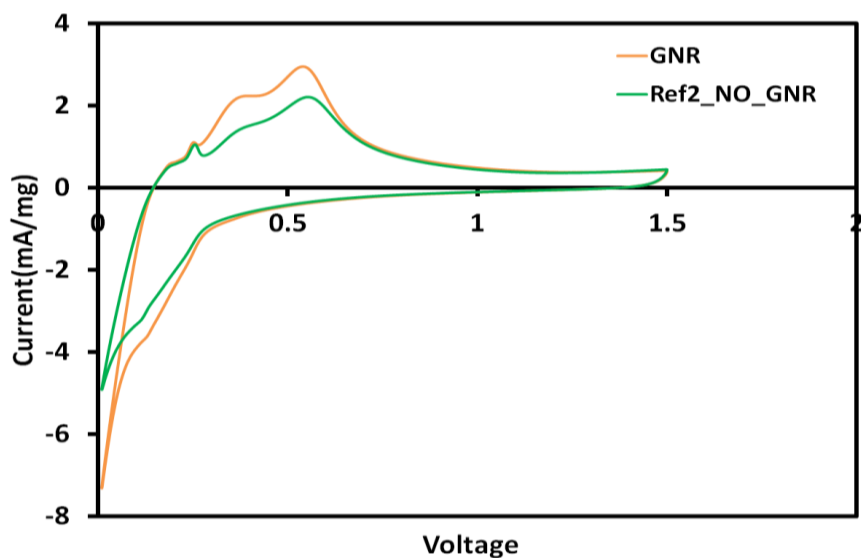


Figure 2.14 Cyclic voltammograms of GNR and reference for case 2

Figure 2.15 shows evolution of electrochemical impedance spectroscopy for Case 1. As shown in figure 2.15 a) before formation the charge transfer resistance (R_{ct}) for PAA_REM is higher because of its porous surface. However with more cycles the charge transfer resistance of Ref1 starts to increase and the difference with the PAA_REM is far lesser. Figure 2.16 shows EIS before formation for case 2. It is evident that addition of GNR decreases the overall charge transfer resistance.

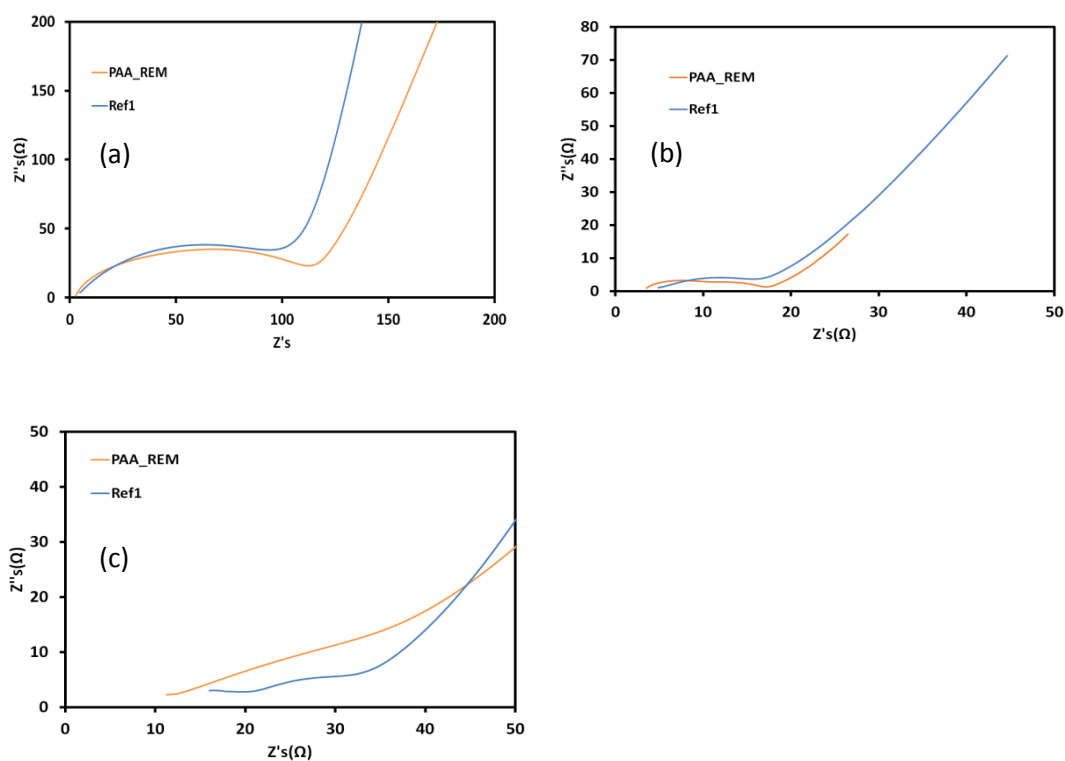


Figure 2.15 Nyquist plots of impedance data for case 1 a) before formation b) after formation c) after cycling

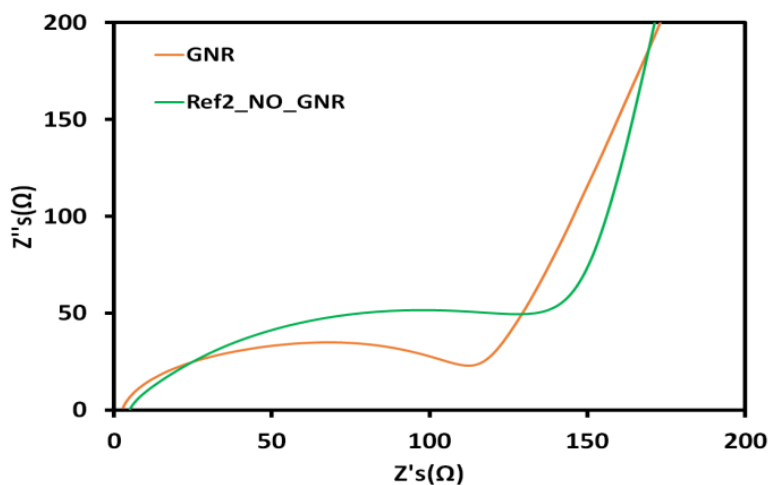


Figure 2.16 Nyquist plot of impedance data for case 2 before formation

The cyclic performance for case 1 is represented by Figure 2.17. The first cycle is at 0.1C, the second cycle is at 0.2C and the rest of the 50 cycles are at 0.3C and this procedure is repeated over a number of cycles. All the capacities in this work are reported on the basis of total mass including the conductive additive and binder. The lithiation capacity for PAA_REM is 1720 mAh/g while that for Ref1 is 1690mAh/g. The similar values are expected because of the similar composition for case 1. However after 400 cycles of deep charge/discharge the capacity retention for PAA_REM is about 50% and the same for Ref1 is 35%. The better retention for the PAA_REM is associated with the porous structure which is able to accommodate the volume expansion of silicon[34]. Figure 2.18 shows the cycle life performance for case 2. The lithiation capacity for GNR is 1720mAh/g while that for the reference without the GNR is 1610mAh/g. This increase in the capacity due to the addition of

GNR is due to its ability to act as a very good conducting agent for SiNp[33]. Also GNR participates in the electrochemical reaction at the surface which further boosts the capacity[35][36]. After 325 cycles of deep charge/discharge cycle retention for GNR is 50% and for the reference without GNR is 42% which highlights the importance of GNR in electrically connecting the isolated SiNp inside the voids.

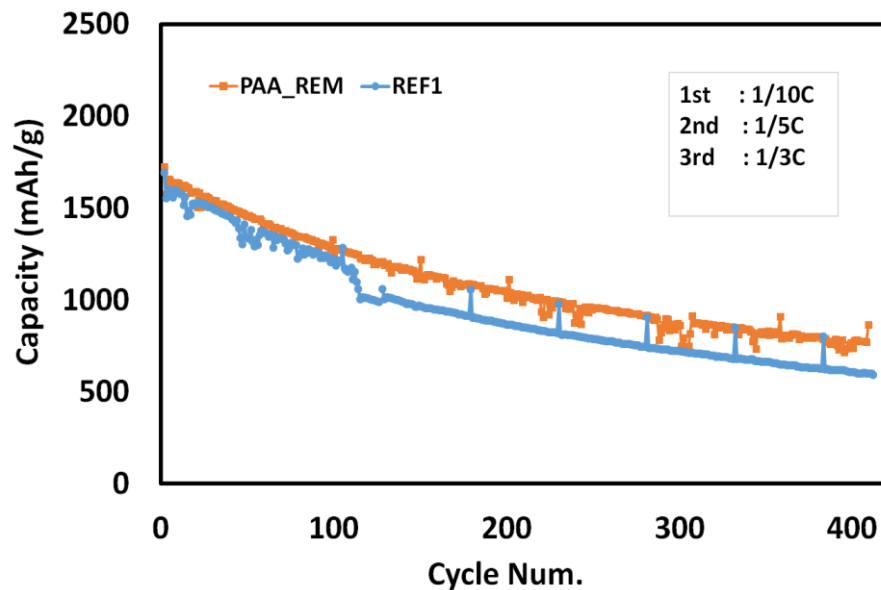


Figure 2.17 Cyclic performance of PAA_REM and reference for case 1

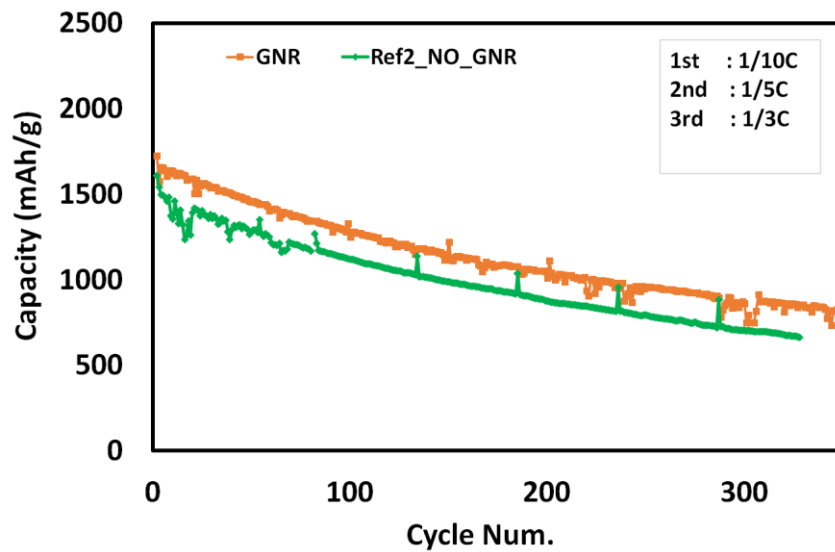


Figure 2.18 Cyclic performance GNR and reference for case

Figure 2.19 and 2.20 shows the rate capability performance for case 1 and 2 respectively. It is clear from figure 2.19 that until 1C there is not a significant difference in capacity for PAA_REM and REF1 but at 2C the capacity for the reference is lower than PAA_REM. This is possibly because of the ease of Li-ion diffusion into the porous structure especially at higher currents[25]. Figure 2.20 exemplifies the advantage of having GNR in not only giving a higher capacity at lower C rates but also retaining its superior capacity at higher C rates which is possible because of the role of GNR in providing shorter diffusional length and better facilitating the transport for Li-ions which is essential especially at faster rates [33].

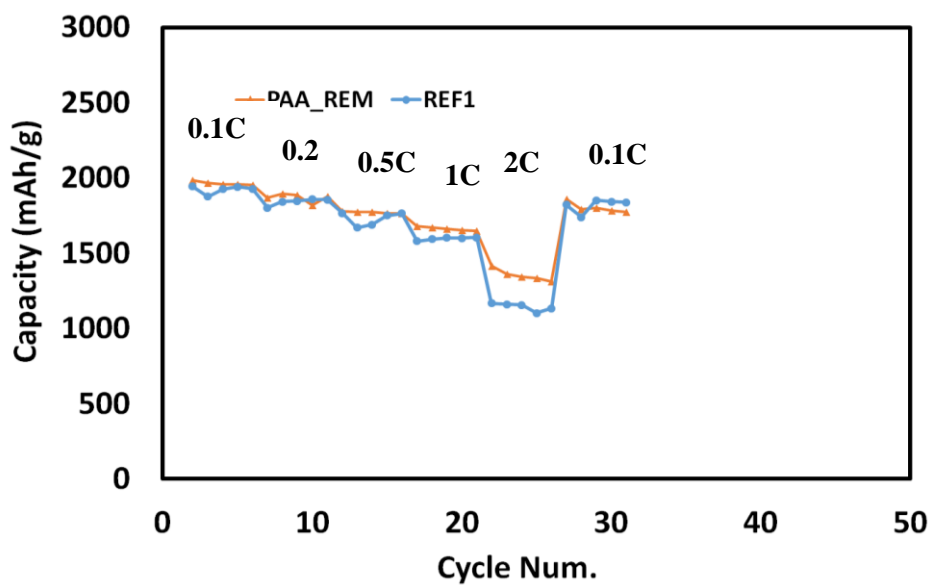


Figure 2.19 Rate capabilities of PAA_REM and reference for Case 1

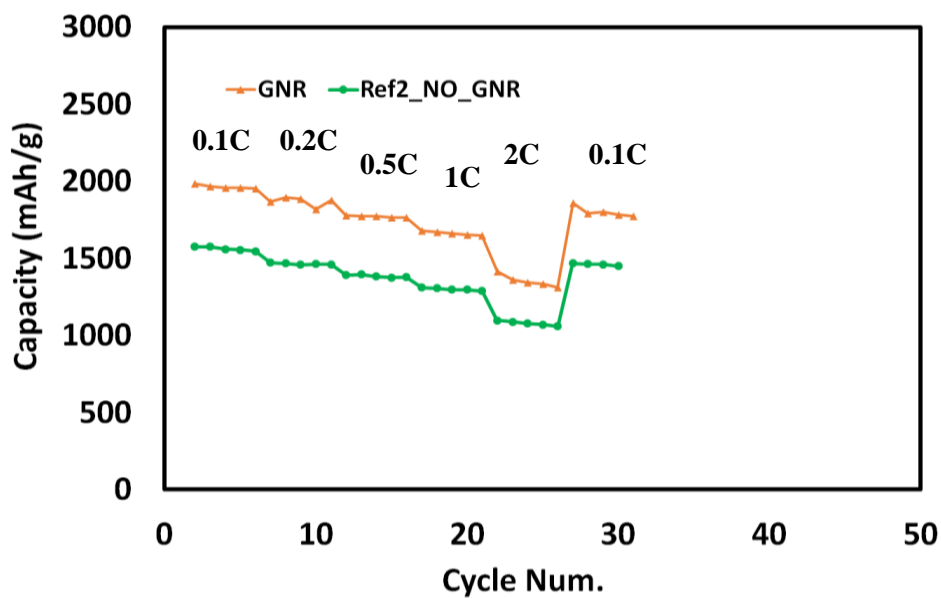


Figure 2.20 Rate capabilities of GNR and reference for case 2

2.4 Conclusion

In summary, directly deposited porous silicon anodes have been fabricated via air-controlled electrospray. A mild heat treatment at 350°C leads to the degradation of PAA which facilitates the creation of macropores which accommodates the silicon volume expansion thus preserves the electrode structure. This is different from most of the other approaches which require a harsh heat treatment for carbonization or formation of a sacrificial silicon oxide layer. Also by using thermal degradation to remove the sacrificial layer in this study makes it environmentally friendly compared to other cases which use HF etching. GNR has been employed in this study to ensure the SiNp in the voids are electrically not isolated and form a conductive bridge between the graphene sheets and the voids. To study the effect of the pores and GNR individually two cases are discussed. Case 1 shows similar capacity for the electrode with the pores and without the pores confirming similar composition but shows much better cyclic performance confirming the hypothesis that the performance is different because of the voids mitigating the silicon volume expansion. Case 2 shows that the electrode with GNR has a higher capacity compared to the electrode without GNR due to better activation of SiNp due to its ability to form conductive pathways to electrically connect the SiNp inside the voids. The electrode with GNR also shows a better rate capability highlighting the role of GNR in shortening the diffusion transport pathways.

REFERENCES

- [1] M. Armand and J. Tarascon, "Building better batteries," vol. 451, no. February, pp. 2–7, 2008.
- [2] B. Dunn, H. Kamath, and J. Tarascon, "for the Grid : A Battery of Choices," vol. 334, no. November, pp. 928–936, 2011.
- [3] P. G. Bruce, B. Scrosati, and J. Tarascon, "Lithium Batteries Nanomaterials for Rechargeable Lithium Batteries ** Angewandte," pp. 2930–2946, 2008.
- [4] M. Li, J. Lu, Z. Chen, and K. Amine, "30 Years of Lithium-Ion Batteries," vol. 1800561, pp. 1–24, 2018.
- [5] E. Environ, J. R. Szczech, and S. Jin, "Energy & Environmental Science Nanostructured silicon for high capacity lithium battery anodes †," pp. 56–72, 2011.
- [6] N. S. Hochgatterer *et al.*, "Silicon / Graphite Composite Electrodes for High-Capacity Anodes : Influence of Binder Chemistry on Cycling Stability," pp. 76–80, 2008.
- [7] J. P. Maranchi, A. F. Hepp, and P. N. Kumta, "High Capacity , Reversible Silicon Thin-Film Anodes for Lithium-Ion Batteries," pp. 198–201, 2016.
- [8] X. Zuo, J. Zhu, P. Müller-buschbaum, and Y. Cheng, "Nano Energy Silicon based lithium-ion battery anodes : A chronicle perspective review," *Nano Energy*, vol. 31, no. November 2016, pp. 113–143, 2017.
- [9] L. Y. Beaulieu, K. W. Eberman, R. L. Turner, and L. J. Krause, "Colossal Reversible Volume Changes in Lithium Alloys," vol. C, pp. 7–10, 2001.
- [10] J. H. Ryu, J. W. Kim, Y. Sung, and S. M. Oh, "Failure Modes of Silicon Powder Negative Electrode in Lithium Secondary Batteries," pp. 306–309, 2004.
- [11] H. Wu and Y. Cui, "Designing nanostructured Si anodes for high energy," pp. 414–429, 2012.
- [12] J. M. Chem *et al.*, "The failure mechanism of nano-sized Si-based negative electrodes for lithium ion batteries," no. Cmc, pp. 6201–6208, 2011.
- [13] M. Ashuri and L. L. Shaw, "batteries : where size , geometry and structure," pp. 74–103, 2016.
- [14] C. K. Chan *et al.*, "High-performance lithium battery anodes using silicon nanowires," pp. 31–35, 2007.

- [15] H. Wu *et al.*, “conformally coat silicon nanoparticles,” *Nat. Commun.*, vol. 4, pp. 1943–1946, 2013.
- [16] E. Environ, “Environmental Science Improving the cycling stability of silicon nanowire anodes with conducting polymer coatings †,” pp. 7927–7930, 2012.
- [17] C. Wang, H. Wu, Z. Chen, M. T. Mcdowell, Y. Cui, and Z. Bao, “operation of silicon microparticle anodes for,” *Nat. Chem.*, vol. 5, no. 12, pp. 1042–1048, 2013.
- [18] H. Xiang *et al.*, “Graphene / nanosized silicon composites for lithium battery anodes with improved cycling stability,” vol. c, pp. 0–9, 2011.
- [19] J. Ren, Q. Wu, G. Hong, W. Zhang, and H. Wu, “Silicon – Graphene Composite Anodes for High-Energy Lithium Batteries,” vol. 60439, pp. 77–84, 2013.
- [20] S. Chen, M. L. Gordin, R. Yi, G. Howlett, H. Sohn, and D. Wang, “Silicon core-hollow carbon shell nanocomposites with tunable buffer voids for high capacity anodes of lithium-ion batteries,” *Phys. Chem. Chem. Phys.*, vol. 14, no. 37, pp. 12741–12745, 2012.
- [21] L. Wu, J. Yang, X. Zhou, M. Zhang, Y. Ren, and Y. Nie, “Silicon nanoparticles embedded in a porous carbon matrix as a high-performance anode for lithium-ion batteries,” pp. 11381–11387, 2016.
- [22] Q. Xiao *et al.*, “Inward lithium-ion breathing of hierarchically porous silicon anodes,” *Nat. Commun.*, vol. 6, pp. 1–8, 2015.
- [23] T. Ikonen, T. Nissinen, E. Pohjalainen, O. Sorsa, T. Kallio, and V. P. Lehto, “Electrochemically anodized porous silicon: Towards simple and affordable anode material for Li-ion batteries,” *Sci. Rep.*, vol. 7, no. 1, pp. 1–8, 2017.
- [24] F. Dai *et al.*, “Minimized Volume Expansion in Hierarchical Porous Silicon upon Lithiation,” *ACS Appl. Mater. Interfaces*, vol. 11, no. 14, pp. 13257–13263, 2019.
- [25] K. Zhang, Y. Xia, Z. Yang, R. Fu, C. Shen, and Z. Liu, “Structure-preserved 3D porous silicon/reduced graphene oxide materials as anodes for Li-ion batteries,” *RSC Adv.*, vol. 7, no. 39, pp. 24305–24311, 2017.
- [26] H. Wu *et al.*, “Six Thousand Electrochemical Cycles of Double-Walled Silicon Nanotube Anodes for Lithium Ion Batteries,” *Nat. Nanotechnol.*, vol. 7, pp. 310–315, 2012.
- [27] N. Liu *et al.*, “A pomegranate-inspired nanoscale design for large-volume-change lithium battery anodes,” *Nat. Nanotechnol.*, vol. 9, no. 3, pp. 187–192, 2014.
- [28] H. Wu, G. Zheng, N. Liu, T. J. Carney, Y. Yang, and Y. Cui, “Engineering empty space between Si nanoparticles for lithium-ion battery anodes,” *Nano Lett.*, vol. 12, no. 2, pp. 904–909, 2012.
- [29] L. Wei, C. Chen, Z. Hou, and H. Wei, “Poly (acrylic acid sodium) grafted carboxymethyl cellulose as a high performance polymer binder for silicon

- anode in lithium ion batteries,” *Nat. Publ. Gr.*, no. December 2015, pp. 1–8, 2016.
- [30] E. Quiroga-gonzález, J. Carstensen, and H. Föll, “Structural and Electrochemical Investigation during the First Charging Cycles of Silicon Microwire Array Anodes for High Capacity Lithium Ion Batteries,” pp. 626–636, 2013.
- [31] S. Hansen, E. Quiroga-gonzález, J. Carstensen, and H. Föll, “Electrochimica Acta Size-dependent cyclic voltammetry study of silicon microwire anodes for lithium ion batteries,” *Electrochim. Acta*, vol. 217, pp. 283–291, 2016.
- [32] B. Jerliu *et al.*, “Lithium insertion into silicon electrodes studied by cyclic voltammetry and: Operando neutron reflectometry,” *Phys. Chem. Chem. Phys.*, vol. 20, no. 36, pp. 23480–23491, 2018.
- [33] G. Shoorideh *et al.*, “Harvesting Interconductivity and Intraconductivity of Graphene Nanoribbons for a Directly Deposited , High-Rate Silicon-Based Anode for Li-Ion Batteries,” 2018.
- [34] J. Wang *et al.*, “Tuning the Outward to Inward Swelling in Lithiated Silicon Nanotubes via Surface Oxide Coating,” *Nano Lett.*, vol. 16, no. 9, pp. 5815–5822, 2016.
- [35] X. Hua *et al.*, “In situ transmission electron microscopy of electrochemical lithiation , delithiation and deformation of individual graphene nanoribbons,” vol. 0, no. 1, pp. 0–8, 2012.
- [36] X. Fan, W. T. Zheng, and J. Kuo, “Adsorption and Diffusion of Li on Pristine and Defective Graphene,” 2012.

CHAPTER 3

DIRECT DEPOSIT SILICON/GRAPHITE/GRAPHENE HYBRID ANODES FOR SCALABLE AND HIGH PERFORMANCE LITHIUM ION BATTERIES

3.1 Introduction

Presently lithium ion battery technology uses graphite as the anode material which has a theoretical capacity of upto 372 mAh/g and thus a significant upgrade in terms of gravimetric and volumetric energy density is the need of the hour especially for applications such as Electric Vehicle[1][2][3][4]. Silicon anode has been one of the most promising alternatives to the conventional graphite anode due to its high theoretical gravimetric capacity of about 4200mAh/g[5][6][7]. However Silicon undergoes huge volume expansion because of its inherent ability to store a lot of lithium ions which leads to huge stress creation over a number of cycles of lithiation and delithiation. This creation of huge stress leads to pulverization of the electrode material as well as detachment of the active material from the collector resulting in electrical isolation of silicon. Solid electrolyte interphase is typically formed at potentials less than 1V which is a passivating layer but due to the repeated volume

changes the SEI layer is broken down over a number of cycles resulting thicker SEI and higher impedance and also resulting in a lower columbic efficiencies. All these steps occur in a synergistic way and lead to rapid failing of the silicon based anodes. Apart from these issues Silicon has inherently low electrical conductivity which impedes its use in high power density or rate capability applications[8][9][10][11][12][13][14].

To overcome these obstacles various different strategies have been explored. Coatings of various materials such as conductive polymers[15] [16] help to provide a continuous conductive network and self healing polymers [17] which has the ability to recover by itself during repeated cycling. Silicon/Graphene hybrid anodes have been widely used because of the ability of graphene to not only provide excellent conductivity but also act as a mechanical buffer towards the silicon volume expansion and hence improve cycle life performance[18][19][20]. Other approaches, including but not limited to, have utilized silicon carbon based composites and engineering void spaces for the effective accommodation of silicon volume expansion[21][22][23][24][25]. The various approaches studied in the literature to create pore spaces invariably involve the use of an expensive fabrication method such as chemical vapour deposition(CVD) to create an assembly with a sacrificial template that is etched away later by using hydrofluoric acid[26][27][28].

One of the most promising approaches has been to blend silicon with graphite to serve as the anode. Graphite has a number of advantages such as high columbic efficiency, reasonable mechanical flexibility, good electrical conductivity, and low cost[29].

Blending silicon with graphite will result in an increase in ICE, reduced overall volume expansion and thus better cycle retention. Additionally there will not a major change required from a material processing point of view since there is already large scale production in place for the manufacturing of graphite based anodes[30][31]. However the blending of Silicon and graphite only works at extremely low concentrations of silicon. If the silicon content is increased the volume expansion is massive and it leads to the graphite losing electrical contact from the collector due to the electrode pulverization[32][33]. To overcome these issues many groups have turned towards carbon based additives which not only enhance the mixing of silicon in the graphitic structures to give homogenous resulting micrometer sized composites but also to provide sufficient mechanical support to counter silicon's volume expansion[34][35].

In our study we are blending silicon with two different kinds of graphite i.e. spherical graphite, which from here onwards will be referred to as CP11, and plate like graphite, which from now on will be referred to as SF-6, to see the compatibility of silicon with different kinds of graphite which gives us different morphology of the hybrid electrode. We will also be using graphene as an additive to mitigate the volume expansion associated with silicon in order to increase the silicon content in this composite which is aimed at 40%. The process of choice is air-controlled electrospray to achieve the desired morphology in a scalable and economic manner. The respective electrodes containing silicon and CP11, containing silicon SF6 and silicon CP11 and SF6 will be referred to as Si/CP11, Si/SF6 and Si/CP11/SF6 from now on respectively.

3.2 Experimental Section

Preparation of DD Silicon/CP11 Graphite/Graphene anodes via Air-controlled

Electrospray: 2.5g of CMC (MTI) was dissolved in a mixture of 80.833g of Distilled water and left for stirring overnight. 5g of SBR (MTI) originally at 50% solid content was diluted to 15% solid content by adding 28.34g of distilled water left for overnight stirring. 5.32g distilled water was mixed with 2.61g of Isopropyl alcohol and left for stirring at 45°C for 5 minutes. Next 0.515g of CP11 (Hyundai) was added to the solution and left for sonication for 75 minutes with intermediate vortex stirring to dissolve the solution completely. 1.125g of the CMC solution prepared overnight was added into the solution to increase the stability of the solution which decreases after sonication. 0.3g of SBR was added into the solution. Next 0.15g of Silicon (US Research Nanomaterials c.a. 30-70nm) was added in the mixture and left for sonication(X) for 1 hour to disperse the solution properly and prevent any aggregation of silicon nanoparticles. Next another 1.125g of CMC was added into the solution for the same purpose as before i.e. to increase the stability of the solution. Finally 2.833g of Graphene (ACS) solution in water was added into the mixture. The solution was stirred vigorously and left overnight for stirring. The solution was then pumped from a syringe at 0.04ml/min towards a copper collector at a distance of 15cm from the tip of the needle. 25KV of Voltage was applied to the system. Additionally 30psi of air pressure was applied to the system which resulted in the formation of Si/CP11/CMC/SBR/Gr composite which was collected on the copper foil. This resulted in formation of DD Si/CP11/CMC/SBR/Gr electrode on the copper collector

of the loading 0.8-1 mg/cm². Higher areal or mass loading can simply be achieved by longer spraying time or by using additional nozzles.

Preparation of DD Silicon/SF6 Graphite/Graphene anodes via Air-controlled

Electrospray: 2.5g of CMC (MTI) was dissolved in a mixture of 80.833g of Distilled water and left for stirring overnight. 5g of SBR (MTI) originally at 50% solid content was diluted to 15% solid content by adding 28.34g of distilled water left for overnight stirring. 5.32g distilled water was mixed with 2.61g of Isopropyl alcohol and left for stirring at 45°C for 5 minutes. Next 0.515g of SF6 (Hyundai) was added to the solution and left for sonication for 15 minutes with intermediate vortex stirring to dissolve the solution completely. 1.125g of the CMC solution prepared overnight was added into the solution to increase the stability of the solution which decreases after sonication. 0.3g of SBR was added into the solution. Next 0.15g of Silicon (US Research Nanomaterials c.a. 30-70nm) was added in the mixture and left for sonication(X) for 1 hour to disperse the solution properly and prevent any aggregation of silicon nanoparticles. Next another 1.125g of CMC was added into the solution for the same purpose as before i.e. to increase the stability of the solution. Finally 2.833g of Graphene (ACS) solution in water was added into the mixture. The solution was stirred vigorously and left overnight for stirring. The solution was then pumped from a syringe at 0.04ml/min towards a copper collector at a distance of 15cm from the tip of the needle. 25KV of Voltage was applied to the system. Additionally 30psi of air pressure was applied to the system which resulted in the formation of Si/SF6/CMC/SBR/Gr composite which was collected on the copper foil. This resulted

in formation of DD Si/SF6/CMC/SBR/Gr/ electrode on the copper collector of the loading 0.8-1 mg/cm². Higher areal or mass loading can simply be achieved by longer spraying time or by using additional nozzles.

Preparation of DD Silicon/CP11/SF6 Graphite/Graphene anodes via Air-controlled Electrospray: 2.5g of CMC (MTI) was dissolved in a mixture of 80.833g of Distilled water and left for stirring overnight. 5g of SBR (MTI) originally at 50% solid content was diluted to 15% solid content by adding 28.34g of distilled water left for overnight stirring. 5.32g distilled water was mixed with 2.61g of Isopropyl alcohol and left for stirring at 45°C for 5 minutes. Next 0.2575g of CP11 was added to the mixture and stirred vigorously by vortex stirrer. This solution was kept for sonication for 75minutes. Next 0.2575g of SF6 (Hyundai) was added to the solution and left for sonication for 15 minutes with intermediate vortex stirring to dissolve the solution completely. 1.125g of the CMC solution prepared overnight was added into the solution to increase the stability of the solution which decreases after sonication. 0.3g of SBR was added into the solution. Next 0.15g of Silicon (US Research Nanomaterials c.a. 30-70nm) was added in the mixture and left for sonication(X) for 1 hour to disperse the solution properly and prevent any aggregation of silicon nanoparticles. Next another 1.125g of CMC was added into the solution for the same purpose as before i.e. to increase the stability of the solution. Finally 2.833g of Graphene (ACS) solution in water was added into the mixture. The solution was stirred vigorously and left overnight for stirring. The solution was then pumped from a syringe at 0.04ml/min towards a copper collector at a distance of 15cm from the tip

of the needle. 25KV of Voltage was applied to the system. Additionally 30psi of air pressure was applied to the system which resulted in the formation of Si/CP11/SF6/CMC/SBR/Gr composite which was collected on the copper foil. This resulted in formation of DD Si/CP11/SF6/CMC/SBR/Gr electrode on the copper collector of the loading 0.8-1 mg/cm². Higher areal or mass loading can simply be achieved by longer spraying time or by using additional nozzles.

Material Characterization of the Directly Deposited Electrodes. Composite electrodes were characterized using a scanning electron microscope (SEM, Zeiss Gemini) and Energy Dispersive Spectroscopy (Bruker) to assess morphological changes. Thermogravimetric analysis (TGA, TA instruments Q500) was conducted on the electrodes to measure the silicon content.

Battery fabrication and electrochemical measurements of the directly deposited silicon electrodes. 2032 type coin cells were fabricated using the as directly deposited silicon composite as working electrode, Lithium metal disc (MTI) as counter electrode and a polyethylene separator (Cellgard) to test the performance of the half cells. A homemade electrolyte 1M LiPF₆ as the salt with dimethyl carbonate (Sigma), Ethylene methyl carbonate (Sigma), and diethyl carbonate (Sigma) was used as solvents in a ratio of 2:4:4 with 10% of fluoroethylene carbonate (Sigma) additive inside the half cells. Electrochemical properties of the cells were characterized by electrochemical impedance spectroscopy (PARASAT 4000, Princeton Applied

Research) and cyclic voltammetry (CH Instruments, Potentiostat) and galvanostatic charge and discharge cycles (MTI). A voltage window of 0.01-1.5V Vs Li/Li⁺ were applied to the half cells.

3.3 Results and Discussion

Material Characterization:

Morphology of CP11 and SF6 is shown in figure 3.1a) and b) respectively. It can be seen that CP11 is sphere-like and SF6 is plate like. Figure 3.2 shows top view and cross sections of Si/CP11/CMC/SBR/Gr anode. It can be shown that the CP11/ Si electrode is very well packed but at high magnification it can be observed that not a lot of Silicon is available on its surface. Figure 3.3 shows top view and cross section images of SF6/Si electrode. It is apparent that the packing is not very compact and the electrode appears bulky. However at high magnification a homogeneous distribution of Si on the surface of the graphite flake is observed which suggests the small dimension of the graphite flake is able to provide electrical contact to activate the silicon and it has some sharp features. Figure 3.4 shows the top view and cross section view of the electrode combining both the kinds of graphite namely CP11 and SF6. It can be observed that the resulting morphology is a transition between bulky and most compact.

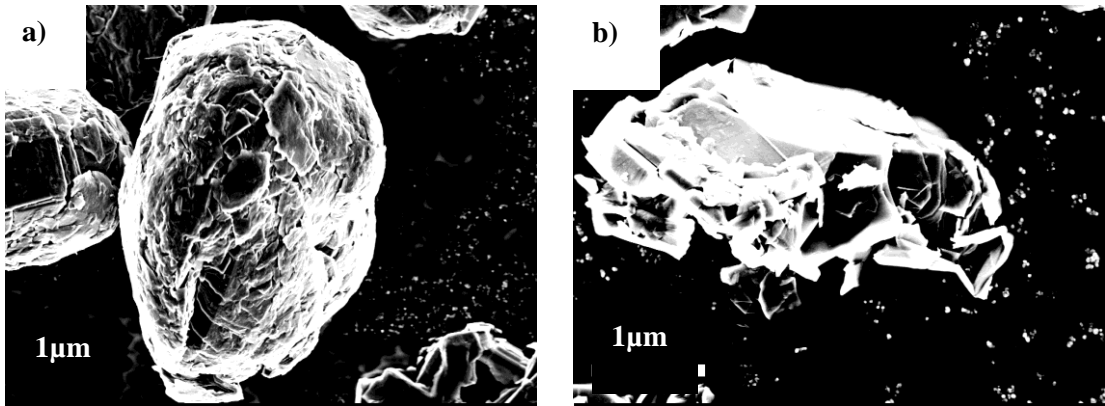


Figure 3.1 SEM images of a) CP11 and b) SF6

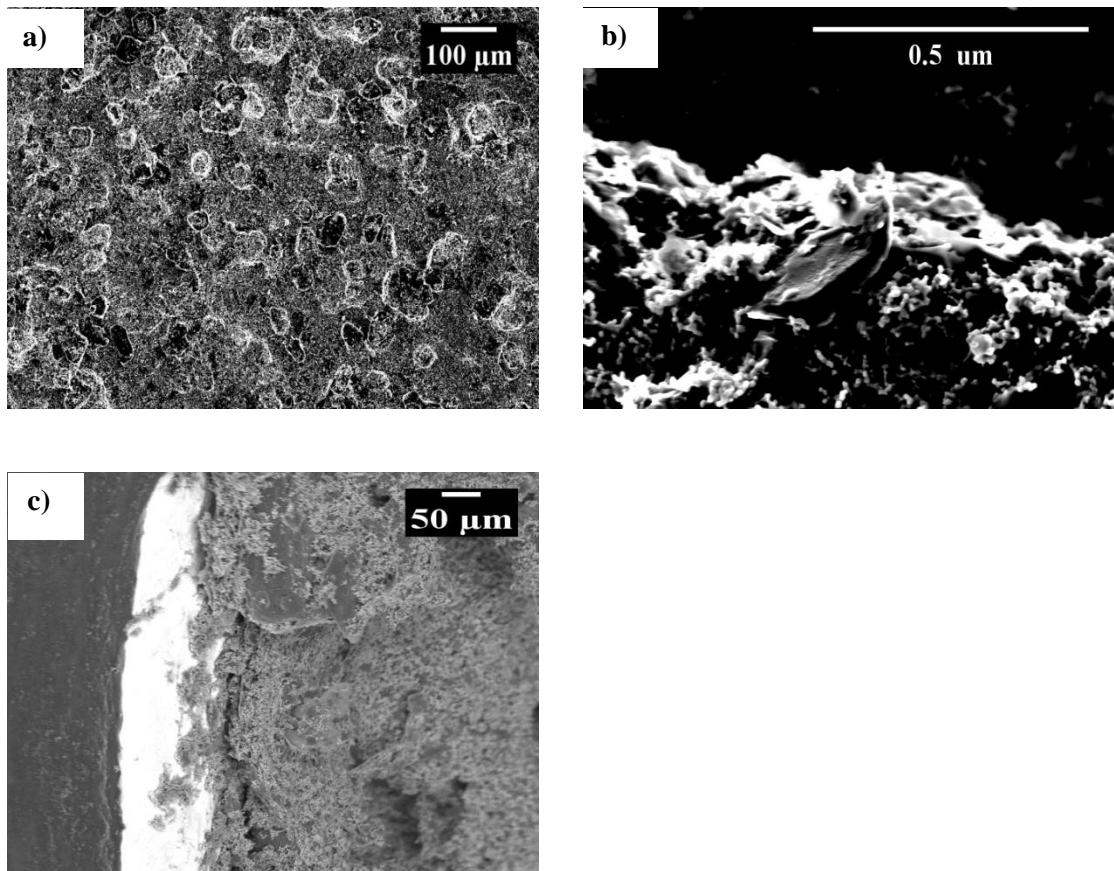


Figure 3.2 SEM images of a) low magnification top view Si/CP11 electrode b) high magnification top view of Si/CP11 electrode c) cross-section Si/CP11 electrode

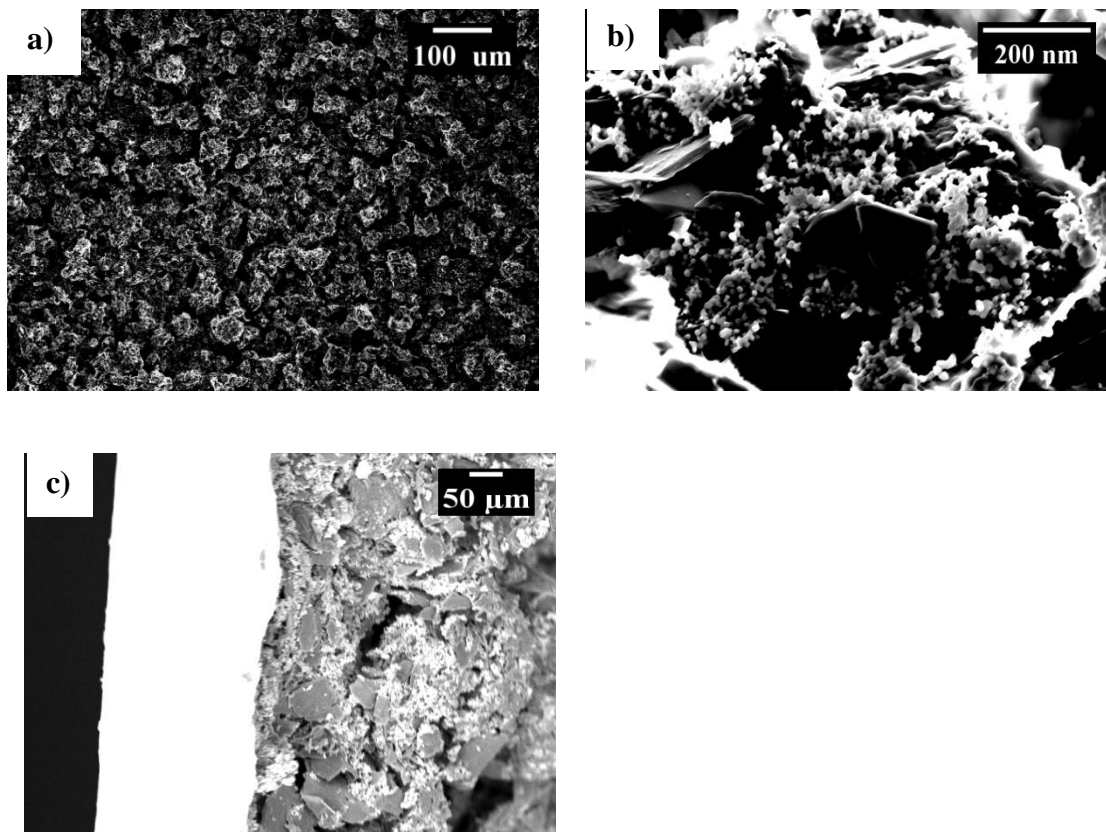


Figure 3.3 SEM images of a) low magnification top view Si/SF6 electrode b) high magnification top view of Si/SF6 electrode c) cross-section Si/SF6 electrode

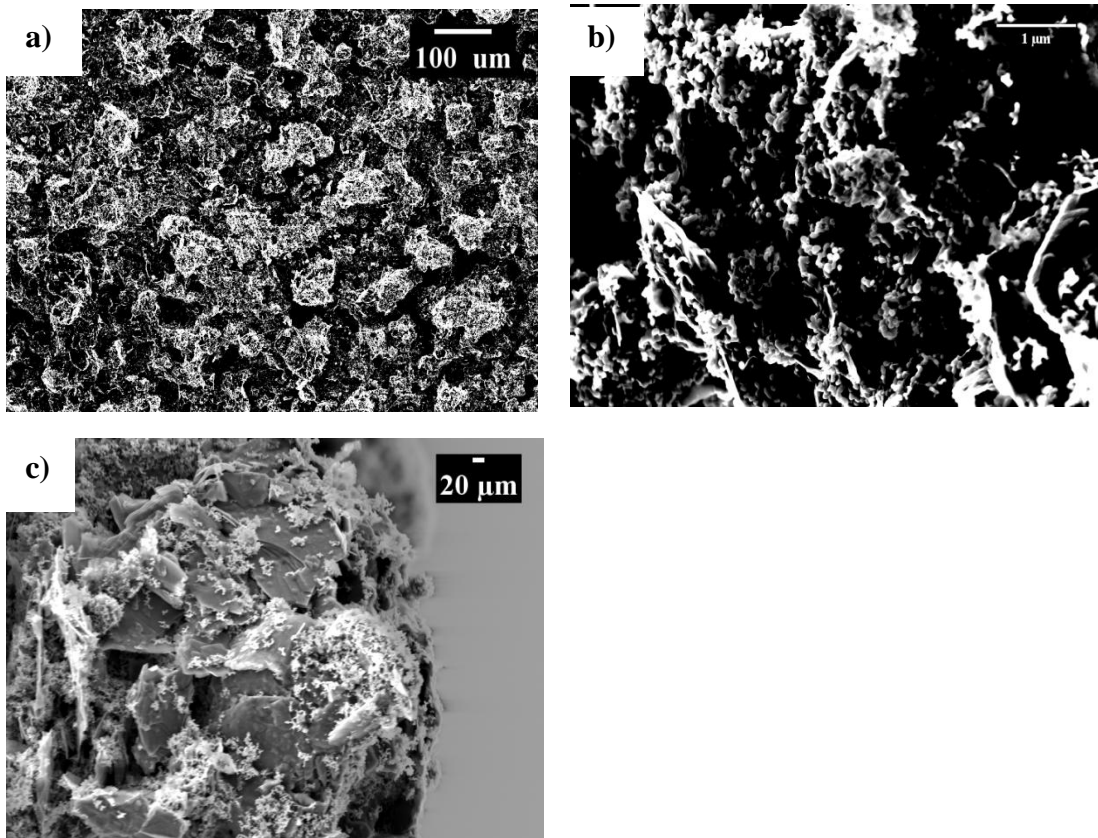


Figure 3.4 SEM images of a) low magnification top view Si/CP11/SF6 electrode b) high magnification top view of Si/CP11/SF6 electrode c) cross-section Si/CP11/SF6 electrode

Fig 3.5 shows the comparison of TGA analysis for the Si/SF6, Si/CP11 as well as Si/CP11/SF6 which shows that all 3 have exactly similar composition including similar silicon content and hence we can compare the electrochemical performances of these 3 cases and rule out the influence of composition.

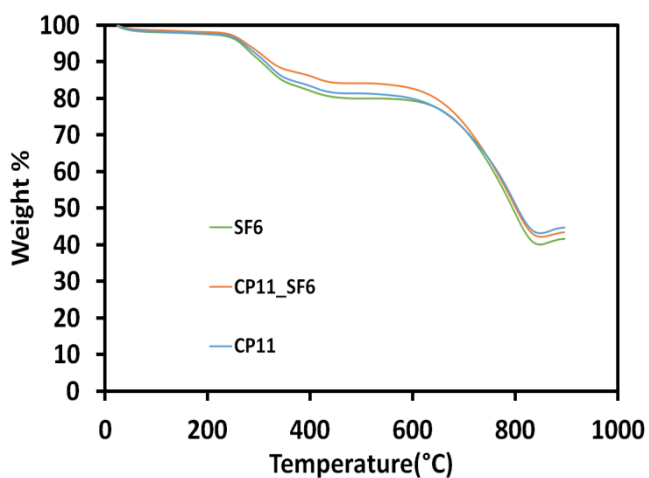


Figure 3.5 TGA analysis of Si/CP11, Si/SF6, and Si/CP11/SF6

Figure 3.7 shows the tap density comparison between CP11 and SF6. It is quite clear that CP11 has a lot higher tap density than SF6 which verifies our previous findings of CP11 being a lot more efficiently packed compared to SF6.

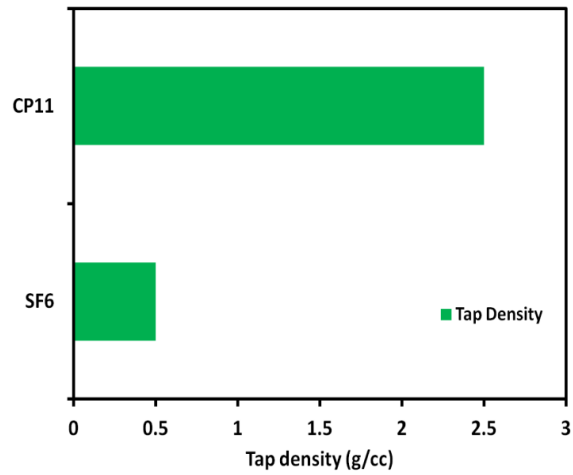


Figure 3.6 Tap density of CP11 and SF6 powder

Half cell Electrochemical Performance:

To compare the electrochemical performance 2032 coin type half cells were assembled. Each cell was lithiated to a voltage of 1.5V and delithiated to a voltage of 0.01V and made to undergo 5 formation cycles at 0.1C and then undergo deep charge discharge galvanostatic cycling with the 1st cycle at 0.1C, second cycle at 0.2C and the rest of the cycles at 0.3C and going back to 0.1C after 50 cycles at 0.3C to see the rate of recovery and same pattern was followed thereafter.

Figure 3.7 shows the capacity-voltage graph for the initial formation cycle of Si/CP11, Si/SF6 and Si/CP11/SF6. All 3 cases show a very similar profile with a small plateau at 0.8V signifying the formation of SEI and then a larger plateau around 0.25V which signifies the lithium insertion reactions with silicon[36]. The 1st cycle delithiation capacity for Si/SF6 is 800mAh/g while that for Si/CP11 is 686 mAh/g and for Si/CP1/SF6 is 745mAh/g. One of the possible reasons for the higher conductivity of the plate like graphite is the smaller size of the plate like graphite which allows it to have multiple contact points with silicon thus providing better electrical contact with silicon. In case of CP11 because of its larger size it is unable to fit in between two different silicon particles and thus electrically isolate the silicon by not providing efficient electrical contact. Expectedly blending both the graphite together gives an intermediate capacity. Figure 3.8 illustrates the reason for higher capacity for Si/SF6 case. The first cycle columbic efficiency for Si/SF6, Si/CP11 and Si/CP11/SF6 is

80.2, 84.54 and 83.42 respectively. The highest columbic efficiency for Si/CP11 is possibly comes from the lower surface area of CP11 due to its larger size. Similarly due to the larger surface area of SF6 there is more possibility of side reactions occurring and hence the Si/SF6 has the lowest ICE whereas Si/CP11/SF6 gives an intermediate ICE which follows a similar trend as seen earlier in figure 3.8.

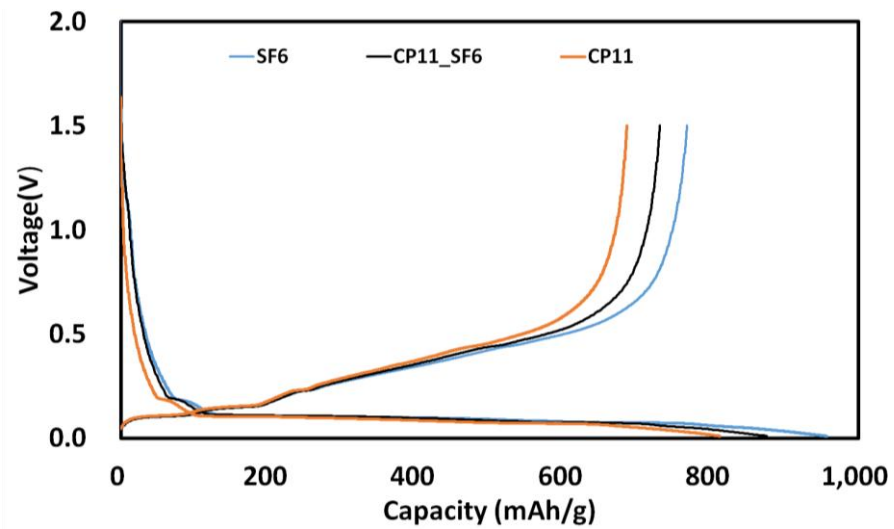


Figure 3.7 initial capacity-voltage profiles of Si/SF6, Si/CP11 and Si/CP11/SF6

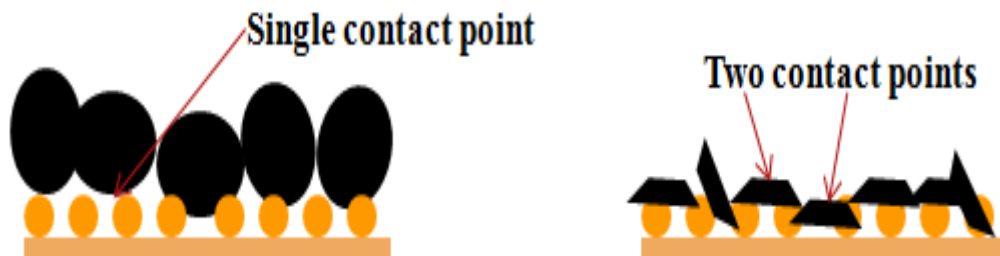


Figure 3.8 schematic illustrating higher capacity for Si/SF6 electrode

The cycle life performance of Si/SF6, Si/CP11 and Si/CP11/SF6 is represented by figure 3.9. All the three show relatively stable cycling at 0.3C. After 200 cycles the capacity at 0.1C for Si/CP11/SF6 and Si/SF6 is almost the same whereas Si/CP11 is the least because of its lower starting capacity. Figure 3.10 shows the electrochemical impedance profile for Si/CP11, Si/SF6 and Si/CP11/SF6. Interestingly the overall charge transfer resistance is the least for Si/CP11/SF6 at 90 Ω whereas for Si/SF6 it is 120 Ω and for Si/CP11 it is 100 Ω . One possibility for the charge transfer resistance being the highest for Si/SF6 is its less efficient packing due to the lower tap density as highlighted in figure 3.1 and 3.6 whereas Si/CP11 has better packing. Si/CP11/SF6 has the least resistance possibly because of the synergistic effects of mixing the spherical and plate like graphite during the air-controlled electrospraying. Figure 3.11 shows the rate capability of Si/CP11, Si/SF6 and Si/CP11/SF6 respectively. It is evident from the figure that at lower C rates Si/SF6 gives the highest capacity due to its more efficient activation of silicon but at higher C rates it performs very badly whereas Si/CP11 gives a better performance at higher C rates due to its more efficient packing. The Si/CP11/SF6 gives the best performance at higher C rates highlighting the synergistic effect of blending the two kinds of graphite as also seen in the EIS plot in figure 3.10. The higher capacity compared to Si/CP11 is due to the presence of SF6 and the better rate capability performance is due to the presence of CP11 and thus it gives the most optimized performance highlighting the advantages of blending the two kinds of graphite together with silicon to give us the best of both worlds.

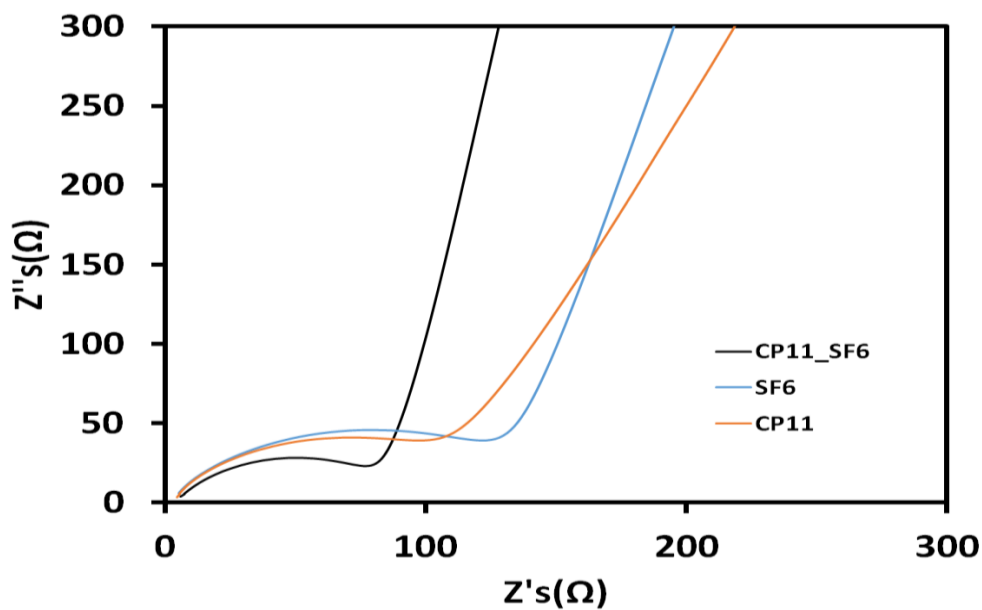


Figure 3.9 Nyquist plots for impedance data for Si/CP11, Si/SF6 and Si/CP11/SF6

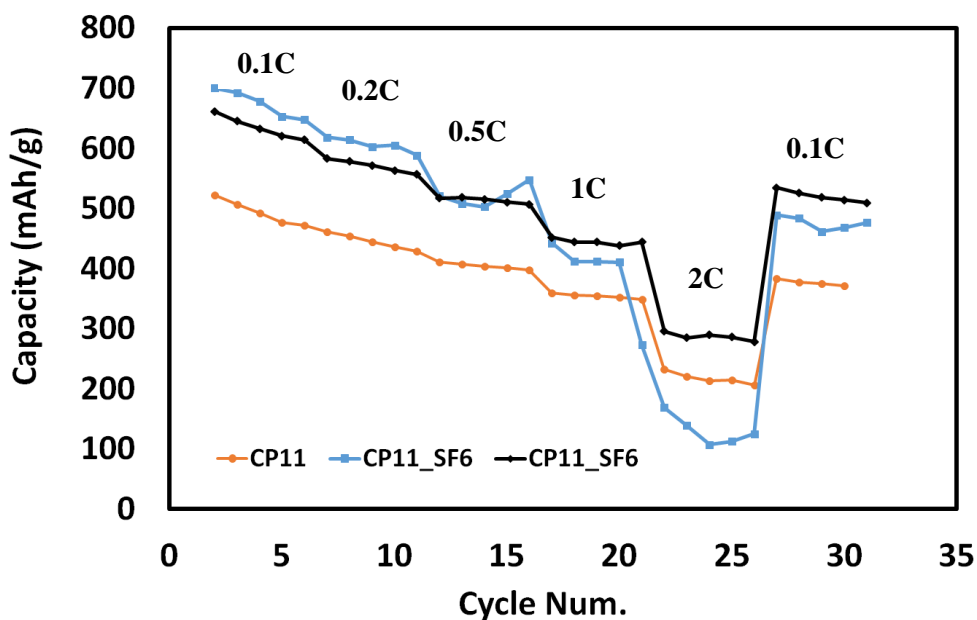


Figure 3.10 Rate capability of Si/CP11, Si/SF6, Si/CP11/SF6

3.4 Conclusion:

In summary, we have successfully synthesized a moderately higher silicon content silicon/graphite/ graphene composite system by air –controlled electrospray which is of practical relevance. By blending silicon with graphite we are able to show increased initial columbic efficiency and no compromise has been made to the specific capacity by increasing the amount of silicon because of the presence of graphene as an additive which reduces severe volume expansion resulting from a Si/Graphite based system. We show the compatibility of blending different types of graphite with silicon namely CP11 which is spherical like and SF6 which is plate like. While Si/SF6 gives us a higher capacity due to higher silicon utilization because of its smaller size Si/CP11 gives us better rate capability and lower impedance because of its more efficient packing facilitated by its higher tap density. Si/CP11 gives us higher initial columbic efficiency compared to Si/SF6 because of the higher surface area of SF6 due to its smaller size. It is found by combining both plate-like and spherical-like graphite with silicon we achieve the best of both worlds in terms of best rate capability and the least charge transfer resistance because of the synergistic effects as well as we get an intermediate ICE and capacity thus arriving at an optimized silicon graphite graphene composite system for a moderate silicon content system.

REFERENCES

- [1] M. Armand and J. Tarascon, "Building better batteries," vol. 451, no. February, pp. 2–7, 2008.
- [2] B. Dunn, H. Kamath, and J. Tarascon, "for the Grid : A Battery of Choices," vol. 334, no. November, pp. 928–936, 2011.
- [3] P. G. Bruce, B. Scrosati, and J. Tarascon, "Lithium Batteries Nanomaterials for Rechargeable Lithium Batteries ** Angewandte," pp. 2930–2946, 2008.
- [4] M. Li, J. Lu, Z. Chen, and K. Amine, "30 Years of Lithium-Ion Batteries," vol. 1800561, pp. 1–24, 2018.
- [5] E. Environ, J. R. Szczech, and S. Jin, "Energy & Environmental Science Nanostructured silicon for high capacity lithium battery anodes †," pp. 56–72, 2011.
- [6] N. S. Hochgatterer *et al.*, "Silicon / Graphite Composite Electrodes for High-Capacity Anodes : Influence of Binder Chemistry on Cycling Stability," pp. 76–80, 2008.
- [7] J. P. Maranchi, A. F. Hepp, and P. N. Kumta, "High Capacity , Reversible Silicon Thin-Film Anodes for Lithium-Ion Batteries," pp. 198–201, 2016.
- [8] X. Zuo, J. Zhu, P. Müller-buschbaum, and Y. Cheng, "Nano Energy Silicon based lithium-ion battery anodes : A chronicle perspective review," *Nano Energy*, vol. 31, no. November 2016, pp. 113–143, 2017.
- [9] L. Y. Beaulieu, K. W. Eberman, R. L. Turner, and L. J. Krause, "Colossal Reversible Volume Changes in Lithium Alloys," vol. C, pp. 7–10, 2001.
- [10] J. H. Ryu, J. W. Kim, Y. Sung, and S. M. Oh, "Failure Modes of Silicon Powder Negative Electrode in Lithium Secondary Batteries," pp. 306–309, 2004.
- [11] H. Wu and Y. Cui, "Designing nanostructured Si anodes for high energy," pp. 414–429, 2012.
- [12] J. M. Chem *et al.*, "The failure mechanism of nano-sized Si-based negative electrodes for lithium ion batteries," no. Cmc, pp. 6201–6208, 2011.
- [13] M. Ashuri and L. L. Shaw, "batteries : where size , geometry and structure," pp. 74–103, 2016.
- [14] C. K. Chan *et al.*, "High-performance lithium battery anodes using silicon nanowires," pp. 31–35, 2007.

- [15] H. Wu *et al.*, “conformally coat silicon nanoparticles,” *Nat. Commun.*, vol. 4, pp. 1943–1946, 2013.
- [16] E. Environ, “Environmental Science Improving the cycling stability of silicon nanowire anodes with conducting polymer coatings †,” pp. 7927–7930, 2012.
- [17] C. Wang, H. Wu, Z. Chen, M. T. Mcdowell, Y. Cui, and Z. Bao, “operation of silicon microparticle anodes for,” *Nat. Chem.*, vol. 5, no. 12, pp. 1042–1048, 2013.
- [18] H. Xiang *et al.*, “Graphene / nanosized silicon composites for lithium battery anodes with improved cycling stability,” vol. c, pp. 0–9, 2011.
- [19] J. Ren, Q. Wu, G. Hong, W. Zhang, and H. Wu, “Silicon – Graphene Composite Anodes for High-Energy Lithium Batteries,” vol. 60439, pp. 77–84, 2013.
- [20] S. Chen, M. L. Gordin, R. Yi, G. Howlett, H. Sohn, and D. Wang, “Silicon core-hollow carbon shell nanocomposites with tunable buffer voids for high capacity anodes of lithium-ion batteries,” *Phys. Chem. Chem. Phys.*, vol. 14, no. 37, pp. 12741–12745, 2012.
- [21] L. Wu, J. Yang, X. Zhou, M. Zhang, Y. Ren, and Y. Nie, “Silicon nanoparticles embedded in a porous carbon matrix as a high-performance anode for lithium-ion batteries,” pp. 11381–11387, 2016.
- [22] Q. Xiao *et al.*, “Inward lithium-ion breathing of hierarchically porous silicon anodes,” *Nat. Commun.*, vol. 6, pp. 1–8, 2015.
- [23] T. Ikonen, T. Nissinen, E. Pohjalainen, O. Sorsa, T. Kallio, and V. P. Lehto, “Electrochemically anodized porous silicon: Towards simple and affordable anode material for Li-ion batteries,” *Sci. Rep.*, vol. 7, no. 1, pp. 1–8, 2017.
- [24] F. Dai *et al.*, “Minimized Volume Expansion in Hierarchical Porous Silicon upon Lithiation,” *ACS Appl. Mater. Interfaces*, vol. 11, no. 14, pp. 13257–13263, 2019.
- [25] K. Zhang, Y. Xia, Z. Yang, R. Fu, C. Shen, and Z. Liu, “Structure-preserved 3D porous silicon/reduced graphene oxide materials as anodes for Li-ion batteries,” *RSC Adv.*, vol. 7, no. 39, pp. 24305–24311, 2017.
- [26] H. Wu *et al.*, “Six Thousand Electrochemical Cycles of Double-Walled Silicon Nanotube Anodes for Lithium Ion Batteries,” *Nat. Nanotechnol.*, vol. 7, pp. 310–315, 2012.
- [27] N. Liu *et al.*, “A pomegranate-inspired nanoscale design for large-volume-change lithium battery anodes,” *Nat. Nanotechnol.*, vol. 9, no. 3, pp. 187–192, 2014.
- [28] H. Wu, G. Zheng, N. Liu, T. J. Carney, Y. Yang, and Y. Cui, “Engineering empty space between Si nanoparticles for lithium-ion battery anodes,” *Nano Lett.*, vol. 12, no. 2, pp. 904–909, 2012.
- [29] S. Chae, S. Choi, N. Kim, J. Sung, and J. Cho, “Integration of Graphite and Silicon Anodes for the Commercialization of High-Energy Lithium-Ion

Batteries Angewandte Reviews,” pp. 2–28.

- [30] J. Wu, “The critical role of carbon in marrying silicon and graphite anodes for high - energy lithium - ion batteries,” no. August, pp. 1–20, 2019.
- [31] J. Park, J. Ham, M. Shin, H. Park, Y. Lee, and S. Lee, “Synthesis and electrochemical characterization of anode material with titanium e silicon alloy solid core / nanoporous silicon shell structures for lithium rechargeable batteries,” *J. Power Sources*, vol. 299, pp. 537–543, 2015.
- [32] S. Son *et al.*, “Interfacially Induced Cascading Failure in Graphite-Silicon Composite Anodes,” vol. 1801007, pp. 1–8, 2019.
- [33] M. Wetjen, S. Solchenbach, H. A. Gasteiger, D. Pritzl, J. Hou, and V. Tileli, “Morphological Changes of Silicon Nanoparticles and the Influence of Cutoff Potentials in Silicon-Graphite Electrodes,” vol. 165, no. 7, pp. 1503–1514, 2018.
- [34] H. Wang, J. Xie, S. Zhang, G. Cao, and X. Zhao, “RSC Advances battery anode materials †,” vol. c, pp. 69882–69888, 2016.
- [35] Q. Xu, J. Sun, J. Li, Y. Yin, and Y. Guo, “Scalable synthesis of spherical Si / C granules with 3D conducting networks as ultrahigh loading anodes in lithium-ion batteries,” *Energy Storage Mater.*, vol. 12, no. November 2017, pp. 54–60, 2018.
- [36] J. Oh, D. Jin, K. Kim, D. Song, Y. M. Lee, and M. H. Ryou, “Improving the Cycling Performance of Lithium-Ion Battery Si/Graphite Anodes Using a Soluble Polyimide Binder,” *ACS Omega*, vol. 2, no. 11, pp. 8438–8444, 2017.

CHAPTER 4

PARTICLE COMPOSITE SILICON/GRAPHITE/GRAPHENE HYBRID ANODES FOR SCALABLE AND HIGH PERFORMANCE LITHIUM ION BATTERIES

4.1 Introduction

Since the invention of Lithium ion battery in the early 1990's there has been a lot of research on the type of cathode material but graphite as the anode has been a constant which has a theoretical capacity of upto 372 mAh/g and thus a significant upgrade in terms of gravimetric and volumetric energy density is the need of the hour especially for applications such as Electric Vehicle[1][2][3][4]. Silicon anode has been one of the most promising alternatives to the conventional graphite anode due to its high theoretical gravimetric capacity of about 4200mAh/g[5][6][7]. However Silicon undergoes huge volume expansion because of its inherent ability to store a lot of lithium ions which leads to huge stress creation over a number of cycles of lithiation and delithiation. This creation of huge stress leads to pulverization of the electrode material as well as detachment of the active material from the collector resulting in electrical isolation of silicon. Solid electrolyte interphase is typically formed at

potentials less than 1V which is a passivating layer but due to the repeated volume changes the SEI layer is broken down over a number of cycles resulting thicker SEI and higher impedance and also resulting in a lower columbic efficiencies. All these steps occur in a synergistic way and lead to rapid failing of the silicon based anodes. Apart from these issues Silicon has inherently low electrical conductivity which impedes its use in high power density or rate capability applications[8][9][10][11][12][13][14].

To overcome these obstacles various different strategies have been explored. Coatings of various materials such as conductive polymers[15] [16] help to provide a continuous conductive network and self healing polymers [17] which has the ability to recover by itself during repeated cycling. Silicon/Graphene hybrid anodes have been widely used because of the ability of graphene to not only provide excellent conductivity but also act as a mechanical buffer towards the silicon volume expansion and hence improve cycle life performance[18][19][20]. Other approaches, including but not limited to, have utilized silicon carbon based composites and engineering void spaces for the effective accommodation of silicon volume expansion[21][22][23][24][25]. The various approaches studied in the literature to create pore spaces invariably involve the use of an expensive fabrication method such as chemical vapour deposition(CVD) to create an assembly with a sacrificial template that is etched away later by using hydrofluoric acid[26][27][28].

One of the most promising approaches has been to blend silicon with graphite to serve as the anode. Graphite has a number of advantages such as high columbic efficiency,

reasonable mechanical flexibility, good electrical conductivity, and low cost[29]. Blending silicon with graphite will result in an increase in ICE, reduced overall volume expansion and thus better cycle retention. Additionally there will not a major change required from a material processing point of view since there is already large scale production in place for the manufacturing of graphite based anodes[30][31]. However the blending of Silicon and graphite only works at extremely low concentrations of silicon. If the silicon content is increased the volume expansion is massive and it leads to the graphite losing electrical contact from the collector due to the electrode pulverization[32][33]. To overcome these issues many groups have turned towards carbon based additives which not only enhance the mixing of silicon in the graphitic structures to give homogenous resulting micrometer sized composites but also to provide sufficient mechanical support to counter silicon's volume expansion[34][35].

One of the biggest issues with a silicon graphite carbon hybrid system is the amount of volume expansion that takes place which completely pulverizes the electrode structure resulting in a capacity lower than even 100% graphite based anodes. Figure 4.1 shows the effect of silicon content in a silicon graphite graphene hybrid system. As is evident even at very low silicon content like 10% there is still massive capacity fading. Figure 4.2 is a schematic illustrating the problem associated with decreasing the silicon content. Decreasing the silicon content does not really solve the problem of immense thickness change resulting from the volume expansion of silicon and hence improves cycling only marginally unless the silicon content is reduced to 5-8%[36].

Therefore we need to develop a method to reduce this thickness change due to the volume expansion of silicon. This study aims to combine the lessons learned in chapter 2 and 3 and extend the work further. All our previous work was based on synthesizing direct deposit silicon based anodes. Here we introduce a unique assembly of two step particle additive composite approach to reduce the volume expansion of silicon. Figure 4.3 is a schematic illustrating the first step of the process. A solution of silicon, graphene and polyimide (PI) binder was sprayed onto a collector. After this the as sprayed particles were scratched off the collector and grinded. These particles are then kept under 350°C for 6hours under inert conditions. Finally these particles are blended with CP11 and SF6 in an aqueous solution and sprayed directly onto the copper discs as shown in figure 4.4 constituting the second step of this process. This allows us to get particles which will retain its structure even in an aqueous solution because of the particles being insoluble in water. To highlight the advantages of this two step additive composite approach we also make control direct deposit electrodes having the same composition but very different assembly. We also show a very high level of flexibility in our material processing by forming particles of different size and morphology by changing electro spraying parameters and study the effect of the same on electrochemical performance.

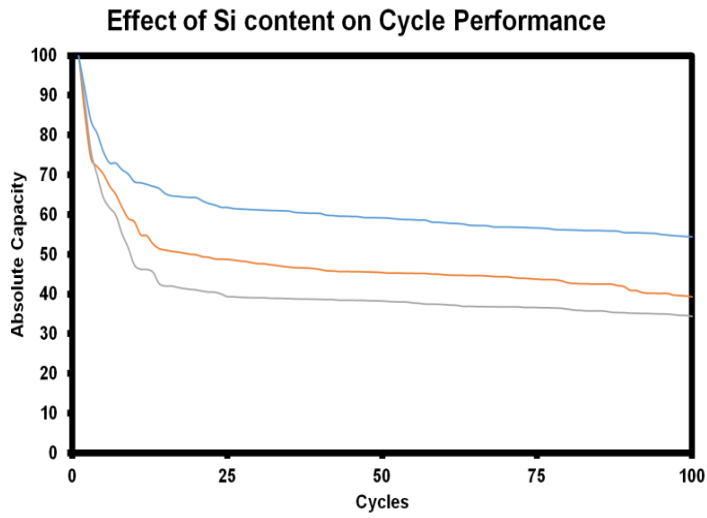


Figure 4.1 Effect of lowering silicon content on cycle performance

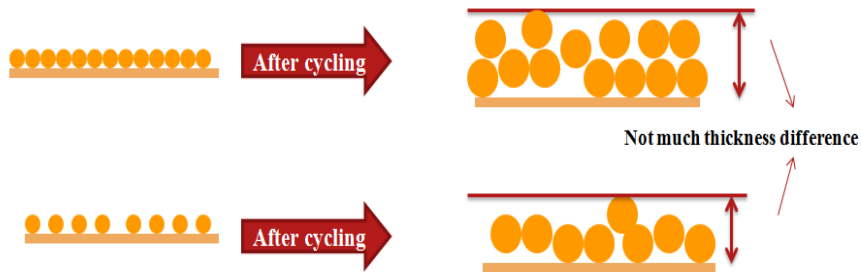


Figure 4.2 Schematic illustrating the problem of silicon thickness change

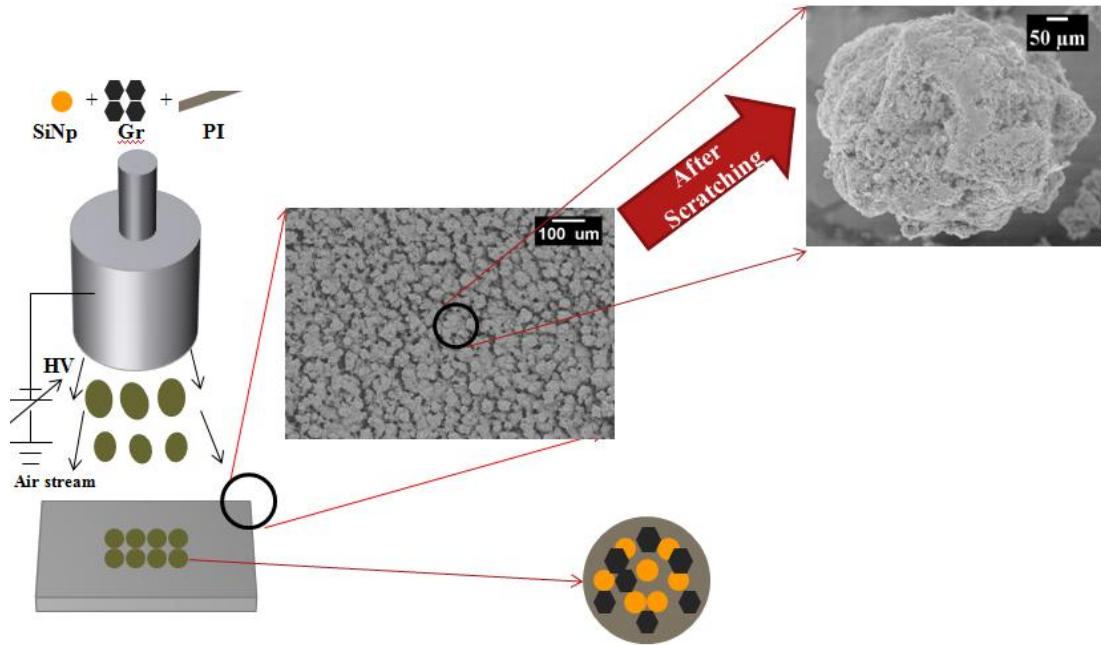


Figure 4.3 Schematic illustrating the first step of the particle additive composite

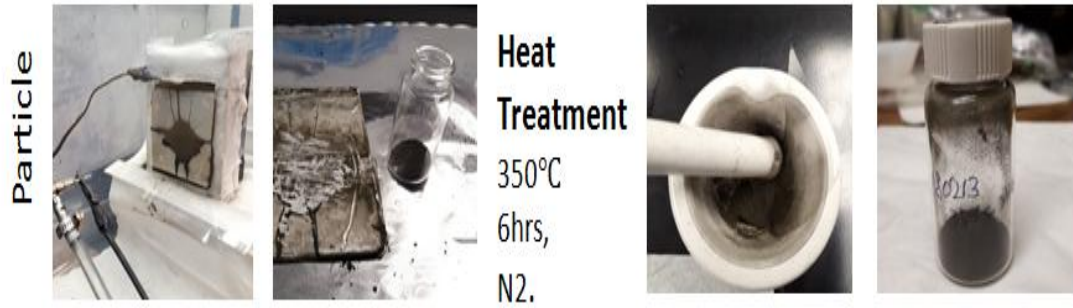


Figure 4.4 A visual representation of the synthesis of the particles

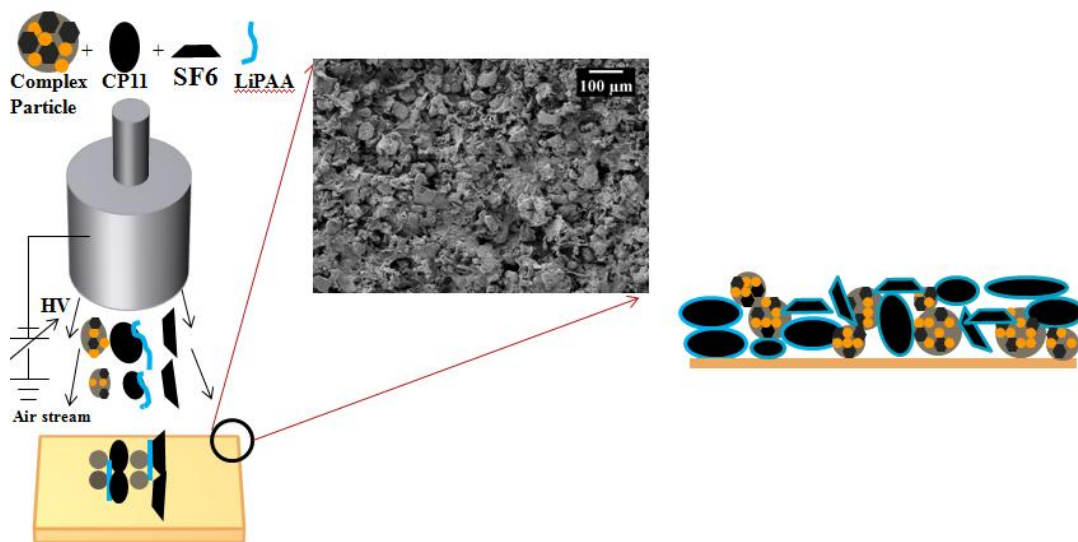


Figure 4.5 Schematic illustrating the second step of the particle additive composite

4.2. Experimental Section

Preparation of Particle Composite Si/Graphite/Graphene hybrid anodes via Air-controlled Electropray: 1.5g of PI (X) was dissolved in a mixture of 7.5g of NMP (Sigma Aldrich) and 7.5g of DMF (Sigma Aldrich) and left for stirring overnight.

0.35g of Silicon (US Research Nanomaterials c.a. 30-70nm) was dissolved in a mixture of 0.91g of NMP and 3.43g of DMF and left for sonication(X) for 1 hour to disperse the solution properly and prevent any aggregation. 1.167g of PI solution prepared previously was then added to this solution. The solution was stirred vigorously by a vortex stirrer. Finally, 2.971g of a 4% by weight solution of Graphene in NMP (ACS) was added to the mixture. The solution was stirred vigorously and left overnight for stirring. The solution was then pumped from a syringe at 0.01ml/min towards a copper collector at a distance of 20cm from the tip of the needle. 25KV of Voltage was applied to the system. Additionally 30psi of air pressure was applied to the system. The solution was sprayed overnight for 8hours. This resulted in the formation of Si/Gr/PI composite which was collected on the Aluminium foil. The as collected spray was scratched off the surface of the Aluminium collector and sphere-like particles were obtained containing Si/PI/Gr. As-collected particles were then heat treated at 350°C at a ramp rate of 10°C/min for 6h in N₂ inert conditions. These particles are then grinded on a mortar and pestle to reduce the particle size and break up any aggregates that may have been formed.

0.92g of PAA(Sigma) was mixed with 91.08g of distilled water and stirred for 30 minutes. Another separate solution of 0.24g of Lithium hydroxide and 23.76g of distilled water was prepared. The LiOH solution was added dropwise to the PAA solution to form Lithiated polyacrylic acid(LiPAA). This was left for stirring overnight.

Then a separate solution was formed to execute the second step of this process. 9.03g of distilled water was taken and into it 0.2575g of CP11 was added and the resulting

solution was left for sonication for 90minutes along with regular vortex stirring. Then 0.2575g of SF6 was added to the solution and again the solution is sonicated for 15 minutes. 0.6g of the LiPAA solution previously prepared was added into this solution. 0.064g of the as prepared comoposite particles were added into this solution. Finally, 0.064g of Graphene(ACS) powder was added into the solution. This is the solution for the second part of the process. This solution was electro sprayed directly onto to the copper collector which resulted in formation of DD Si/PI/Gr/CP11/SF6/LiPAA electrode on the copper collector of the loading $1.8\text{mg}/\text{cm}^2$. Higher areal or mass loading can simply be achieved by longer spraying time or by using additional nozzles.

Preparation of DD Silicon/Graphite/Graphene hybrid anodes via Air-controlled

Electrospray: 6.72g of distilled water was taken and into it 0.23g of CP11 was added and the resulting solution was left for sonication for 90minutes along with regular vortex stirring. Then 0.23g of SF6 was added to the solution and again the solution is sonicated for 15 minutes. 1.905g of the LiPAA solution previously prepared was added into this solution. 0.1g of SiNp were added into this solution. Finally, 0.56g of Graphene(ACS) solution was added into the solution. This is the solution for the reference direct deposit method. This solution was electro sprayed directly onto to the copper collector which resulted in formation of DD Si/Gr/CP11/SF6/LiPAA electrode on the copper collector of the loading $1.8\text{mg}/\text{cm}^2$. Higher areal or mass loading can simply be achieved by longer spraying time or by using additional nozzles.

Material Characterization of the Directly Deposited Electrodes. Composite electrodes were characterized using a scanning electron microscope (SEM, Zeiss Gemini) and Energy Dispersive Spectroscopy (Bruker) to assess morphological changes. Thermogravimetric analysis (TGA, TA instruments Q500) was conducted on the electrodes to measure the silicon content.

Battery fabrication and electrochemical measurements of the directly deposited silicon electrodes. 2032 type coin cells were fabricated using the as directly deposited silicon composite as working electrode, Lithium metal disc (MTI) as counter electrode and a polyethylene separator (Cellgard) to test the performance of the half cells. A homemade electrolyte 1M LiPF_6 as the salt with dimethyl carbonate (Sigma), Ethylene methyl carbonate (Sigma), and diethyl carbonate (Sigma) was used as solvents in a ratio of 2:4:4 with 10% of fluoroethylene carbonate (Sigma) additive inside the half cells. Electrochemical properties of the cells were characterized by electrochemical impedance spectroscopy (PARASAT 4000, Princeton Applied Research) and cyclic voltammetry (CH Instruments, Potentiostat) and galvanostatic charge and discharge cycles (MTI). A voltage window of 0.01-1.5V Vs Li/Li^+ were applied to the half cells.

4.3 Results and Discussion:

Material Characterization:

Figure 4.6 shows the SEM images of the particles on the collector before scratching it off and after scratching it off the collector. Figure 4.6a) shows that the particles are very easy to scratch off the collector and we can observe a uniform deposition on the collector. Figure 4.6 b) shows that the particle has a spherical like structure and looks reasonably compact Figure 4.7 a) shows the morphology of the electrode made from the two step particle composite approach and b) shows the morphology of the control electrode having the same composition but very different structure. We can see the particle composite structure has an inherent roughness associated to it while the reference has a relatively smoother surface.

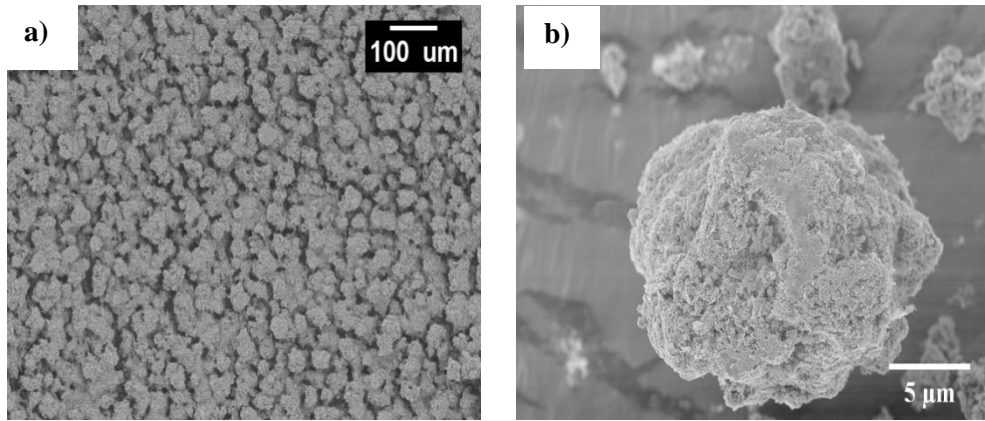


Figure 4.6 SEM images of a) particles on the collector b) Particle after scratching

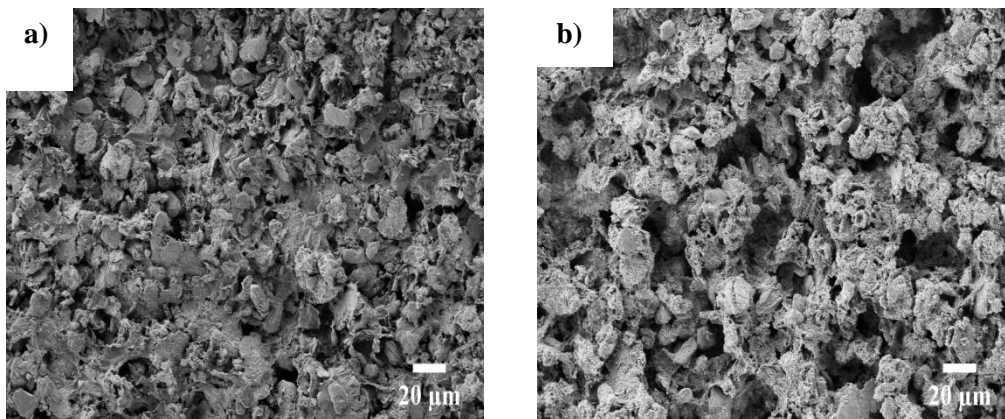


Figure 4.7 SEM images of a) particle additive composite electrode b) direct deposit electrode

Figure 4.8 shows the thermogravimetric analysis for particle additive composite and reference i.e. direct deposit electrodes which shows that the composition for both is very similar and hence the difference in the electrochemical performances will only be due to the different assemblies.

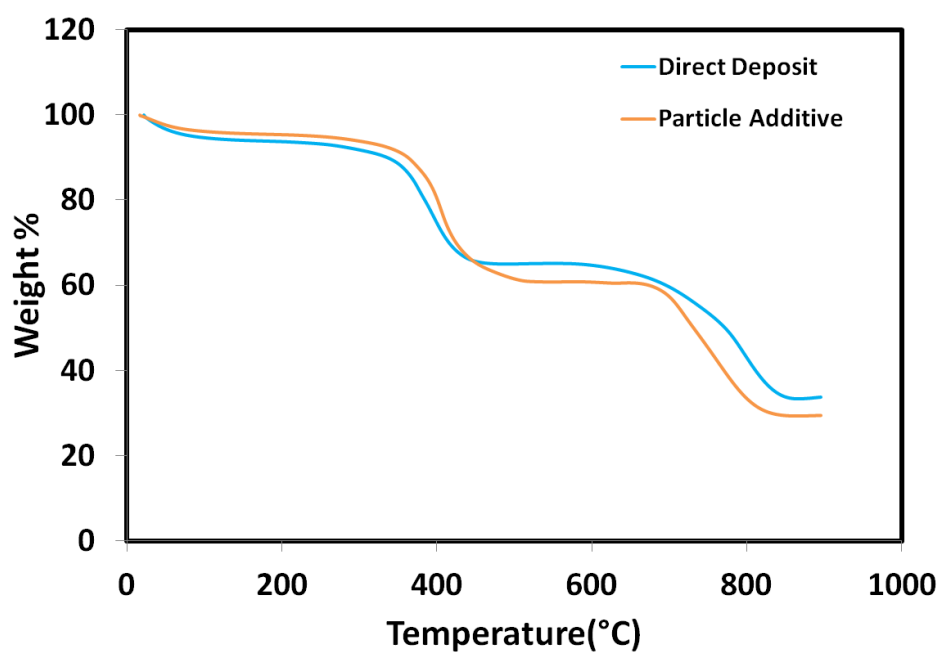


Figure 4.8 TGA analysis of particle additive and direct deposit

Figure 4.9 shows the SEM images of the particles upon changing the infusion rate of electrospraying. Figure 4.9 a) shows the particle morphology at the infusion rate 0.01ml/min and we can observe the particle is slightly spherical and has a dense structure. Figure 4.9 b) shows the particle morphology at 0.02ml/min and a smoother surface is visible as well as the size of the particle decreases. Figure 4.9 c) shows the particle morphology at 0.03ml/min and we can see the particle at this point is more porous but the size increases. Figure 4.9 d) shows that the particle morphology at 0.04ml/min and we can see that instead of spherical like structure we get rod-like structure i.e. the morphology completely changes which is possibly due to incomplete drying of the solvent at such a high infusion rate and the size increases. Figure 4.10 shows the particle size distribution w.r.t. infusion rate. We can see that the size is at its lowest at 0.02ml/min and then it increases again with increasing infusion rate. Figure 4.11 shows the SEM images displaying the effect of relative volatility of the solvent used in electrospraying on the particle morphology. Figure 4.11 a) shows the particle morphology after using 100% NMP solvent which has the highest relative volatility and we can see the particle morphology is very dense and the particle size is very inhomogeneous because of the difficulty involved in evaporating a solvent which has such a low volatility. Figure 4.11 b) shows the particle morphology after using 100% DMF as the solvent bringing down the relative volatility and we observe that the particle is highly porous and bulky but the size reduces. Figure 4.11 c) shows the morphology of the particle after using 1:1:1 ratio of NMP/DMF/DMA as the solvent and as is visible the particles are become denser and more sphere-like because of the decrease in the relative volatility from 4.12 b). Figure 4.11 d) shows effect of using

NMP/DMF/THF in a ratio of 1:1:1 solvent on particle morphology and we can see that the particle morphology is dense and the size reduces further. Figure 4.12 shows the particle size distribution w.r.t. relative volatility which is changed by changing the solvent used for electrospaying, based on the solubility of the PI, and it is evident that there is a direct relation between the particle size and relative volatility i.e. the size decreases as the relative volatility increases which has been the case in the literature as well[37][38][39]. Figure 4.13 shows the SEM images of the particles on changing the distance from the tip of the nozzle to the collector. Figure 4.13 a) shows the particle morphology when the distance from the collector is 20cm and we can see that the particle is dense and sphere-like. Figure 4.13 b) shows the SEM image of the particle when the distance from the collector is 25 cm and we can see that the particle is very much sphere-like and dense and the size increases. Figure 4.13 c) shows the SEM image of the particle when the distance from the collector is 30 cm and we can see that the particle morphology is slightly dense and sphere-like while the size decreases. Figure 4.14 shows particle size distribution w.r.t. distance from the collector and we can see that we have a maxima in terms of the particle size at 25cm. Figure 4.15 shows the SEM images of the particles on changing the voltage applied during electrospay. Figure 4.15 a) shows the SEM image of the particle when the voltage is at 20KV and we can see that not only is the particle slightly dense but also it has a sphere like and smooth morphology. Figure 4.15 b) shows the SEM image of the particle at 25KV and we can see that the surface is very rough but the size of the particle decreases. Figure 4.15 c) shows the SEM image of the particle at 30KV and it is evident that the morphology is rough and dense but the size increases. Figure 4.16 shows the particle size

distribution w.r.t. voltage and we can see the resulting PSD is very similar to that of rate in the sense that there is a minima at 25KV. Figure 4.17 shows the SEM images of the particle on changing the applied air pressure during the electrospray. Figure 4.17 a) show the SEM image of particle at 25psi and we can see the surface is very smooth and the particle is very much sphere-like. Figure 4.17 b) shows the SEM image of the particle at 30psi and we can see that the morphology is dense and rough and the size reduces. Figure 4.17 c) shows the SEM image of particle at 35psi and it is visible that the particle morphology changes from dense to porous. Figure 4.18 shows the particle size distribution w.r.t. air pressure and we can see yet again we get a similar distribution as previously obtained for infusion rate and voltage i.e. a minima at 30psi.

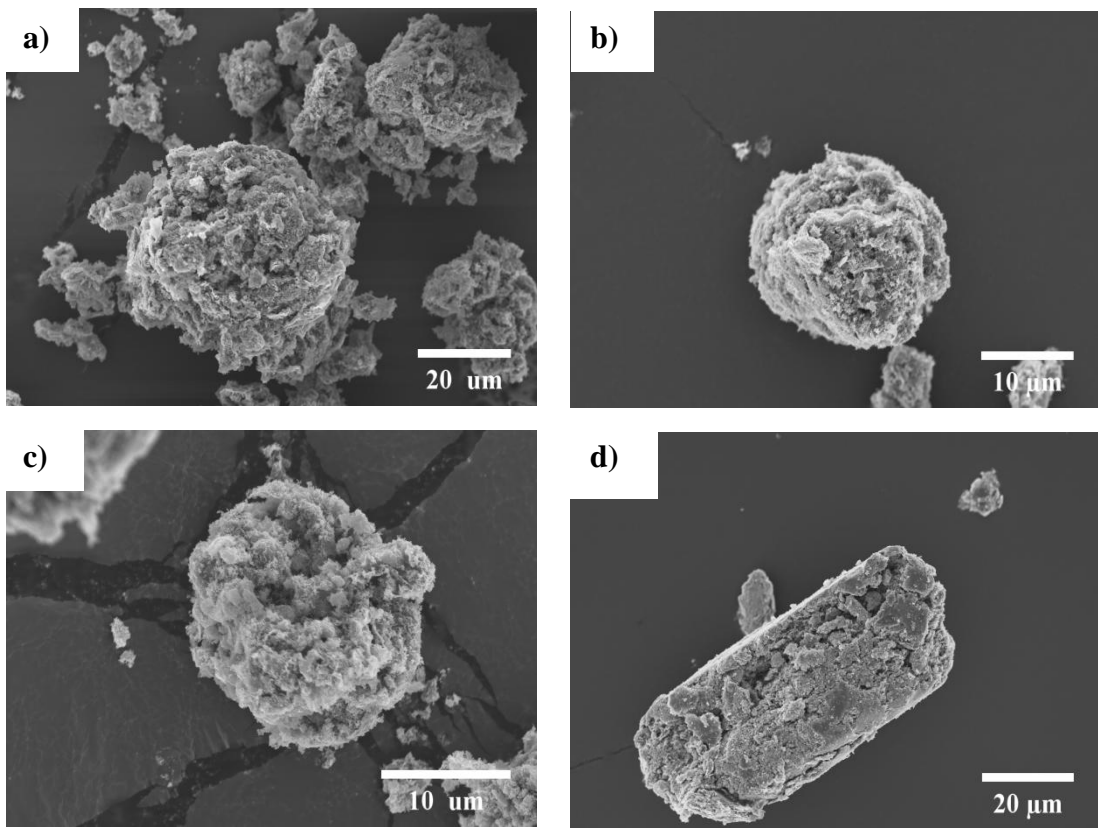


Figure 4.9 SEM images of particle morphology at a) 0.01 ml/min b) 0.02ml/min c) 0.03ml/min and d) 0.04 ml/min infusion rate

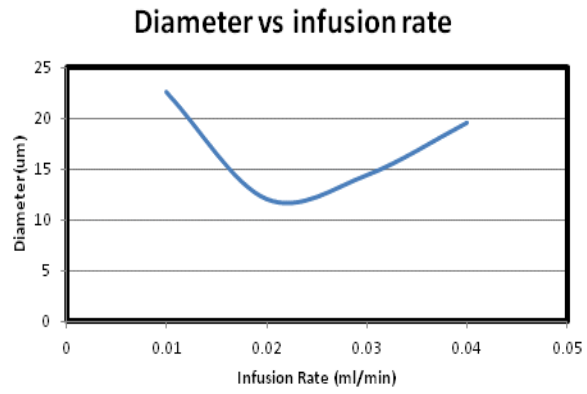


Figure 4.10 Particle size distribution vs. infusion rate

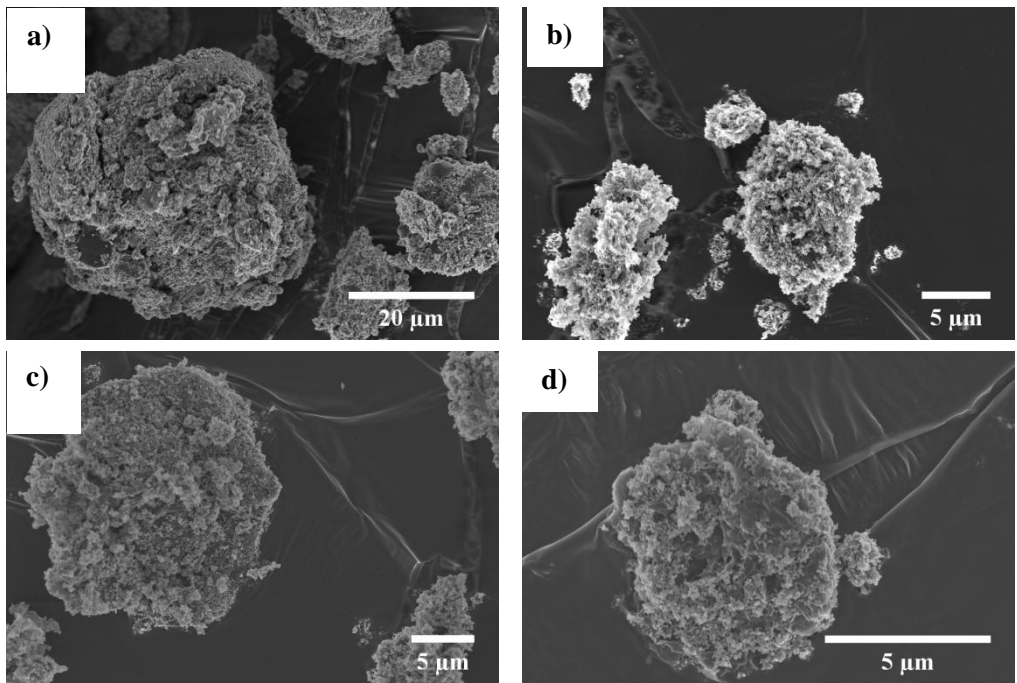


Figure 4.11 SEM images of particle morphology at a) 100% NMP b) 100% DMF c) NMP/DMF/DMA and d) NMP/DMF/THF

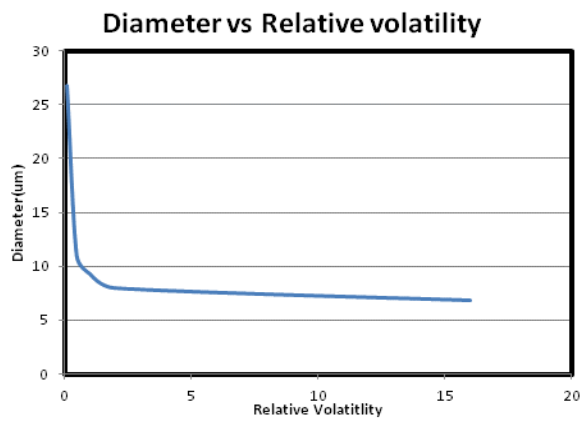


Figure 4.12 Particle size distribution vs. relative volatility

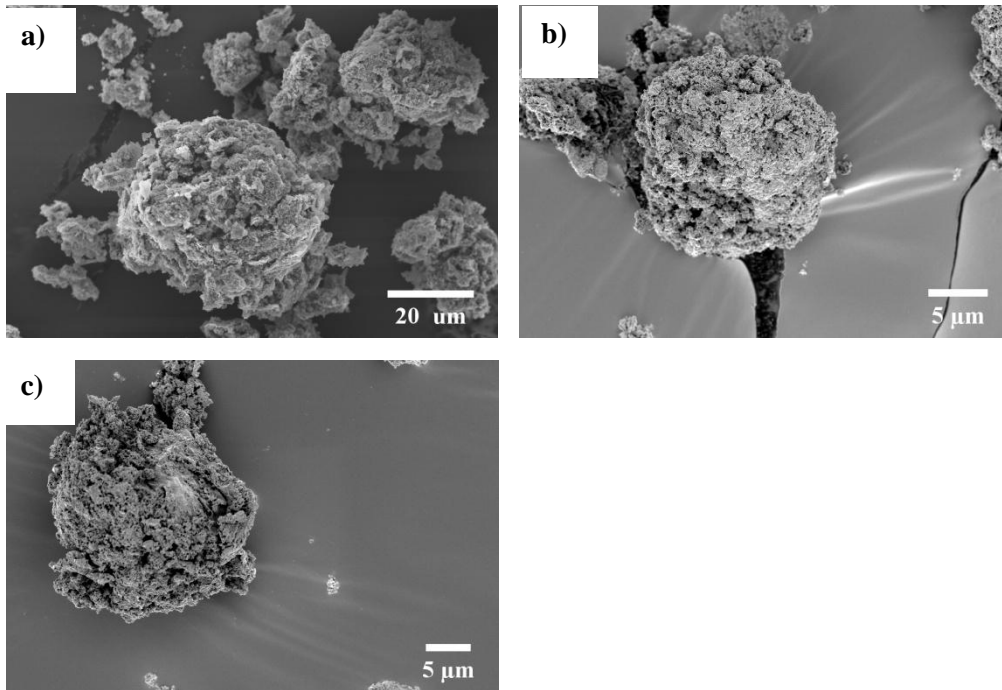


Figure 4.13 SEM images of particle morphology at a) 20cm b) 25cm and c) 30cm distance from the collector

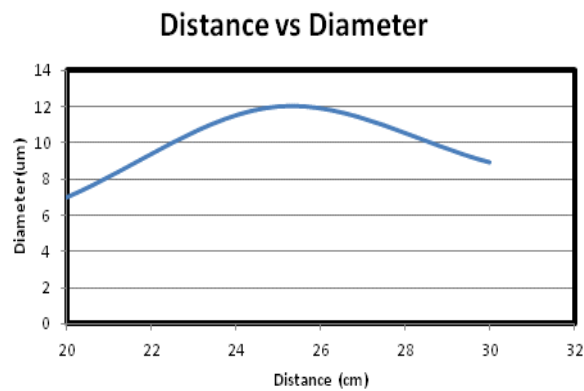


Figure 4.14 Particle size distribution vs. distance from collector

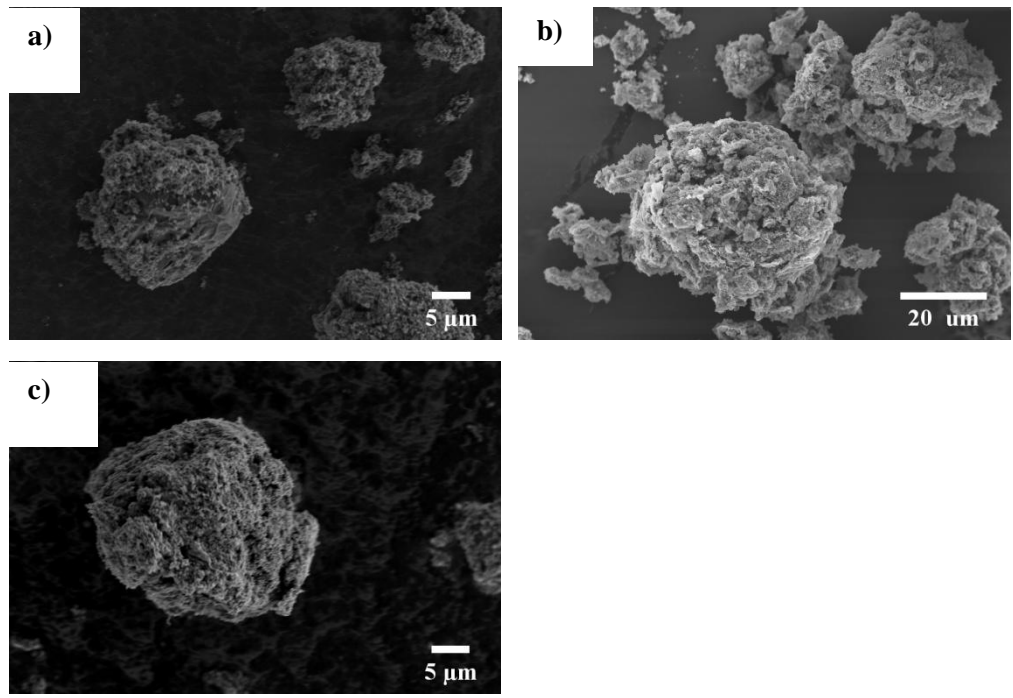


Figure 4.15 SEM images of particle morphology at a) 20KV b) 25KV and c) 30KV voltage

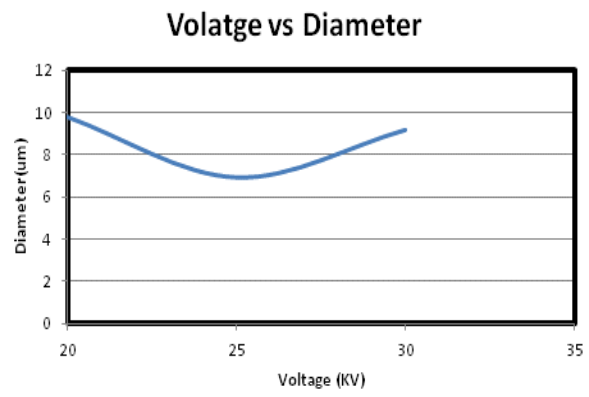


Figure 4.16 Particle size distribution vs. voltage

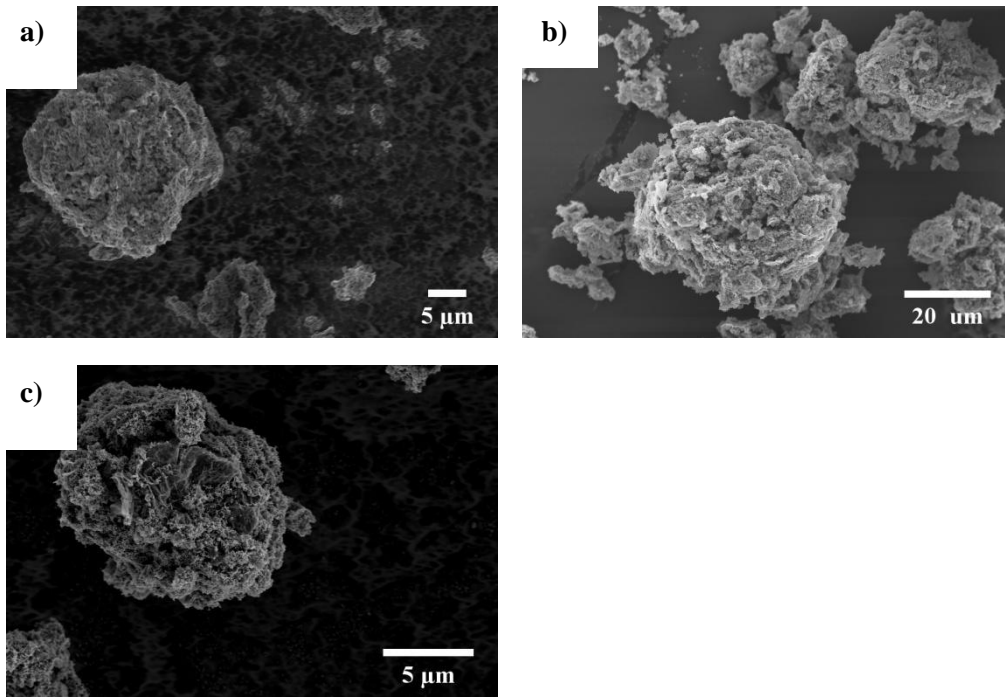


Figure 4.17 SEM images of particle morphology at a) 25 psi b) 30 psi and c) 35 psi air pressure

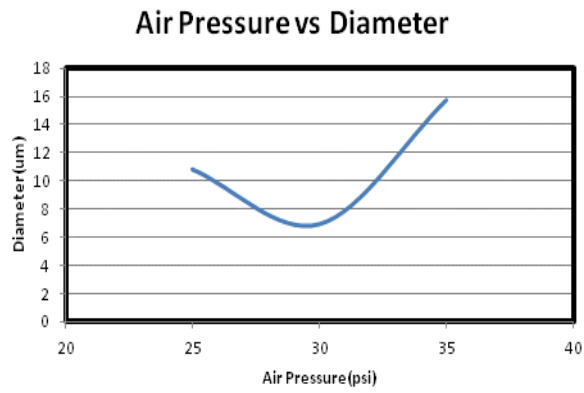


Figure 4.18 Particle size distribution vs. air pressure

Figure 4.19 shows the internal pore size distribution inside the particles by changing various parameters of electro spraying which was used for the electrochemical performance study. The 3 cases chosen are divided into high density, low density and medium density which can be obtained by either changing the solvent or other parameters of electro spraying as discussed previously. The LD has a surface area of $52.18 \text{ m}^2/\text{g}$, the MD has a surface area of $39.21 \text{ m}^2/\text{g}$, the HD has a surface area of $28.35 \text{ m}^2/\text{g}$. Figure 4.20 shows the thermogravimetric analysis of 3 sizes of particles, representing the average size calculated from PSD, $7\mu\text{m}$, $12\mu\text{m}$ and $20\mu\text{m}$ respectively, chosen to study the effect of particle size of electrochemical performance and it is clear that the composition of the electrode is the same. Figure 4.21 shows the thermogravimetric analysis of LD, MD and HD confirming that the composition of the respective electrodes is the same.

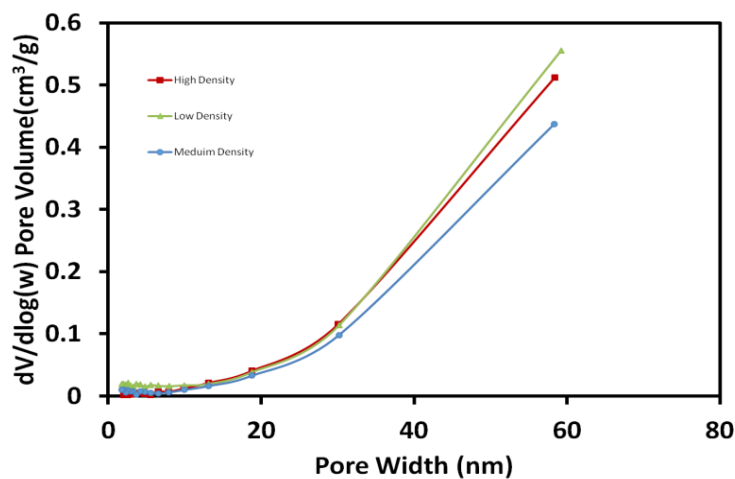


Figure 4.19 BET analysis of HD, LD and MD

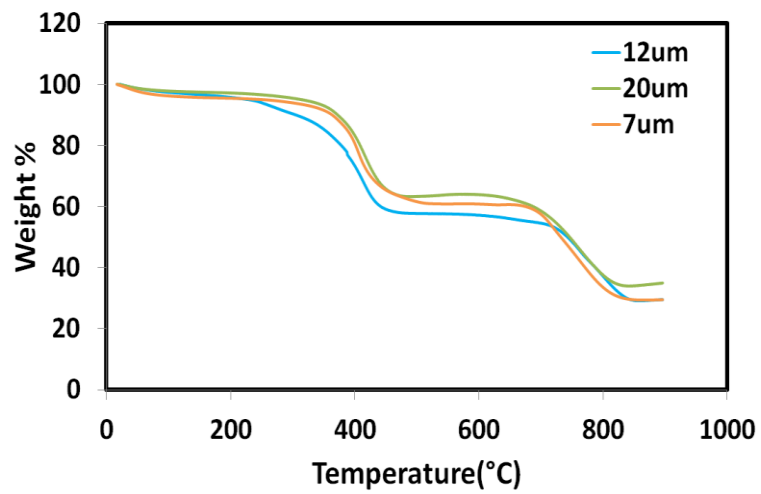


Figure 4.20 TGA analysis 12µm, 20µm and 7µm

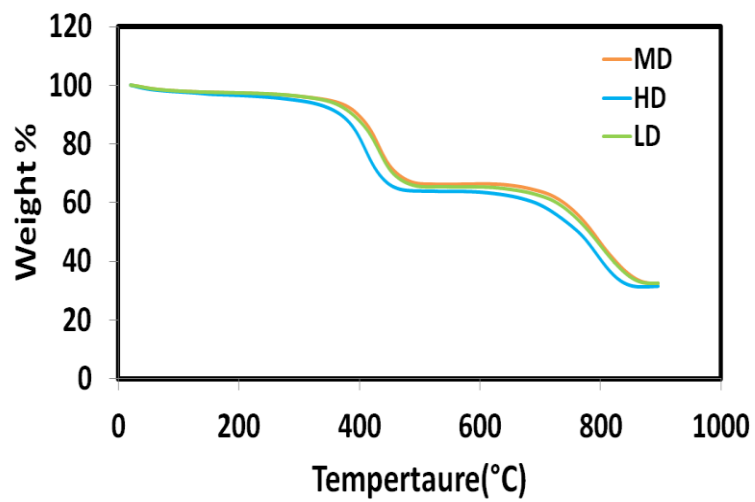


Figure 4.21 TGA analysis of MD, HD and LD

Half-cell Electrochemical Performance:

To compare the electrochemical performance 2032 coin type half cells were assembled. Each cell was lithiated to a voltage of 1.5V and delithiated to a voltage of 0.01V and made to undergo 5 formation cycles at 0.1C and then undergo cycling pattern as mentioned previously thereafter. The capacity-voltage graph comparison for the particle additive and direct deposit is shown figure 4.22. The particle additive gives us a delithiation 1st cycle capacity of 720-780mAh/g whereas the same for the direct deposit system is 530-565 mAh/g. This is possibly due to the better silicon coverage by carbon made possible by the assembly obtained from particle additive system. The ICE for particle additive is 69% and for direct deposit is 65%. The lower than expected ICE could be because of the use of polyimide which has a tendency to react with lithium[40] Figure 4.23 a) and b) shows the EDX image silicon and carbon distribution for particle additive and direct deposit respectively which explains why a higher capacity is obtained for the particle additive despite the same composition. Figure 4.24 a) and b) shows the EIS spectra comparison of direct deposit and particle additive before and after formation respectively. It is evident that the charge transfer resistance for the particle additive is lower compared to direct deposit possibly because of better conduction pathways formed between the silicon and graphene and better carbon coverage of silicon. The charge transfer resistance decreases after formation due to the formation of the lithiated amorphous phase of silicon from the pristine crystalline silicon before formation[41].

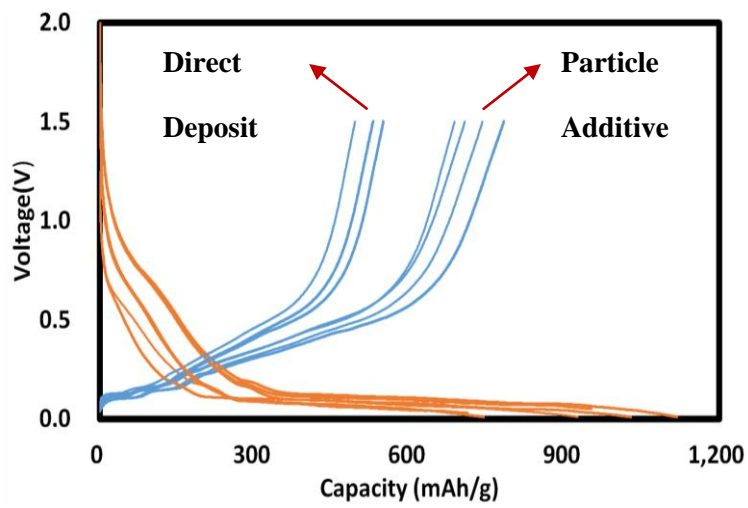


Figure 4.22 Initial capacity-voltage profile particle additive and direct deposit

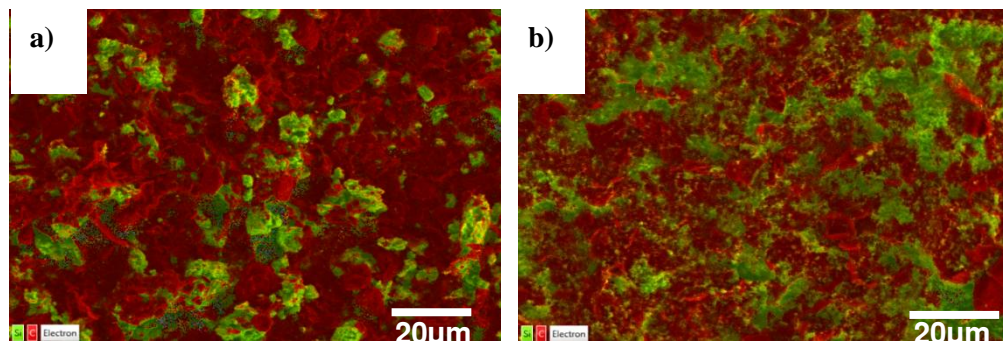


Figure 4.23 EDX image of silicon and carbon distribution a) particle additive b) direct deposit electrode

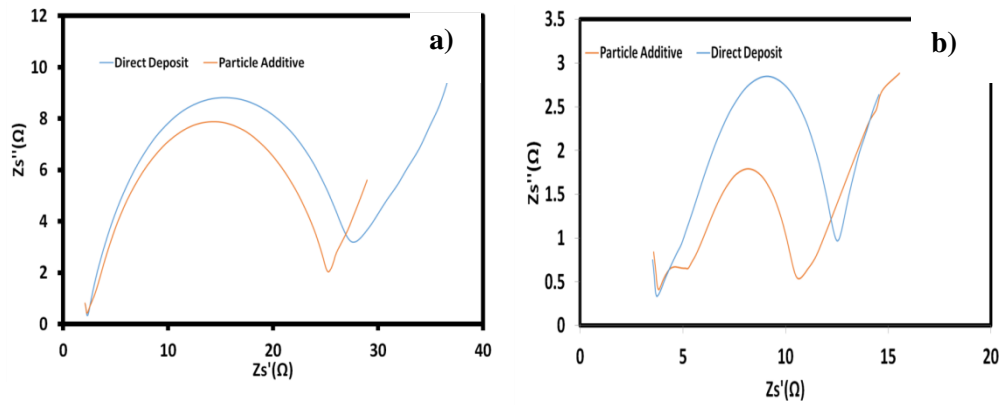


Figure 4.24 Nyquist plot of impedance data comparison a) before formation b) after formation between particle additive and direct deposit

Figure 4.25 shows the cycling performance of direct deposit and particle additive. The particle additive is able to retain its higher capacity for over 300 cycles of deep charge and discharge. Figure 4.26 shows the rate capability performance of the direct deposit and particle additive and it is evident that even at harsh C rates like 2C the particle additive is able to maintain its higher capacity possibly due to its better silicon connectivity and lesser overall charge transfer resistance.

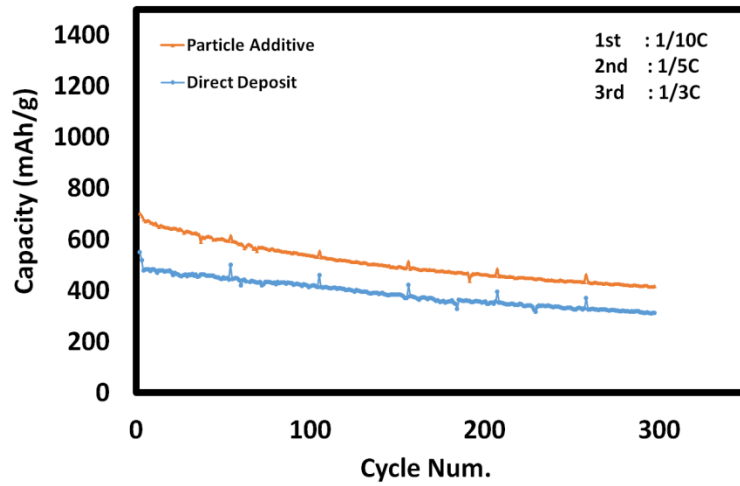


Figure 4.25 Cycle performance of particle additive and direct deposit

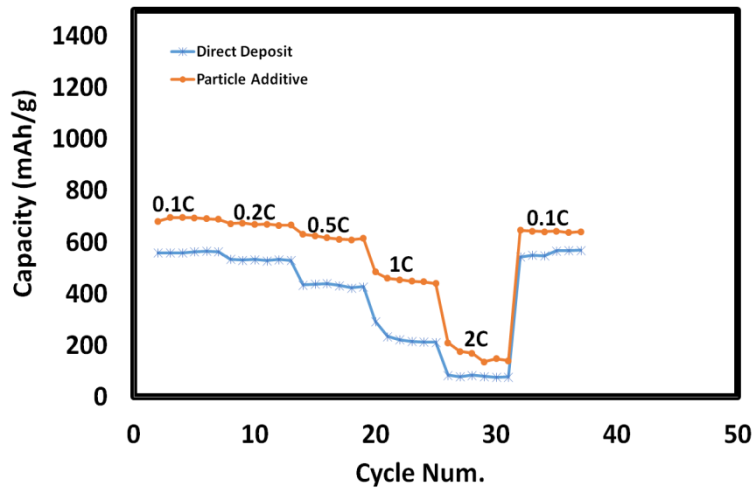


Figure 4.26 Rate capability of particle additive and direct deposit

The capacity-voltage graph comparison for different size of particles is shown figure 4.27. The 7 μm and 12 μm particle size gives almost identical capacity of 745mAh/g but the largest size of 20 μm gives a relatively lower capacity of 711mAh/g which suggests that a minor change in size does not affect the capacity by much but a major change in size does decrease the capacity possibly because of the larger sized particles not able to establish a good electrical contact with CP11 and SF6. Figure 4.28 shows the EIS spectra comparison of 7 μm , 12 μm and 20 μm . From figure 4.28 we learn that 20 μm has the highest charge transfer resistance of the lot possibly because of its lack of contact with graphite whereas 12 μm has the smallest charge transfer resistance possibly because it has the most compact structure and good packing being very close to the size of the graphite used in this study. Another interesting observation is that the 12 μm shows the worst diffusion of Li-ions represented by the tail of the impedance spectra possibly due to the compact and dense structure obtained.

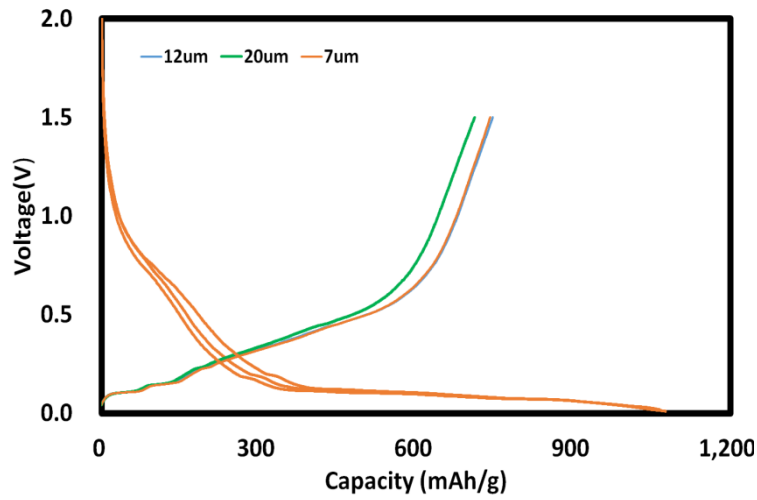


Figure 4.27 Initial capacity-voltage profile of 12µm, 20 µm and 7µm

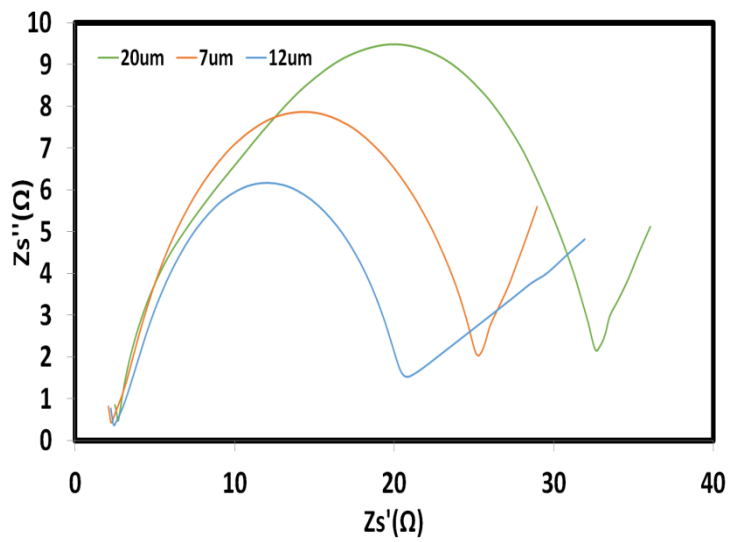


Figure 4.28 Nyquist plot for impedance data for 20µm, 7µm, and 12µm

Figure 4.29 shows the cycling performance of different size of the particle. The 20 μm shows the worst cycling performance possibly due to its larger sized particles do not have a good synergy with the graphite originating from its high charge transfer resistance. The 12 μm and 7 μm give a very similar cycling performance until 200 cycles but the 12 μm sized particle electrode shows a sharp decline possibly due to its compact structure not giving enough room for silicon to expand. Figure 4.30 shows the rate capability of the different sized particle electrodes. The 20 μm gives the best performance at 2C possibly because of its better lithium ion diffusivity as shown in figure 4.28. The 7 μm shows the worst rate capability because of its lower electrode density suggesting weaker packing. This shows the ability to choose the right size of the particle based on the requirement.

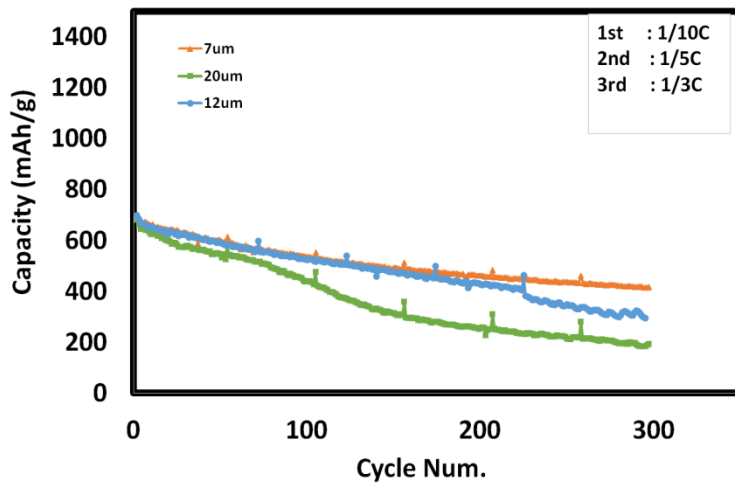


Figure 4.29 Cycle performance of 7µm, 20µm and 12µm

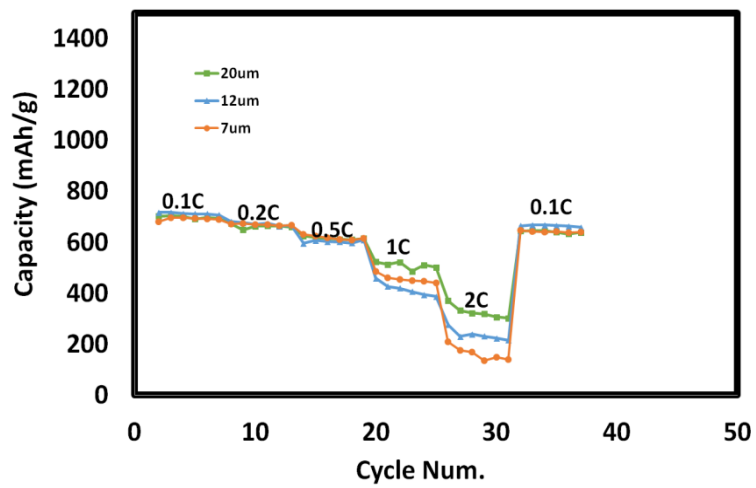


Figure 4.30 Rate capability of 20µm, 12µm and 7µm

The capacity-voltage graph comparison for different levels of porosity of the particles is given in figure 4.31. HD electrode which is the least porous and MD which has intermediate level of porosity show almost similar capacity of 800mAh/g whereas LD i.e. the electrode with the highest level of porosity shows a significantly lower capacity of 575 mAh/g. This is possibly because LD has such a porous structure that the silicon occupying these pores is electronically isolated and thus cannot participate in the reaction with Li-ions therefore remaining underutilized. The ICE of both LD and MD is 70% but that of HD is 67% possibly because of the compact densely packed structure makes the movement of Li-ions back difficult and hence the drop in ICE for HD. Figure 4.32 shows the cycling performance of LD, MD, HD. The HD shows 31% capacity retention, the MD shows 55% retention and the LD shows 53% retention after 300 cycles of deep charge and discharge. The worst performance of HD is because of the lack of internal pores inside the particle which does not contribute towards mitigating volume expansion whereas the better performance of LD and MD comes because of the porous structure of the particles which allow for the stress relaxation created by the silicon volume expansion[42]. Another important thing to note is despite the MD is slightly less porous compared to LD the cycle retention performance is almost similar which points at an optimum amount of porosity of the particles. This is because LD is very loosely packed and there is not enough conductive bridge between the silicon and the voids which leads to a slow decline in cycling performance[43]. The rate capability performance of LD, HD and MD is shown in figure 4.33. The HD has the worst performance at 2C probably because the

dense electrode structure makes it difficult for the fast transport of Li-ions. The LD electrode has marginally better performance but the lack of electronic connectivity and lower capacity to begin with leads to the ordinary rate capability. The MD has the best rate capability performance and again points at the most optimized porous structure.

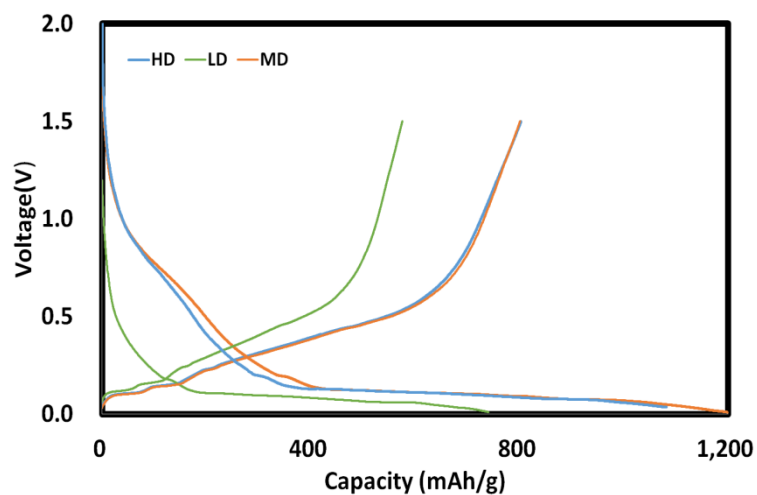


Figure 4.31 initial capacity-voltage profiles of HD, LD and MD

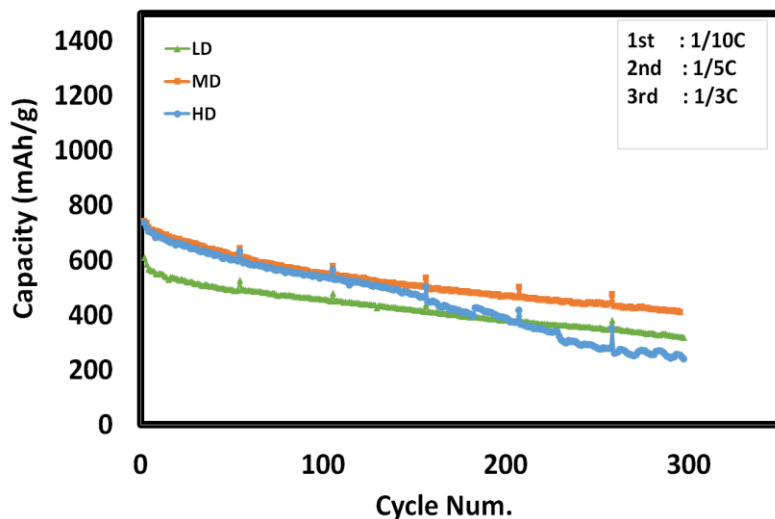


Figure 4.32 Cycle performance of LD, MD and HD

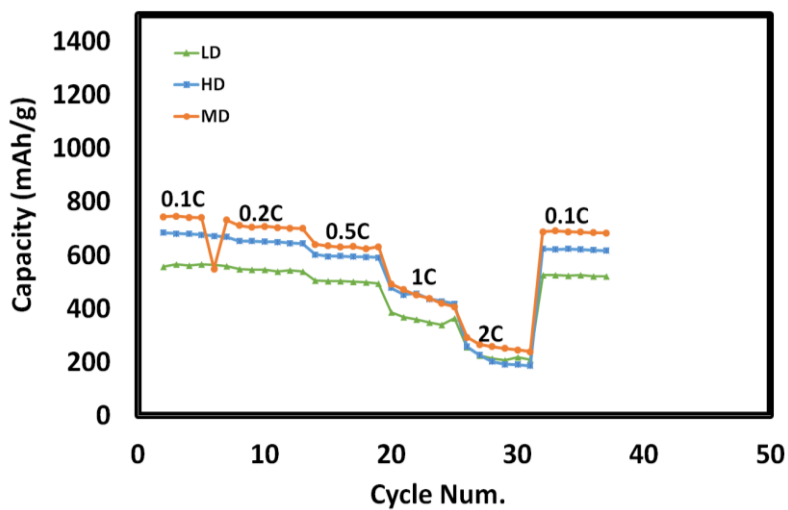


Figure 4.33 Rate capability performances of LD, HD and MD

4.4 Conclusion

In the present study we have successfully combined the work done in chapter 1 and chapter 2 to come up with a new method of material processing by using a particle additive system which helps in decreasing the overall volume expansion by controlling the particle properties and preserving the particle structure thereby increasing the energy density of the electrode. We also highlight the advantages of this particle additive system by comparing it with direct deposit system used in previous work and find that the particle additive system not only gives us a much higher capacity but is also able to retain this higher capacity over multiple cycles of charge and discharge and over harsh rate capability condition. We also display a high degree of tuneability and control in the synthesis of the particles of producing particles of various different size, morphology and porosity by changing the electrospraying parameters which enables us to synthesize these particles based on any particular requirement. We further study the effect of the size of the particles on electrochemical

performance by using a set of 3 different sized particles namely 7 μ m, 12 μ m and 20 μ m. We find that in terms of capacity there is not a big difference between 7 μ m and 12 μ m but by increasing the size to 20 μ m the capacity decreases marginally. In terms of cycling performance the smallest size performed the best but in terms of rate capability the largest size gave the best performance exemplifying the ability to make particles depending on the requirement. We further extend this study by studying the effect of porosity of the particles on the electrochemical performance by comparing highly porous LD, highly dense HD and moderately porous MD. We find that having pores help in the relaxation of stress accompanied by the silicon volume expansion and hence LD and MD outperform HD in cycling performance. Also we see that MD gives a much higher capacity and the same retention as LD which showed us an optimum value of porosity since having too many pores makes the electrode structure very loose and leads to electronic isolation.

REFERENCES

- [1] M. Armand and J. Tarascon, "Building better batteries," vol. 451, no. February, pp. 2–7, 2008.
- [2] B. Dunn, H. Kamath, and J. Tarascon, "for the Grid : A Battery of Choices," vol. 334, no. November, pp. 928–936, 2011.
- [3] P. G. Bruce, B. Scrosati, and J. Tarascon, "Lithium Batteries Nanomaterials for Rechargeable Lithium Batteries ** Angewandte," pp. 2930–2946, 2008.
- [4] M. Li, J. Lu, Z. Chen, and K. Amine, "30 Years of Lithium-Ion Batteries," vol. 1800561, pp. 1–24, 2018.
- [5] E. Environ, J. R. Szczech, and S. Jin, "Energy & Environmental Science Nanostructured silicon for high capacity lithium battery anodes †," pp. 56–72, 2011.
- [6] N. S. Hochgatterer *et al.*, "Silicon / Graphite Composite Electrodes for High-Capacity Anodes : Influence of Binder Chemistry on Cycling Stability," pp. 76–80, 2008.
- [7] J. P. Maranchi, A. F. Hepp, and P. N. Kumta, "High Capacity , Reversible Silicon Thin-Film Anodes for Lithium-Ion Batteries," pp. 198–201, 2016.
- [8] X. Zuo, J. Zhu, P. Müller-buschbaum, and Y. Cheng, "Nano Energy Silicon based lithium-ion battery anodes : A chronicle perspective review," *Nano Energy*, vol. 31, no. November 2016, pp. 113–143, 2017.
- [9] L. Y. Beaulieu, K. W. Eberman, R. L. Turner, and L. J. Krause, "Colossal Reversible Volume Changes in Lithium Alloys," vol. C, pp. 7–10, 2001.
- [10] J. H. Ryu, J. W. Kim, Y. Sung, and S. M. Oh, "Failure Modes of Silicon Powder Negative Electrode in Lithium Secondary Batteries," pp. 306–309, 2004.
- [11] H. Wu and Y. Cui, "Designing nanostructured Si anodes for high energy," pp. 414–429, 2012.
- [12] J. M. Chem *et al.*, "The failure mechanism of nano-sized Si-based negative electrodes for lithium ion batteries," no. Cmc, pp. 6201–6208, 2011.

- [13] M. Ashuri and L. L. Shaw, “batteries : where size , geometry and structure,” pp. 74–103, 2016.
- [14] C. K. Chan *et al.*, “High-performance lithium battery anodes using silicon nanowires,” pp. 31–35, 2007.
- [15] H. Wu *et al.*, “conformally coat silicon nanoparticles,” *Nat. Commun.*, vol. 4, pp. 1943–1946, 2013.
- [16] E. Environ, “Environmental Science Improving the cycling stability of silicon nanowire anodes with conducting polymer coatings †,” pp. 7927–7930, 2012.
- [17] C. Wang, H. Wu, Z. Chen, M. T. Mcdowell, Y. Cui, and Z. Bao, “operation of silicon microparticle anodes for,” *Nat. Chem.*, vol. 5, no. 12, pp. 1042–1048, 2013.
- [18] H. Xiang *et al.*, “Graphene / nanosized silicon composites for lithium battery anodes with improved cycling stability,” vol. c, pp. 0–9, 2011.
- [19] J. Ren, Q. Wu, G. Hong, W. Zhang, and H. Wu, “Silicon – Graphene Composite Anodes for High-Energy Lithium Batteries,” vol. 60439, pp. 77–84, 2013.
- [20] S. Chen, M. L. Gordin, R. Yi, G. Howlett, H. Sohn, and D. Wang, “Silicon core-hollow carbon shell nanocomposites with tunable buffer voids for high capacity anodes of lithium-ion batteries,” *Phys. Chem. Chem. Phys.*, vol. 14, no. 37, pp. 12741–12745, 2012.
- [21] L. Wu, J. Yang, X. Zhou, M. Zhang, Y. Ren, and Y. Nie, “Silicon nanoparticles embedded in a porous carbon matrix as a high-performance anode for lithium-ion batteries,” pp. 11381–11387, 2016.
- [22] Q. Xiao *et al.*, “Inward lithium-ion breathing of hierarchically porous silicon anodes,” *Nat. Commun.*, vol. 6, pp. 1–8, 2015.
- [23] T. Ikonen, T. Nissinen, E. Pohjalainen, O. Sorsa, T. Kallio, and V. P. Lehto, “Electrochemically anodized porous silicon: Towards simple and affordable anode material for Li-ion batteries,” *Sci. Rep.*, vol. 7, no. 1, pp. 1–8, 2017.
- [24] F. Dai *et al.*, “Minimized Volume Expansion in Hierarchical Porous Silicon upon Lithiation,” *ACS Appl. Mater. Interfaces*, vol. 11, no. 14, pp. 13257–13263, 2019.
- [25] K. Zhang, Y. Xia, Z. Yang, R. Fu, C. Shen, and Z. Liu, “Structure-preserved 3D porous silicon/reduced graphene oxide materials as anodes for Li-ion batteries,” *RSC Adv.*, vol. 7, no. 39, pp. 24305–24311, 2017.
- [26] H. Wu *et al.*, “Six Thousand Electrochemical Cycles of Double-Walled Silicon Nanotube Anodes for Lithium Ion Batteries,” *Nat. Nanotechnol.*, vol. 7, pp. 310–315, 2012.
- [27] N. Liu *et al.*, “A pomegranate-inspired nanoscale design for large-volume-change lithium battery anodes,” *Nat. Nanotechnol.*, vol. 9, no. 3, pp. 187–192, 2014.

- [28] H. Wu, G. Zheng, N. Liu, T. J. Carney, Y. Yang, and Y. Cui, "Engineering empty space between Si nanoparticles for lithium-ion battery anodes," *Nano Lett.*, vol. 12, no. 2, pp. 904–909, 2012.
- [29] S. Chae, S. Choi, N. Kim, J. Sung, and J. Cho, "Integration of Graphite and Silicon Anodes for the Commercialization of High-Energy Lithium-Ion Batteries *Angewandte Reviews*," pp. 2–28.
- [30] J. Wu, "The critical role of carbon in marrying silicon and graphite anodes for high - energy lithium - ion batteries," no. August, pp. 1–20, 2019.
- [31] J. Park, J. Ham, M. Shin, H. Park, Y. Lee, and S. Lee, "Synthesis and electrochemical characterization of anode material with titanium e silicon alloy solid core / nanoporous silicon shell structures for lithium rechargeable batteries," *J. Power Sources*, vol. 299, pp. 537–543, 2015.
- [32] S. Son *et al.*, "Interfacially Induced Cascading Failure in Graphite-Silicon Composite Anodes," vol. 1801007, pp. 1–8, 2019.
- [33] M. Wetjen, S. Solchenbach, H. A. Gasteiger, D. Pritzl, J. Hou, and V. Tileli, "Morphological Changes of Silicon Nanoparticles and the Influence of Cutoff Potentials in Silicon-Graphite Electrodes," vol. 165, no. 7, pp. 1503–1514, 2018.
- [34] H. Wang, J. Xie, S. Zhang, G. Cao, and X. Zhao, "RSC Advances battery anode materials †," vol. c, pp. 69882–69888, 2016.
- [35] Q. Xu, J. Sun, J. Li, Y. Yin, and Y. Guo, "Scalable synthesis of spherical Si / C granules with 3D conducting networks as ultrahigh loading anodes in lithium-ion batteries," *Energy Storage Mater.*, vol. 12, no. November 2017, pp. 54–60, 2018.
- [36] S. Y. Kim, J. Lee, B. Kim, Y. Kim, K. S. Yang, and M. Park, "Facile Synthesis of Carbon-Coated Silicon/Graphite Spherical Composites for High-Performance Lithium-Ion Batteries," 2016.
- [37] F. Raeesi, M. Nouri, and A. K. Haghi, "Electrospinning nanofibers of," no. 114, pp. 1–13, 2009.
- [38] X. Hao *et al.*, "Effects of the Electro spray Ionization Parameters on the Formation and Morphology of Colloidal Microspheres of Polyacrylonitrile," vol. 102, pp. 2889–2893, 2006.
- [39] C. H. Park and J. Lee, "Electrosprayed Polymer Particles : Effect of the Solvent Properties."
- [40] J. Oh, D. Jin, K. Kim, D. Song, Y. M. Lee, and M. H. Ryou, "Improving the Cycling Performance of Lithium-Ion Battery Si/Graphite Anodes Using a Soluble Polyimide Binder," *ACS Omega*, vol. 2, no. 11, pp. 8438–8444, 2017.
- [41] J. Guo, A. Sun, X. Chen, C. Wang, and A. Manivannan, "Cyclability study of silicon-carbon composite anodes for lithium-ion batteries using electrochemical impedance spectroscopy," *Electrochim. Acta*, vol. 56, no. 11, pp. 3981–3987, 2011.

- [42] S. Li *et al.*, “Silicon/carbon composite microspheres with hierarchical core-shell structure as anode for lithium ion batteries,” *Electrochem. commun.*, vol. 49, pp. 98–102, 2014.
- [43] G. Shoorideh *et al.*, “Harvesting Interconductivity and Intraconductivity of Graphene Nanoribbons for a Directly Deposited , High-Rate Silicon-Based Anode for Li-Ion Batteries,” 2018.

CHAPTER 5

FUTURE WORK

5.1 Chapter 2

In the 1st part of this chapter we show the effect of pores and the 2nd part of the chapter attempts to explain the effect of GNR. In both cases we see an improvement from the reference electrodes in cycling performance and we concluded that in the 1st case the improvement is caused by the pores being able to mitigate the volume expansion generated by silicon expansion and contraction and in the second case the improvement is due to GNR forming a bridge between the graphene sheets and silicon nanoparticles inside the voids. It was thus concluded that we are addressing two primary modes of failure for a silicon anode based lithium ion battery. But in order to prove this hypothesis we should measure the evolution of volume expansion for case 1 and 2 separately. The short-term future goal of the project is measuring an in-situ volume expansion by using dilatometer. This will provide a quantitative measure of volume expansion and its evolution over a number of cycles of charge and discharge

in real time. If this measurement is carried out independently for both case 1 and case 2 we can measure the amount of decrease in the thickness change by the creation of pores and compare it with an electrode structure without externally created pores and also see the effect of addition of GNR to confirm our hypothesis of addressing the root cause of failure in silicon anode based electrodes. Figure 5.1 shows the in-situ dilatometer measurement for PAA_REM which shows a significant reduction in the thickness change of the silicon anode possibly because of the porous structure. This will have to be compared to the reference electrode.

In the same way the effect of GNR on thickness change can be seen to effectively prove the hypothesis. Also post-mortem EDX and XPS analysis should be done to see the SEI composition after cycling and check if it can form a stable SEI layer. One of the long term future goals of this project would be to combine in-situ dilatometry with graphene stress based FEM modeling to fundamentally study the role of graphene in application of compressive stress and the role of pores to help in channelize the volume expansion in inward direction. Also the modeling and in-situ dilatometry can be combined with in-situ TEM to get a visual picture of the silicon expanding and also study AFM and monitor the changes on the surface of the electrode as the silicon expands. If this is combined it will serve as a very powerful tool to not only obtain fundamental insights into the mechanism of silicon expansion but also to minimize it.

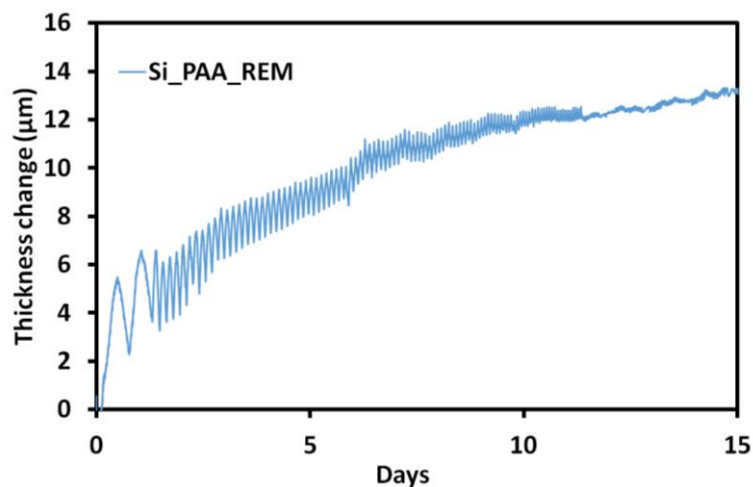


Figure 5.1 In-situ dilatometer measuring thickness change evolution with time

5.2 Chapter 3

In this chapter we have showed that the blending the two types of graphite with different shape and different morphology gave us a good cycle life performance and great rate capability. However, the capacity of this blended system is less than SF-6 only system. One way of potentially increasing this 1st cycle capacity is by adding a small amount of GNR in the system which will act as conductive bridge between CP11 and SF6 which should result in a higher activation of the graphite and thus

increase its capacity. Figure 5.2 shows a cross-section SEM image of GNR acting as a conduction bridge between CP11 and SF6. With the GNR acting as a conductive bridge we could also enhance the rate capability even further. Combining graphite and GNR has never been studied before and should give very useful insights especially considering the demand for a silicon graphite based hybrid system due to its widespread practical scope.

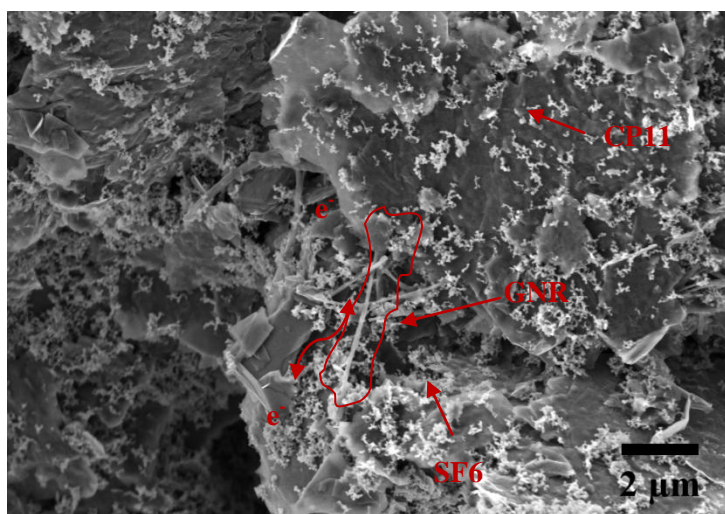


Figure 5.2 SEM image of cross section of CP11/SF6/GNR electrode

5.3 Chapter 4

In this chapter we showed a new particle additive method which was better than direct deposit method. One of the concerns was the low ICE which needs to be improved. This can be done by changing the binder from PI to PAN or by increasing the content

of graphite further and reducing silicon content. Another way to improve the particle additive system is creating external pores in the 1st step of this process and adding GNR exactly as done in chapter 2. These external pores along with the internal pores created for the particle based system should further boost the cycle like and addition of GNR will give intra-particle connectivity and achieve a very high level of control on volume expansion at the particle level. For the second step we can add GNR along with graphite to achieve a particle graphite inter-connectivity which should boost the capacity despite reducing silicon content to around 20%. Figure 5.3 illustrate the idea. This system will be of great industrial relevance as well as fundamental relevance. Finally, we can do an in-situ dilatometry test for this new modified particle additive system and compare it with direct deposit system.

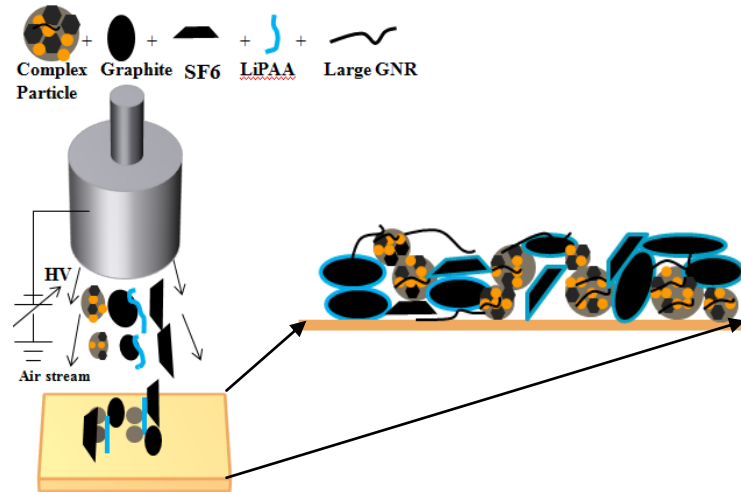


Figure 5.3 Schematic illustrating step 1 of the modified Particle additive method